Università degli Studi di Padova

Dipartimento di Fisica e Astronomia
Galileo Galilei

Corso di Laurea Magistrale in Astronomia

Gravitational Wave detections: implications for Cosmology

Relatore
Prof. Nicola Bartolo
Co-relatori
Dott. Michele Liguori
Dott. Giampaolo Benevento

Laureando
Sarah Libanore
Matricola: 1143936

ABSTRACT

This work explores the middle ground between Astrophysics and Cosmology using one of the most recent tools acquired by science: Gravitational Waves.

From their amplitude, the luminosity distance of the source can be measured; if the redshift is also available, they can be seen as standard sirens. However, in the cases where the redshift is not obtainable, statistical methods have still been proposed to exploit Gravitational Waves in the study of the Universe and its properties.

In this work, one particular method is analyzed. Introducing a statistical estimator, this allows to study the anisotropies in the source distribution due to the clustering and lensing. The Angular Power Spectra of the estimator and of the lensing are derived both in a theoretical and computational way. The Fisher matrix of the first one is also calculated. Future implementations of this method are described and its possible applications both for Cosmology and Astrophysics are put forward.

Contents

Introduction

Cosmology and Astrophysics have seen a huge development in the last 20 years. Researchers working in these areas have been collecting a lot of data and elaborating models to explain them and to predict new observables. Between Cosmology and Astrophysics there is a strong and natural link and the tools of one can be used to deepen our knowledge of the other. Moreover, it is really important making them coherent and finding new methods to give an answer to those questions that are still unanswered.

Multi messenger Astrophysics could be a way to achieve these goals. Nowadays it is becoming reality thanks to the existence of measuring instruments that are more and more sensitive to several kinds of electromagnetic wavelengths as well as Gravitational Waves, neutrinos and cosmic rays. Bridging the pieces of information obtained with the different methods, looking for new observables to test models and improving them in order to describe the details of observed phenomena are the challenges the scientic community is facing nowadays.

This work explores the middle ground between Astrophysics and Cosmology, connecting them using one of the most recent tools acquired by science: Gravitational Waves. The possibility of using Gravitational Waves as a tool for new kinds of research is now concrete, as tested by the recent measurements of various events by the LIGO and VIRGO collaboration. In particular, GW sources can be seen as standard sirens: indeed, their luminosity distance can be obtained studying the wave amplitude. Comparing this measurement with the redshift of the source provides a way to estimate the Universe expansion rate (as we already do using SN IA as standard candles). To obtain the source redshift is however necessary either to identify the host galaxy or to detect an Electro-Magnetic counterpart. Since these will not always be possible, alternative statistical methods have been put forward.

This work focuses on the method presented by Namikawa, Nishizawa, Taruya in the paper *Anisotropies of Gravitational Wave standard sirens as a new Cosmological probe without redshift information* (`arXiv:1511.04638v2`). Considering a given kind of GW source, such as Neutron Stars binary mergers, this article explains how it is possible to build an estimator that, thanks to the fluctuations in the measurements of luminosity distance compared to a statistic distribution, allows to estimate the properties of clustering and lensing of the sources. This can provide a statistical method to study both Cosmology and Astrophysics. In fact, assuming models which exploit prior knowledge of the Astrophysical sources and their distribution, the fluctuations measurement can give information about the underlying Cosmology. Vice versa, if the Cosmology is well modelled, the distribution of the Astrophysical sources can be inferred.

This work is organized as follows.

Chapter 1 introduces Gravitational Waves and their study. It shortly reviews the

main aspects of General Relativity and it derives the Gravitational Wave mathematical description. It then analyzes the principal Astrophysical processes that can produce them and explains how they can be observed. After an overview of the current and future detectors, it finally presents the wavefront model for the GWs emitted from binary mergers.

Chapter 2 presents the Cosmological Standard Model used to describe the Universe on large scales. It then focuses on the Large Scale Structures and their evolution and distribution, also explaining what the gravitational lensing is. The Power Spectrum and the Angular Power Spectrum are then introduced as important statistical tools to analyze these quantities. Finally, it provides an overview on the use of Gravitational Waves to study Cosmology.

Chapter 3 introduces some statistical techniques used to link observations with theoretical models. In particular, it firstly describes how it is possible to estimate parameters from data and then it focuses on the Fisher matrix analysis. This is used to forecast the sensitivity of future instruments in determining the parameter values without having information about the data; other forecasting techniques are briefly introduced. The case of the Angular Power Spectrum forecasting is finally studied.

Chapter 4 combines the tools introduced in the previous Chapters to deeply analyze the paper from Namikawa, Nishizawa, Taruya. It firstly shows how an anisotropy estimator can be constructed and how its Angular Power Spectrum can be derived from the matter and lensing ones. It then performs the study of the errors associated to it; to do so, the Angular Power Spectrum Fisher matrix is calculated. The numerical implementation of the estimator Angular Power Spectrum is then described. This is not reported in the paper and it has therefore been necessary to fully derive it in order to construct a useful statistical tool. Its realization has been completed but it has to be improved, because some approximations have to be overcome . This will be done in future works, together with the numerical implementation of the Fisher matrix and of the error analysis.

The task of this work has been to construct a groundwork over which a future research project could be set up. The method presented to study Gravitational Waves without redshift information can provide a new way to deepen the knowledge both of Cosmology and Astrophysics, placing itself on the ground of a new, surely growing, field of research: the multi messenger Astronomy. It would therefore probably provide interesting achivements in the next future.

Chapter 1

What are Gravitational Waves?

This Chapter presents a short review of some of the main aspects about Gravitational Waves: how they are derived from General Relativity and their mathematical description (Sec. 1.1), the Astrophysical processes that can produce them (Sec. 1.2) and how they can be detected and analyzed (Sec. 1.3).

1.1 Gravitational Wave mathematical description

1.1.1 General Relativity overview

In modern physics, General Relativity (GR) is the most reliable theory used to explain how matter and energy affect spacetime. The core of GR is the description of gravity, which is a property of spacetime itself, strictly connected with its curvature. When matter is present, it warps spacetime geometry: this can be mathematically described using the metric.

When spacetime is flat, its intervals can be measured using the Minkowski metric

$$ds^2 = -c^2 dt^2 + dx^2 + dy^2 + dz^2$$
$$= \eta_{\mu\nu} dx^\mu dx^\nu \ , \tag{1.1}$$

where ds^2 is the invariant line element and $x^\mu = (ct, x, y, z)$ are the 4d spacetime cartesian coordinates; $\eta_{\mu\nu}$ is a symmetric matrix called the metric: when expressed in cartisian coordinates, $\eta_{\mu\nu} = (-1, 1, 1, 1)$. c is the speed of light; from now on in this work, it will be considered $c = 1$ and $G = 1$ for the universal gravity constant.

When spacetime curvature is different from 0, the generic metric will be given by

$$ds^2 = g_{\mu\nu} dx^\mu dx^\nu \ , \tag{1.2}$$

where $g_{\mu\nu}$ is still symmetric and it depends on the geometry coordinates; in fact, it can be derived using the scalar product between the basis vectors[1]

$$\mathbf{e}_\mu = \frac{\partial}{\partial x^\mu}$$
$$\Rightarrow g_{\mu\nu} = \mathbf{e}_\mu \cdot \mathbf{e}_\nu \ . \tag{1.3}$$

When $\mathbf{e}_\mu \cdot \mathbf{e}_\nu = 0$, the basis system is orthogonal and the metric is diagonal. It is always possible to locally transform the metric $g_{\mu\nu}$ in the Minkowski metric $\eta_{\mu\nu}$;

---

[1]In this work, 3d vectors are written in **bold** character.

this is assured by the Local Flatness Theorem (see [66] and [28]): when an arbitrary coordinate system $\{x^\mu\}$ and an arbitrary point P in spacetime are given, it is always possible to find another locally intertial coordinate system $\{x^{\bar\mu}\}$ in which

- $g_{\bar\mu\bar\nu}(P) = \eta_{\bar\mu\bar\nu} \quad \forall \bar\mu, \bar\nu$

- $\dfrac{\partial g_{\bar\mu\bar\nu}(P)}{\partial x^{\bar\rho}} = 0 \quad \forall \bar\mu, \bar\nu, \bar\rho$

- $\dfrac{\partial^2 g_{\bar\mu\bar\nu}(P)}{\partial x^{\bar\rho}\partial x^{\bar\sigma}} \neq 0$

The metric second order derivative $\partial^2 g_{\bar\mu\bar\nu}(P)/\partial x^{\bar\rho}\partial x^{\bar\sigma}$ has 100 freedom degrees, 20 of which canot be reduced to 0 using the coordinate transformation. They characterize the geometry deviation from flatness and they can be described using the Riemann tensor $R^\mu_{\nu\rho\sigma}$.

After having defined the metric connection, or Christoffel symbol

$$\Gamma^\sigma_{\mu\nu} = \frac{1}{2} g^{\sigma\rho} (\partial_\mu g_{\rho\nu} + \partial_\nu g_{\rho\mu} - \partial_\rho g_{\mu\nu}) \ , \tag{1.4}$$

thanks to the study of the covariant derivatives in a curved spacetime (see [66] and [28] for a complete derivation), the Riemann tensor follows from the calculation of the commutator between two covariant derivatives. It results to be

$$R^\sigma_{\mu\rho\nu} = \partial_\rho \Gamma^\sigma_{\mu\nu} - \partial_\nu \Gamma^\sigma_{\mu\rho} + \Gamma^\sigma_{\alpha\rho} \Gamma^\alpha_{\mu\nu} - \Gamma^\sigma_{\alpha\nu} \Gamma^\alpha_{\mu\rho} \ . \tag{1.5}$$

It is antisymmetric in the last two indexes and it has 20 freedom degrees, the same of the metric second order derivative.

Given the Riemann tensor, the Ricci tensor $R_{\mu\nu} = R^\lambda_{\mu\lambda\nu}$ is defined by contracting its first and third index; its trace $R = g^{\mu\nu} R_{\mu\nu}$ is called Ricci scalar. The Ricci tensor has 10 freedom degrees and describes the isotropic deformation of spacetime; the anisotropic one is given by the Weyl tensor, defined as the traceless part of the Riemann tensor.

$R_{\mu\nu}$ and R can be used to define the Einstein tensor

$$G_{\mu\nu} = R_{\mu\nu} - \frac{1}{2} R g_{\mu\nu} \ , \tag{1.6}$$

which satisfies the so called contracted Bianchi identity $\nabla^\mu G_{\mu\nu} = 0$.

Einstein equations

Einstein equations connect spacetime geometry with matter and energy distribution. The first one is expressed by the Ricci tensor $R_{\mu\nu}$, symmetric in its 2 index; to describe the second one another symmetric 2 index tensor is therefore required. As explained in [66], this could be done by the energy-momentum tensor: its formulation depends on the kind of matter involved.

The easiest case is the dust fluid: it is characterized by zero pressure and its comoving[2] matter-energy density $\rho = mn$, where m is the particles mass (if all of them have the same) and n is the comoving particle number density. Setting the

---

[2]In GR, "comoving to something" means "in a reference system at rest with it".

4-velocity as u^μ, the dust fluid energy-momentum tensor can be defined (see [66] and [28] for details) as

$$T^{\mu\nu} = \rho u^\mu u^\nu \; . \tag{1.7}$$

The tensor $T^{\mu\nu}$ is symmetric and each of its components plays a different role: $T^{00} = mn(u^0)^2$ is the matter-energy density, $T^{ij} = mnu^iu^j$ is the momentum flux, $T^{0i} = T^{i0} = mnu^0u^i$ is the matter-energy flux, which can also be seen as the impulse density.

Eq. (1.7) can be generalized to the case of perfect fluid: it is characterized by its density ρ and its isotropic pressure p and it has zero viscosity, zero anisotropic stress and no heat conduction. Its covariant energy-momentum tensor can be calculated (see [66] and [28]) as

$$T^{\mu\nu} = (p + \rho)u^\mu u^\nu + g^{\mu\nu}p \; . \tag{1.8}$$

It is possible to define $\nabla_\mu T^{\mu\nu} = 0$ where ∇_μ as the covariant derivative, so the energy-momentum tensor is locally conserved. When spacetime is flat, $\nabla_\mu = \partial_\mu$ and the tensor is globally conserved; in this case, the $\nu = 0$ component represents the energy conservation, while the $\nu = i$ conserves the i linear momentum component.

At this point, a set of second order differential equations can be built (see [66] and [28]): these are called Einstein equations, and they are given by

$$R_{\mu\nu} - \frac{1}{2}Rg_{\mu\nu} = 8\pi T_{\mu\nu} \; , \tag{1.9}$$

where the constant $8\pi = 8\pi G/c^4$ depends on having set the Einstein equations equal to the Poisson equation in the limit of weak gravitational field.

Since eq. (1.9) contains on the left hand side only the Ricci tensor and it does not depend on the Weyl one, it does not define completely and uniquely the spacetime curvature. In fact, it only describes the gravitational sources distribution (thanks to the link with the energy-momentum tensor) and the local deformation; initial or boundary contidions would be required to specify also spacetime deformations due to non local effect (e.g. tidal forces caused by a source in another place or Gravitational Waves generated by a source modification that happened before). These would be given by the Weyl tensor.

Eq. (1.9) can be modified adding the covariant term $\Lambda g_{\mu\nu}$: as one can see in [17] in details, Λ was originally called Cosmological constant and it has been studied both as a geometry term (when put on the left hand side of the equation) or as an energy contribution (when set on the right hand one). In the latter case, it can be described by the Equation of State (EoS) $p = -\rho$. Nowadays, this term corresponds and has been generalized to the effect of the so called Dark Energy component: understanding its EoS and its time evolution is one of the main tasks Cosmologists are working on.

1.1.2   Derivation of GW from GR

Einstein equations can be analitically solved considering the weak field limit and the linear approximation, where $g_{\mu\nu} = \eta_{\mu\nu} + h_{\mu\nu}$: $|h_{\mu\nu}| << 1$ is seen as a little perturbation over a flat Minkowski background. Eq. (1.5) can be rewritten as

$$R^\mu_{\nu\rho\sigma} = \partial_\rho \left[\frac{1}{2}g^{\mu\beta}(\partial_\nu g_{\beta\sigma} + \partial_\sigma g_{\beta\nu} - \partial_\beta g_{\nu\sigma}) \right] - \partial_\sigma \left[\frac{1}{2}g^{\mu\beta}(\partial_\nu g_{\beta\rho} + \partial_\rho g_{\beta\nu} - \partial_\beta g_{\nu\rho}) \right] \; ,$$
$$\tag{1.10}$$

substituting $g_{\mu\nu} = \eta_{\mu\nu} + h_{\mu\nu}$ this becomes

$$R^\mu_{\nu\rho\sigma} = \frac{1}{2} \left[\partial_\rho h^{\mu\beta}(\partial_\nu h_{\beta\sigma} + \partial_\sigma h_{\beta\nu} - \partial_\beta h_{\nu\sigma}) - \partial_\sigma h^{\mu\beta}(\partial_\nu h_{\beta\rho} + \partial_\rho h_{\beta\nu} - \partial_\beta h_{\nu\rho}) \right] \; .$$

Contracting the index β, eq. (1.10) can be rewritten at first order in $h_{\mu\nu}$ as

$$R^\mu_{\nu\rho\sigma} = \frac{1}{2}\left[\partial_\rho\partial_\nu h^\mu_\sigma + \partial_\rho\partial_\sigma h^\mu_\nu - \partial_\rho\partial_\beta h^{\mu\beta}h_{\nu\sigma} - \partial_\sigma\partial_\nu h^\mu_\rho + \partial_\sigma\partial_\rho h^\mu_\nu - \partial_\sigma\partial_\beta h^{\mu\beta}h_{\nu\rho})\right] \ .$$

Considering that $\partial_\beta h^{\mu\beta}$ is different from zero only if $\beta = \mu$, we further obtain that the previous equation can be written as

$$\begin{aligned} R_{\mu\nu\rho\sigma} &= \frac{1}{2}\left[\partial_\rho\partial_\nu h^\mu_\sigma + \partial_\rho\partial_\sigma h^\mu_\nu - \partial_\rho\partial_\mu h_{\nu\sigma} - \partial_\sigma\partial_\nu h^\mu_\rho - \partial_\sigma\partial_\rho h^\mu_\nu + \partial_\sigma\partial_\mu h_{\nu\rho}\right] \\ &= \frac{1}{2}\left[\partial_\rho\partial_\nu h^\mu_\sigma - \partial_\rho\partial_\mu h_{\nu\sigma} - \partial_\sigma\partial_\nu h^\mu_\rho + \partial_\sigma\partial_\mu h_{\nu\rho}\right] \ . \end{aligned}$$

Therefore, the Riemann tensor can be obtained as

$$R_{\mu\nu\rho\sigma} = \frac{1}{2}(\partial_\nu\partial_\rho h_{\mu\sigma} + \partial_\mu\partial_\sigma h_{\nu\rho} - \partial_\mu\partial_\rho h_{\nu\sigma} - \partial_\nu\partial_\sigma h_{\mu\rho}) \ . \tag{1.11}$$

Defining $h = \eta^{\mu\nu}h_{\mu\nu}$ and $\bar{h}_{\mu\nu} = h_{\mu\nu} - \frac{1}{2}\eta_{\mu\nu}h$, eq. (1.9) becomes

$$\Box\bar{h}_{\mu\nu} + \eta_{\mu\nu}\partial^\rho\partial^\sigma\bar{h}_{\rho\sigma} - \partial^\rho\partial_\nu\bar{h}_{\mu\rho} - \partial^\rho\partial_\mu\bar{h}_{\nu\rho} = -16\pi T_{\mu\nu} \ . \tag{1.12}$$

where $\Box = \eta_{\mu\nu}\partial^\mu\partial^\nu = \partial^\mu\partial_\mu$ is called d'Alambertian.

Eq. (1.12) has different formulation when defined in different gauges[3]; when the Lorentz gauge is set, $\partial^\nu\bar{h}_{\mu\nu} = 0$ and eq. (1.12) reduces to

$$\Box\bar{h}_{\mu\nu} = -16\pi T_{\mu\nu} \ . \tag{1.13}$$

Eq. (1.13) describes how GWs are generated by $T_{\mu\nu}$, which represents their source (see Sec. 1.2).

To study how GWs propagate, it is necessary instead to study the wave outside of the matter distribution (i.e. in the vacuum), where $T_{\mu\nu} = 0$. This leads to

$$\Box\bar{h}_{\mu\nu} = \left(-\partial_0^2 + \nabla^2\right)\bar{h}_{\mu\nu} = 0 \ . \tag{1.14}$$

It is important to underline that if different units are chosen and $c \neq 1$, in eq. (1.14) $-\partial_0$ becomes $-1/c^2\ \partial_0$; this implies that GWs travel with speed $v = c$.

GW tensor properties

Eq. (1.14) can be solved in each of its components $\mathsf{h}(x)$ ($x = x^\mu$) as a wave equation

$$\Box\mathsf{h}(x) = -\frac{\partial^2\mathsf{h}(x)}{\partial t^2} + \nabla^2\mathsf{h}(x) = 0 \ , \tag{1.15}$$

the solution of which (see [66] and [28]) is the plane wave $\mathsf{h}(x) = Be^{ik^\mu x_\mu}$, B being the amplitude and $k^\mu = (\omega, \mathbf{k})$. The latter is a null 4-vector[4]: in fact

$$\Box\mathsf{h}(x) = 0 \ , \tag{1.16}$$

---

[3]In GR, gauge is a map that links points on a perturbed space with points on the linear background (see [11] and [37]). There are many gauges that can be chosen, each of them useful to describe different situations. Lorentz gauge, as defined in [44], is the linear order approximation of the De Donder harmonic gauge: this is defined by $\partial_\mu g^{\mu\nu}\sqrt{-g} = 0$. Lorentz gauge can be seen in analogy to the Lorentz gauge of electromagnetism, in which $\partial_\mu A^\mu = 0$, $A^\mu = (\phi, \mathbf{A})$ being the 4-potential.

[4]In GR, 4-vectors a^μ are called spacelike when $a^\mu a_\mu > 0$, timelike when $a^\mu a_\mu < 0$ and null when $a^\mu a_\mu = 0$.

brings

$$\left(-\frac{\partial^2}{\partial x_0^2} + \frac{\partial^2}{\partial x_j^2}\right) B e^{ik^\mu x_\mu} = -\frac{\partial}{\partial x_0}(-Bik^0 e^{-ik^0 x_0 + ik^j x_j}) + \frac{\partial}{\partial x_j}(Bik^j e^{-ik^0 x_0 + ik^j x_j})$$

$$= -B^2(k^0)^2 + B^2(k^j)^2 e^{-ik^0 x_0 + ik^j x_j} \ , \tag{1.17}$$

which implies $-(k^0)^2 + (k^j)^2 = k^\mu k_\mu = 0$. The plane wave solution can be extended to $\bar{h}_{\mu\nu}$ defining $b_{\mu\nu}$ as the matrix containing all the amplitudes B of the various components. It is a 4×4 symmetric matrix [28], thanks to which GWs can be described as $\bar{h}_{\mu\nu} = b_{\mu\nu} e^{ik^\mu x_\mu}$.

As shown in [44], the coordinate transformation $x_\mu \to x_\mu + \xi_\mu$ can be performed without breaking the Lorentz gauge condition if $\Box \xi_\mu = 0$. The 4 functions ξ_μ can be therefore used to set conditions on the 6 independent components of $\bar{h}_{\mu\nu}$.

In particular, ξ_0 can be chosen in order to set $\mathrm{Tr}(\bar{h}_{\mu\nu}) = \eta^{\mu\nu}\bar{h}_{\mu\nu} = 0$ (i.e. traceless tensor). In this case, as [44] shows, the term $\bar{h} = \eta^{\mu\nu}\bar{h}_{\mu\nu}$ can be defined. Using the definitons of $\bar{h}_{\mu\nu}$ and h previously given, it can be transformed as

$$\bar{h} = \eta^{\mu\nu}\bar{h}_{\mu\nu} = \eta^{\mu\nu}\left(h_{\mu\nu} - \frac{1}{2}\eta_{\mu\nu}h\right) = h - \frac{1}{2}4h = -h \ . \tag{1.18}$$

When $\mathrm{Tr}(\bar{h}_{\mu\nu}) = \bar{h} = 0$, eq. (1.18) assures that also $h = 0$ and consequently $\bar{h}_{\mu\nu} = h_{\mu\nu}$.

The remaining 3 functions ξ_j are used to set $h_{0j} = 0$; in this way, the 0 component of the Lorentz gauge conditions is

$$-\partial^0 h_{00} + \partial^j h_{0j} = 0 \ , \tag{1.19}$$

and $\partial^0 h_{00} = 0$, i.e. h_{00} is constant in time. It represents the static part of the gravitational potential, due to the GW sources; because of the required time dependence of GWs, eq. (1.19) means that $h_{00} = 0$ for them. Consequently, also for the Lorentz gauge condition spatial components $\partial^j h_{ij} = 0$ is required.

Depending on all of this, the conditions set on GW tensor $h_{\mu\nu}$ are

- $h^{0j} = 0$,
- $\partial^j h_{ij} = 0$ to be tranverse,
- $h_i^i = 0$ to be traceless.

These define the Transverse-Traceless (TT) gauge, in which $h_{\mu\nu} = h_{\mu\nu}^{TT}$ has time component $h_{00}^{TT} = 0$ and space component h_{ij}^{TT}; $h_{\mu\nu}^{TT}$ is symmetric and has only 2 degrees of freedom: this displays the existence of two different polarizations.

The solutions in the TT gauge of eq. (1.13) are the plane waves defined by $h_{ij} = e_{ij}^A(\mathbf{k})e^{ik_\mu x^\mu}$. $\mathbf{k} = k^j$ is a vector along the propagation direction, while $e_{ij}^A(\vec{k})$ ($A = +, \times$) are called polarization tensors. Considering $\mathbf{u} \perp \mathbf{v} \perp \mathbf{k}$, they can be expressed as

$$\begin{cases} e_{ij}^+ = \mathbf{u}_i\mathbf{u}_j - \mathbf{v}_i\mathbf{v}_j \\ e_{ij}^\times = \mathbf{u}_i\mathbf{v}_j + \mathbf{v}_i\mathbf{u}_j \ . \end{cases} \tag{1.20}$$

It is possible to consider a single plane wave propagating in $\mathbf{n} = \mathbf{k}/|\mathbf{k}|$ direction: as seen in [44], its components lay on the $\mathbf{n}$ transverse plane because

$$\partial^j h_{ij} = \frac{\partial}{\partial x^j}(e_{ij}^p e^{-ik^0 x_0 + k^j x_j}) = ik^j(e_{ij}^p e^{ik^\mu x_\mu}) = 0 \ , \tag{1.21}$$

which implies $ik^j h_{ij} = 0$ and $n^j h_{ij} = 0$.

Thanks to this property, when $\mathbf{n}$ is along the z axis, h_{ij}^{TT} can be written as

$$
h_{ij}^{TT} = \begin{pmatrix} h_+ & h_\times & 0 \\ h_\times & -h_+ & 0 \\ 0 & 0 & 1 \end{pmatrix}_{ij} \cos(\omega(t-z)) .
\tag{1.22}
$$

The values h_+ and $h_\times$ are the amplitudes of the two polaritazions. In this case, $\mathbf{u} = x$ and $\mathbf{v} = y$, so the polarization tensors are represented by

$$
e_{ij}^+ = \begin{pmatrix} 1 & 0 & 0 \\ 0 & -1 & 0 \\ 0 & 0 & 0 \end{pmatrix}_{ij} \qquad e_{ij}^\times = \begin{pmatrix} 0 & 1 & 0 \\ 1 & 0 & 0 \\ 0 & 0 & 0 \end{pmatrix}_{ij} .
\tag{1.23}
$$

Under these conditions, GWs in the 4-interval ds^2 are (see [44])

$$
\begin{aligned}
ds^2 = &- dt^2 + dz^2 + [1 + h_+ \cos(\omega(t-z))]dx^2 + \\
&+ [1 - h_+ \cos(\omega(t-z))]dy^2 + 2h_\times \cos(\omega(t-z))dxdy .
\end{aligned}
\tag{1.24}
$$

Fourier representation

In the TT gauge, the GW equation of motion is given by $\Box h_{ij}^{TT} = 0$ and h_{ij}^{TT} can be expanded [44] as

$$
h_{ij}^{TT}(x) = \int \frac{d^3k}{(2\pi)^3} \left[\mathcal{A}_{ij}(\mathbf{k})e^{ik^\mu x_\mu} + \mathcal{A}_{ij}^*(\mathbf{k})e^{-ik^\mu x_\mu} \right] ,
\tag{1.25}
$$

being $k^\mu = (\omega, \mathbf{k})$ and $\omega = 2\pi f$, where $f > 0$ is the physical frequency. In the TT gauge $\mathcal{A}_i^i(\mathbf{k}) = 0$ and $k^i \mathcal{A}_{ij}(\mathbf{k}) = 0$. When the propagation direction is well defined as $\mathbf{n}_0$ (e.g. when from Earth a single GW source is observed), it is possible to set (see [44])

$$
\mathcal{A}_{ij}(\mathbf{k}) = A_{ij}(f)\delta^{(2)}(\mathbf{n} - \mathbf{n_0}) .
\tag{1.26}
$$

When observing GWs, the quantity which is measured is f; therefore, in eq. (1.25) it is possible to transform $d^3k = |\mathbf{k}|^2 d|\mathbf{k}|d\Omega = (2\pi)^3 f^2 df d\Omega$. Moreover, indicating the integration over the solid angle as $d\cos\theta d\phi = d^2\mathbf{n}$, eq. (1.25) can be rewritten[5] as

$$
h_{ij}^{TT}(x) = \int f^2 \, df \int d^2\mathbf{n} \left(\mathcal{A}_{ij}(f, \mathbf{n})e^{-2\pi i f(t - \mathbf{n}\cdot\mathbf{x})} + \text{c.c.} \right) .
\tag{1.27}
$$

When the GW has propagation direction $\mathbf{n}_0$, the plane wave components are different from zero only in the plane transverse to $\mathbf{n}_0$; defining the indices $a, b = 1, 2$ over it, the wave can therefore be described as

$$
h_{ab}^{TT}(t, \mathbf{x}) = \int_0^\infty \left(\tilde{h}_{ab}(f, \mathbf{x})e^{-2\pi i f t} + \tilde{h}_{ab}^*(f, \mathbf{x})e^{2\pi i f t} \right) df ,
\tag{1.28}
$$

where $\tilde{h}_{ab}(f, \mathbf{x})$ is the Fourier transform, defined using eq. (1.26)

$$
\begin{aligned}
\tilde{h}_{ab}(t, \mathbf{x}) &= f^2 \int \mathcal{A}_{ab}(f, \mathbf{n})e^{2\pi i f t \mathbf{n}\cdot\mathbf{x}} \, d^2\mathbf{n} \\
&= f^2 A_{ab}(f)e^{2\pi i f t \mathbf{n_0}\cdot\mathbf{x}} .
\end{aligned}
\tag{1.29}
$$

---

[5]In this work, c.c. indicates the complex conjugate.

It can be extended to non-positive f setting $\tilde{h}_{ab}(-f, \mathbf{x}) = \tilde{h}_{ab}^*(f, \mathbf{x})$; in this way, eq. (1.28) can be rewritten in a more compact form as

$$h_{ab}^{TT}(t, \mathbf{x}) = \int_{-\infty}^{+\infty} \tilde{h}_{ab}(f, \mathbf{x}) e^{-2\pi i f t} \, df \ . \tag{1.30}$$

When the GW is studied in a specific place, e.g. at the detector location (see Sec. 1.3), the $\mathbf{x}$ dependence can be omitted from eq. (1.28), substituting $\tilde{h}_{ab}(f) = \tilde{h}_{ab}(f, \mathbf{x} = 0)$.

GW in curved spacetime

When the background metric is dynamical and curved, it can be written as $g_{\mu\nu} = \bar{g}_{\mu\nu}(x) + h_{\mu\nu}(x)$, where $h_{\mu\nu}$ represents the GW contribution and $|h_{\mu\nu}| << 1$. As [44] explains, this condition has to be satisfied in order to distinguish GWs from the background: $h_{\mu\nu}$ modifies the background curvature, but it is indistinguishable from it on a microscopic level. The only way to identify $h_{\mu\nu}$ separately from $\bar{g}_{\mu\nu}$ is thanks to the different scale and frequency that the two metrics have. As a matter of fact, the background is smooth and the GW scale λ is smaller compared to λ_{back}; at the same time, GWs can be considered as high frequency perturbations over a static (or with slow evolution) background. Even though $\lambda = c/f$, these two conditions are independent from one another because f_{back} and λ_{back} are uncorrelated. Detectors (see Sec. 1.3) can distinguish GWs over the background thanks to frequency variations in the gravitational field.

Einstein equations in curved space can be expanded around $\bar{g}_{\mu\nu}$. Ricci tensor can be separated into several contributions such as $\bar{R}_{\mu\nu} + R_{\mu\nu}^{(1)} + R_{\mu\nu}^{(2)} + ...$ Each of them depend in a different way on $h_{\mu\nu}$ and consequently on the GW frequency: for example, $\bar{R}_{\mu\nu}$ depends only on $\bar{g}_{\mu\nu}$, therefore it contains only low frequency modes[6]; $R_{\mu\nu}^{(1)}$ is linear in $h_{\mu\nu}$ and is characterized by the high frequency modes; $R_{\mu\nu}^{(2)}$ is quadratic in $h_{\mu\nu}$ and contains both high and low frequency modes: for instance, the quadratic term $h_{\mu\nu}h_{\rho\sigma}$ can combine two high wave vectors $\mathbf{k}_1$ and $\mathbf{k}_2 \simeq -\mathbf{k}_1$ obtaining a low frequency one (see [44] for details).

This is crucial since Einstein equations can be split[7] into two separated sets:

$$\bar{R}_{\mu\nu} = -\left[R_{\mu\nu}^{(2)}\right]^{LOW} + 8\pi\left(T_{\mu\nu} - \frac{1}{2}g_{\mu\nu}T\right)^{LOW} \ , \tag{1.31}$$

includes the low frequency modes, while

$$R_{\mu\nu}^{(1)} = -\left[R_{\mu\nu}^{(2)}\right]^{HIGH} + 8\pi\left(T_{\mu\nu} - \frac{1}{2}g_{\mu\nu}T\right)^{HIGH} \ , \tag{1.32}$$

includes the high frequency ones.

---

[6]The high and low frequency modes introduced studying the Ricci tensor are both higher than the background modes; the author of [44] shows in fact that the background frequency is even lower than the low frequency modes considered in the Ricci tensor.

[7]The Einstein equations can be written as

$$R_{\mu\nu} \simeq \bar{R}_{\mu\nu} + R_{\mu\nu}^{(1)} + R_{\mu\nu}^{(2)} = 8\pi\left(T_{\mu\nu} - \frac{1}{2}g_{\mu\nu}T\right)^{LOW+HIGH} \ ,$$

therefore the low frequency contributions can be gathered into $\bar{R}_{\mu\nu} + R_{\mu\nu}^{(2)} = 8\pi(T_{\mu\nu} - 1/2 \cdot g_{\mu\nu}T)^{LOW}$, while the high ones into $R_{\mu\nu}^{(2)} = 8\pi(T_{\mu\nu} - 1/2 \cdot g_{\mu\nu}T)^{HIGH}$.

It can be shown (see [44] for details) that from eq. (1.31) the GW energy-momentum tensor can be derived, while eq. (1.32) is a wave equation that describes how $h_{\mu\nu}$ propagates over the background. Integrating the high frequency modes the background dynamic can be derived too: this is characterized by the coarse grain Einstein equations

$$\bar{R}_{\mu\nu} - \frac{1}{2}\bar{g}_{\mu\nu}\bar{R} = 8\pi\left(\bar{T}_{\mu\nu} + t_{\mu\nu}\right) \,, \tag{1.33}$$

where $\bar{T}_{\mu\nu}$ is the effective energy-momentum tensor

$$\left\langle T_{\mu\nu} - \frac{1}{2}g_{\mu\nu}T \right\rangle = \bar{T}_{\mu\nu} - \frac{1}{2}\bar{g}_{\mu\nu}\bar{T} \,, \tag{1.34}$$

obtained thanks to the $\langle ... \rangle$ spatial average over many wavelenghts. The tensor $t_{\mu\nu}$ instead describes how GWs affect the curvature. The effect is the same of a matter distribution having

$$t_{\mu\nu} = -\frac{1}{8\pi}\left\langle R_{\mu\nu}^{(2)} - \frac{1}{2}g_{\mu\nu}R^{(2)} \right\rangle \,. \tag{1.35}$$

The tensor $t_{\mu\nu}$ is due both to physical and gauge modes: the first ones depend on the GW energy, while the second ones are linked with the coordinate system choice. When the Lorentz one is chosen, gauge modes are eliminated and, as shown in [44], after some calculations

$$t_{\mu\nu} = \frac{1}{32\pi}\left\langle \partial_\mu h_{\alpha\beta}\partial_\nu h^{\alpha\beta} \right\rangle \,. \tag{1.36}$$

The tensor $\bar{T}_{\mu\nu} + t_{\mu\nu}$ is covariant but the two tensors can not be conserved separately: this is due to the energy and momentum exchange between GWs and the background curvature sources. Using $t_{\mu\nu}$, the GW energy flux for unit time dt and area $dA = r^2 d\Omega$ can be calculated; when the background metric can be considered flat and the TT gauge can be assumed (i.e. at sufficiently small scales or far enough from every matter source), $\bar{T}_{\mu\nu} = 0$, $D^\mu \simeq \partial^\mu$ and consequently $\partial^\mu t_{\mu\nu} = 0$ and $t_{\mu\nu}$ is conserved. Therefore defining the energy inside a volume V as

$$\frac{dE}{dt} = \int_V dA\, t^{00} \quad \text{where} \quad t^{00} = \frac{1}{32\pi}\left\langle \partial^0 h_{ij}^{TT} \partial^0 h_{ij}^{TT} \right\rangle \,,$$

being $\langle ... \rangle$ a time average. It is possible therefore to find

$$\frac{dE}{dt} = \frac{r^2}{32\pi}\int \left\langle \dot{h}_{ij}^{TT}\dot{h}_{ij}^{TT} \right\rangle d\Omega \,, \tag{1.37}$$

that can be rewritten as

$$\frac{dE}{dA\,dt} = \frac{1}{16\pi}\left\langle \dot{h}_+^2 + \dot{h}_\times^2 \right\rangle \,. \tag{1.38}$$

When considering the total flux integrated in time, the time average $\langle ... \rangle$ in eq. (1.38) can be omitted and

$$\frac{dE}{dA} = \int_{-\infty}^{+\infty} (\dot{h}_+^2 + \dot{h}_\times^2)\, dt = h_+^2 + h_\times^2 \,.$$

If $h_{+,\times}$ are expanded as in eq. (1.28), the total flux over a unit area is

$$\frac{dE}{dA} = \frac{1}{16\pi}\int_{-\infty}^{+\infty} (2\pi f)^2 \left(|\tilde{h}_+(f)|^2 + |\tilde{h}_\times(f)|^2\right) df$$

$$= \frac{\pi}{2}\int_0^{+\infty} f^2 \left(|\tilde{h}_+(f)|^2 + |\tilde{h}_\times(f)|^2\right) df \quad \text{using the symmetry } f \to -f \,,$$

so that one finds

$$\frac{dE}{df} = \frac{\pi}{2} f^2 r^2 \int (|\tilde{h}_+(f)|^2 + |\tilde{h}_\times(f)|^2)\, d\Omega \ . \tag{1.39}$$

The quantity dE/df describes the GW spectrum that can be detected (see Sec. 1.3); when integrated over $f > 0$ it gives the total energy.

Similarly, the momentum flux can be calculated (see [44] for details) as

$$\frac{dP^k}{dt} = -\frac{1}{32\pi} r^2 \int d\Omega \, \langle \dot{h}_{ij}^{TT} \partial^k h_{ij}^{TT} \rangle \ . \tag{1.40}$$

1.2   Gravitational Wave sources

1.2.1   GW emission

GW generation is studied in the linearized theory. Spacetime around the sources can be considered approximately flat if the gravitational field is sufficiently weak; this also implies that the system can be described using the Newtonian approximation.

Eq. (1.13) describes Einstein equations in Lorentz gauge in presence of matter. It can be solved using the Green functions: for a given system, they are defined as the output to a point-like δ_D input. In fact (see [66] and [28]), to solve the generic equation

$$-\frac{\partial^2}{\partial t^2} F(x) + \nabla^2 F(x) = j(x) \ , \tag{1.41}$$

where $j(x^\mu) = \delta_D(t)\delta^{(3)}(\mathbf{x})$ is a scalar field. The homogeneous part

$$-\frac{\partial^2}{\partial t^2} G(x) + \nabla^2 G(x) = 0 \tag{1.42}$$

which in spherical coordinates becomes

$$-\frac{\partial^2}{\partial t^2} G(x) + \frac{1}{r^2}\frac{\partial}{\partial r}\left(r^2 \frac{\partial G(x)}{\partial r}\right) = 0 \ , \tag{1.43}$$

has to be solved. The solution to eq. (1.43) is $G(x) = \frac{1}{r}[O(t-r) + I(t+r)]$, obtained by the superposition of a wave $O(t-r)$ propagating from the source to infinity with $v = c$ (causal solution) and another wave $I(t+r)$ propagating from infinity to the source: this one has no physical meaning and can be ignored. The explicit expression of $G(x)$ and the non homogeneous solution are reached integrating over a small volume V in the limit of $r \to 0$

$$\lim_{r\to 0}\int_V \left[-\frac{\partial^2}{\partial t^2} G(x) + \nabla^2 G(x)\right] d^3x = \lim_{r\to 0}\int_V d^3x\, j(x^\mu) = \delta_D(t) \ . \tag{1.44}$$

Considering that

- if in $r \to 0$ the function $O(t-r)$ does not diverge, $G(x) \simeq 1/r$ and $\partial^2 G(x)/\partial t^2 \simeq 1/r$;

- $d^3x \simeq r^2 dr$ so $d^3x \cdot \partial^2 G(x)/\partial t^2 \to 0$ when $r \to 0$;

- using the divergence theorem

$$\lim_{r\to 0}\int_V d^3x \nabla^2 G(x) = \lim_{r\to 0}\int_{\partial V} ds\, \mathbf{n} \cdot \nabla G \ , \tag{1.45}$$

the solution of eq. (1.44) defines the Green function; in fact

$$\lim_{r \to 0} \int_{\partial V} ds \, \mathbf{n} \cdot \nabla G \simeq \lim_{r \to 0} 4\pi r^2 \left[\frac{1}{r^2} O(t-r) + \frac{1}{r} \frac{dO(t-r)}{dr} \right] = -4\pi O(t) = \delta(t) \ . \tag{1.46}$$

Therefore, considering $r = |\mathbf{x} - \mathbf{x}_e|$ between the positions of the observer and the emission of the signal, eq. (1.46) can be used to define

$$G(x) \ = \ \frac{1}{r} O(t-r) \ = \ -\frac{\delta_D(t - t_e - |\mathbf{x} - \mathbf{x}_e|)}{4\pi |\mathbf{x} - \mathbf{x}_e|} \ , \tag{1.47}$$

where t is the time of the observation and t_e the time of the emission. Finally, the solution eq. (1.41) is found (see [66] and [28]) by convolving the Green functions $G(x)$

$$F(t, \mathbf{x}) = \int dt_e d\mathbf{x}_e \, G(t - t_e, \mathbf{x} - \mathbf{x}_e) j(t_e, \mathbf{x}_e) = -\frac{1}{4\pi} \int d^3\mathbf{x} \frac{|j(t_e, \mathbf{x}_e)|_{\text{rit}}}{|\mathbf{x} - \mathbf{x}_e|} \ . \tag{1.48}$$

In the specific case of GW production (see [44]), if $G(x - x')$ is a solution of $\Box G(x - x') = \delta_D^{(4)}(x - x')$, then the solution of eq. (1.13) is

$$\begin{aligned} \bar{h}_{\mu\nu}(x) \ &= \ -16\pi \int d^4 x' \, G(x - x') T_{\mu\nu}(x') \\ &= 4 \int d^3\mathbf{x}' \frac{1}{|\mathbf{x} - \mathbf{x}'|} T_{\mu\nu}(t - |\mathbf{x} - \mathbf{x}'|, \mathbf{x}') \ . \end{aligned} \tag{1.49}$$

Using the local conservation of $T_{\mu\nu}$, one can demonstrate (see [66] and [28]) that

$$\bar{h}^{ij}(t, \mathbf{x}) \to_{r \to \infty} \frac{2}{r} \ddot{\mathcal{I}}(t-r) \quad \text{where} \quad \ddot{\mathcal{I}}^{ij}(t) = \int d^3 x \, \rho(t, \mathbf{x}') x^i x^j \ , \tag{1.50}$$

is the mass tensor, which describes how the mass is distributed depending on the time second derivative. To have GW production it is instead necessary the variation of the mass distribution second derivative in time, namely the mass quadrupole; this can happen in many different ways, as described in Sec. 1.2.2.

GW emission implies a loss of energy and momentum from the source, which are carried away by the qudrupole radiation. GWs have no monopole or dipole radiation (see [44] for details) in the Lorentz gauge.

1.2.2 Different kinds of GW sources

GW sources can be differentiated (see [36] and [61]) between transient and continuous. The first kind includes compact objects binary coalescences and bursts (i.e. supernovae explosions, unstable pulsar glitches and soft γ repeaters); the second is formed by periodic GW emittors, such as spinning Neutron Stars (NS), and from the GW stochastic background of Astrophysical and Cosmological origin (see e.g. [14]).

Each of these sources can be analyzed using a particular approach.

Binary coalescences (which will be better described later) are the best modeled GW sources; their signal is anisotropic (see Sec. 1.3) and can be divided into 3 phases:

- the inspiral, a small periodic emission lasting over thousands of years while the two objects get closer,

- the merger between the objects, lasting less than 1 s,

- the ring down, less than 1 s in which the "new" object stabilizes.

Binaries emit GWs really efficiently ($\simeq 10\%$ of the mass can be lost during the merging phase), with frequencies f that increase while the objects move faster and faster approaching one another. $\dot{f}$ depends on the chirp mass (see Sec. 1.3 for details), defined as

$$M_{\text{chirp}} = \frac{(m_1 m_2)^{3/5}}{(m_1 + m_2)^{1/5}} = \mu^{3/5} M^{2/5} \ , \tag{1.51}$$

where m_1 and m_2 are the masses of the two objects, $M = m_1 + m_2$ the total mass and $\mu = m_1 m_2 / (m_1 + m_2)$ is the reduced mass.

The frequency f of the last stable orbit depends instead on $M_\odot / M$, where $M_\odot =$ solar mass $= 1.99 \cdot 10^{30}$ kg.

This kind of GW sources is studied using templates (see [36] and [55]): the signal is analitically (for the inspiral phase) or numerically (for the merger) computed and superimposed to data: the match between them is achieved thanks to the parameters choice. The ring down phase is less understood so far: after the merger, a perturbed object has to stabilize but the way it does it depends on its progenitors (see later for details).

GWs can be also generated by different kinds of bursts: in this case their signal is not well modeled. To study them (see [36] and [41]), relevant peaks are searched in the data sets thanks to a coherent analysis between different observatories. Moreover, since both binary coalescences and bursts can be followed by Electro-Magnetic (EM) emission, it is possible to look for GW signals when and where a relevant EM event has happened (short γ ray bursts, core collapse supernovae, kilonovae etc.).

The study of continuous GW sources is totally different. Periodic signals can be generated by accretion disks, spinning NS, NS with misshapen shape or magnetic field: in fact, asymmetries assess the presence of a mass quadrupole.

On the other hand, it is possible to identify the presence of GW background emissions. One of these is due to unresolved binary mergers: its amplitude depends on the binary merger rate. For example, in [19] the NS-NS merger rate is estimated: it is related to the current merger rate, in turn calculated extrapolating the Milky Way one to the Universe average, and to its time-evolution. NS-NS merger rate will be deeper analized in Chapter 2.

Finally, a GW Cosmological background exists. It is generated (details can be found in [11] and [37]) by spatial tensorial fluctuations around the Robertson Walker metric, described (see Chapter 2 for detailed explanation) by

$$ds^2 = -dt^2 + a^2(t)[(\delta_{ij} + h_{ij})dx^i dx^j] \ , \tag{1.52}$$

where h_{ij} is the symmetric traceless and transverse tensor which describes the GW. This kind of GWs is a smoking gun signature of Inflation (see e.e. [26]), the accelerated expansion phase theorized at the beginning of the Universe history. Differently from Astrophysical GWs, their origin can be linked to primordial quantum oscillations of the spacetime itself and not to a mass quadrupole distribution. They have not been detected yet: they are really weak and their frequency is not directly observable from Earth with the present experiments (see Sec. 1.3). If space inteferometers such as LISA (see e.g. [9] and [10] will ever measure this kind of GWs, it will be a smoking gun of
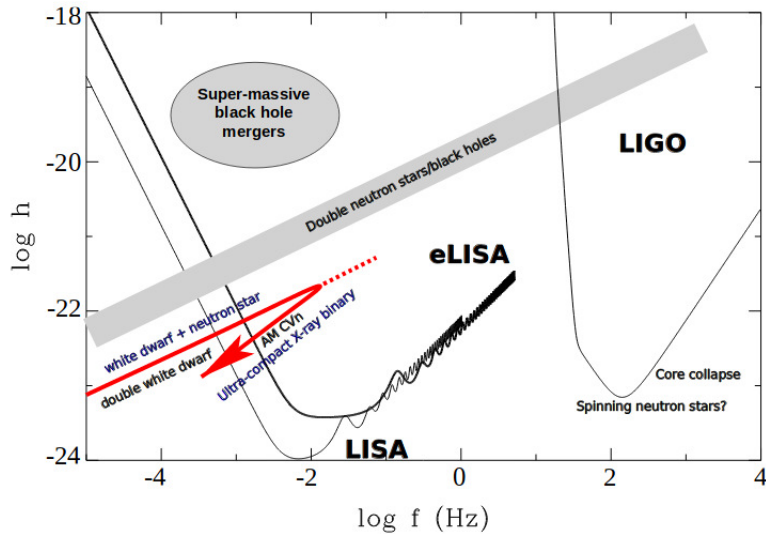
Figure 1.1: Sensitivity limits of existing and future GW detectors compared to frequencies of potential GW sources. Image from [57].

Inflation (see e.g. [14] and [26]), since this is nowadays the only theory predicting a Cosmological GW emission sufficient to be detected.

In this work, only GWs from compact objects binary mergers will be taken into account.

Binary systems

Binary systems are particularly interesting when studying GWs, not only because their orbital evolution is entirely due to the efficient gravitational emission (see [57]), but particularly because the GW frequencies some of them emit fall in the detectable range of already existing instruments (see Figure 1.1 and Sec. 1.3).

Binary systems with this property are formed by compact objects, i.e. they are NS-NS, NS-Black Holes (BH) or BH-BH systems. These are the remnants of pre-existing massive stars that at the end of their life had evolved through a core collapse Supernova (SN). As [67] and [54] explain in details, when a star with mass $m > 8M_\odot$ has completed all the burning cycles allowed in its evolution (i.e. the core is composed by elements of the iron group) the radiation pressure is no more able to balance gravity. Consequently the core collapses and a shock wave is propagated outside the star: external layers are ejected while in the core starts a neutronization process[8]. Neutrons become degenerate and the pressure they exert succeeds in constrasting the gravitational collapse if $m_{core} \lesssim 3.2M_\odot$. In this case a NS is generated; its density is about 10^{15} g/cm^3 while other characteristics are reported in Tab. 1.1. If the degenerate pressure is not enough to counterbalance gravity, the collapse continues and creates a BH, whose chacateristics are reported in Tab. 1.1. The limit of the collapse is the event horizon, defined (see [67] and [54]) as

$$R_S = 2\frac{GM}{c^2} \ . \tag{1.53}$$

---

[8]When the density is $\rho \simeq 10^7$ g/cm^3 electrons and protons combine to form neutron and neutrinos thanks to the inverse β-decay $e^- + p^+ \to n + \nu_e$.

	m	R	$R/R_{S_{1M_\odot}}$
Neutron Star	$1 - 1.5 M_\odot$	10 km	3
Black Hole	$3 - 30 M_\odot$	3 km	1

Table 1.1: Typical values for NS and BH mass m, radius R and R/R_S calculated for $1M_\odot$ objects. Values from [67] and [54].

When massive stars m_1 and m_2 are found in binary systems, their evolution is a little bit different. As [57] describes, the more massive m_1 evolves faster: after the hydrogen (H) burning phase, it expands and fills its Roche lobe[9]. Mass transfer begins, m_1 loses its H envelope and let m_2 acquire mass and angular momentum, increasing its rotational speed. m_1 continues its faster evolution until the SN explosion, leaving a NS or a BH; m_2 evolution is slower and can form a common envelope around its core and m_1 but in the end it also concludes with the SN explosion and the NS or BH creation.

The subsequent orbital evoltion is completely due to GW emission. The mass quadrupole needed (see Sec. 1.2.1) depends in this case on the orbital motion of the objects componing the system: as [60] describes using the Newtonian approximation, if the objects have the same mass m and move in the (x, y) plane with orbital radius R and angular velocity ω, their quadrupole momentum components are

$$
\begin{aligned}
\mathcal{I}_{xx} &= mR^2 \cos(2\omega t) \\
\mathcal{I}_{yy} &= - mR^2 \cos(2\omega t) \\
\mathcal{I}_{xy} &= mR^2 \sin(2\omega t) \; .
\end{aligned}
\tag{1.54}
$$

It can be showed (see [60] and [44]) that GWs emitted have $\omega_{GW} = 2\omega$.

The general expression for the radiation field is

$$
h_{ij}^{TT} = \frac{2}{r} \ddot{\mathcal{I}}_{ij} \; ,
\tag{1.55}
$$

thus perpendiculary to the orbital plane (i.e. in z direction) h_{ij}^{TT} has a circular polarization (see [60]) whose components are

$$
\begin{aligned}
h_+ &= - 8m\omega^2 \frac{R^2}{r} \cos(2\omega t) \\
h_\times &= 8m\omega^2 \frac{R^2}{r} \sin(2\omega t) \; .
\end{aligned}
\tag{1.56}
$$

Along the x axis instead (and for any other direction in the orbital plane because of the existing symmetry) the radiation is completely +polarized, having amplitude $h_+ = 4m\omega^2 R^2/r$ weaker than the previous case. Intermediate cases present both h_+ and $h_\times$, combined to give rise to an elliptical polarization.

If the object masses are unequal, the previous description is still valid if m is changed with the chirp mass defined in eq. (1.51).

The quadrupole expression in eq. (1.54) can be used to calculate the gravitational

---

[9]In the binary system formed by m_1 and m_2, the Roche lobe is the equipotential surface that divides the two regions where the gravitational potential is dominated respectively by m_1 or m_2. When a star fills its Roche lobe, part of its mass can transit in the other lobe because of the gravity attraction of the companion, determining an accretion process over it.

luminosity of the source. As [60] demonstrates, this is

$$
\begin{aligned}
L &= \frac{dE}{dt} = \frac{16}{5}m^2R^4\omega^6 \quad \text{but in Newtonian dynamic } R^3 = \frac{m}{4\omega^2} \\
\Rightarrow L &= \frac{1}{20}(2m\omega)^{10/3} = \frac{1}{20}(m\omega_{GW})^{10/3} \ .
\end{aligned}
\tag{1.57}
$$

The energy the system emits is taken from the orbital energy $E = -m\omega^2R^2$; GW emission implies then the reduction of ω and R, bringing the binary system progressevely to the merger and the formation of a new compact object in the ring down phase. If the progenitors are BH this phase can be interpreted as a new BH stabilization, while if they are NS to understand what happens their EoS is required.

NS-NS, NS-BH and BH-BH binaries have different characteristics. First of all, they emit GWs with different frequencies: the more massive are the merging objects, the shorter is the GWs frequency and the higher is the energy released ([36] and [44]). GWs from NS-NS binaries have a slower evolution and they can be measured from the inspiral, as Figure 1.4 shows. Moreover, BH-BH mergers have no EM counterpart because this is due to the tidal disruption of the objects (see [45]).

1.3 Gravitational Wave detection

1.3.1 GW interferometers

GW transit deforms spacetime. Particularly, it changes distances between free masses differently in the two orthogonal polarization directions; the relative deformation amplitude is $\Delta L/L << 10^{-18}$ ([36]) and can be measured thanks to interferometers.

Basically, interferometers work as showed in Figure 1.2, where the easiest configuration, due to Michelson and Morley, is represented. It is composed by a beam splitter
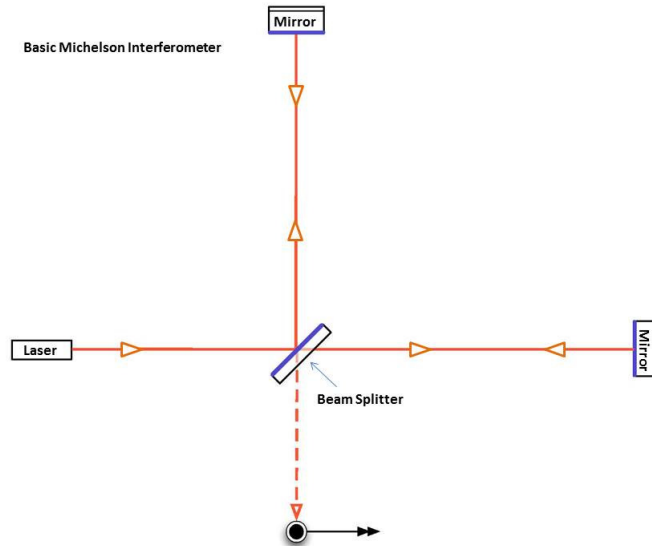

Figure 1.2: Michelson-Morley interferometer, described in Sec. 1.3.1. Image from [38].

which divides an impacting laser beam into two identical parts. One of them passes straight through while the other is deviated at 90°; each beam is then reflected by a mirror and comes back to the beam splitter. Here they merge again into a single beam, which is sent to a photodetector: it will measure the interference figure generated because the two beams travelled different paths before recombining. Any change in light intensity compared to the originally impacting laser can be used to calculate the lenght difference between the two arms travelled by light.

The already existing GW observatories, LIGO (Livingston and Hanford, USA [38]) and VIRGO (Cascina, Italy [69]) work similarly. They are made of two orthogonal arms 4 km long for LIGO and 3 km long for VIRGO (e.g. see Figure 1.3), in which the laser travels in vaccum condition ([36] and [38]). When a GW is passing, space itself is modified in the plane orthogonal to the propagation direction, being stretched in one direction and squeezed in the perpendicular one. Detector arms lenght can therefore change independentely one from another and this variation can change the interference pattern in the photodetector. Every part of these instruments has to be
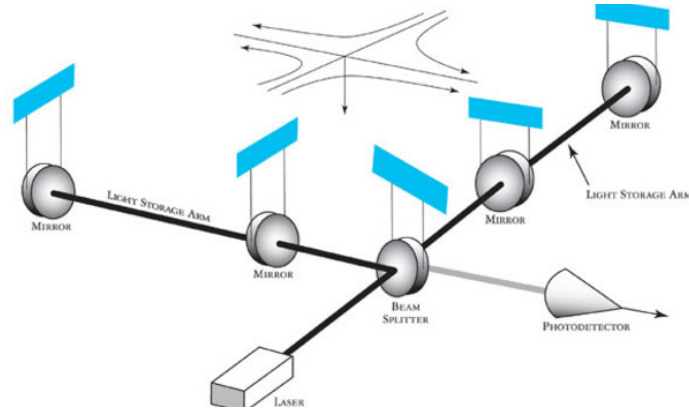

Figure 1.3: Basic schematic of LIGO's interferometers with an incoming GW arriving from above the detector. Image from [38].

isolated from the ground, otherwise its vibration would move the mirrors and change the interference pattern and cover the GW effects. To do so, active and passive damping systems are used: e.g. in LIGO interferometer (see [38]) the first ones are devices that sense ground vibrations and move mirrors in the opposite direction to eliminate their effect, while the second ones consist in inserting all the instruments in a reverse pendulum which absorbs any movement.

Other noise sources have to be taken into account (see [36] and [38]), e.g. thermal vibrations or quantum noise, magnetic or radio signals, glitches.

Each detector has its own power spectral density, describing its sensitivity at every frequency (see Figure 1.1); from Earth, the detectable range is $f \simeq$ Hz - kHz (see [36] and [61]). The signal the detector measures is

$$
\begin{aligned}
x(t) &= h(t) + n(t) \\
h(t) &= \begin{pmatrix} F_+ & F_\times \end{pmatrix} \begin{pmatrix} h_+ \\ h_\times \end{pmatrix} \\
n(t) &= \text{noise} .
\end{aligned}
\tag{1.58}
$$

The quantities F_+ and $F_\times$ are the detector response to the two polarizations h_+ and

$h_\times$. A GW is detected when the signal measured is above a certain threshold; from this, h_+ and $h_\times$ can be reconstructed.

It is important to use more than one detector for two main reasons. First of all because the noise sources acts in different ways in separate detectors, so the GW can be independently identify in each of them: the combination of different data sets improves the observation time, gives more detalis and can confirm or deny the detection itself ([36] and [55]). Moreover, a single detector can not locate the source of the GW, it only excludes some "blind" areas. To improve the angular resolution LIGO is made of two independent interferometers, one realized in Livingston and the second one in Hanford: they are built in order to measure the same polarization to improve the GW signal. A third inteferometer can therefore detect the missing polarization and locate the source thanks to triangularization processes. For this reason, LIGO and VIRGO data are analized together.

Up to now the LIGO-VIRGO collaboration has confirmed 5 BH-BH merger detections and 1 NS-NS, represented in Figure 1.4 (see [1], [2], [3], [4], [5], [6]).
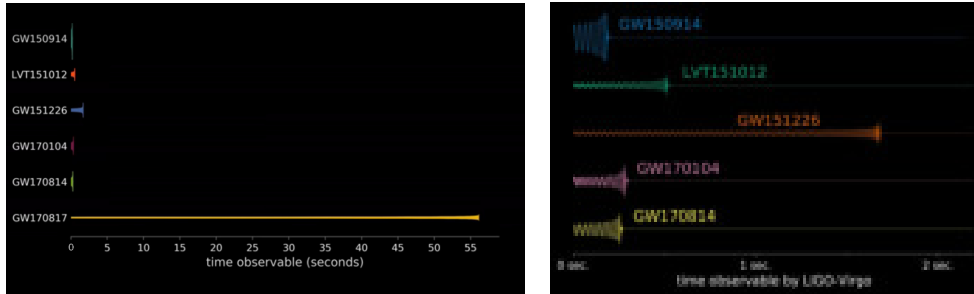

Figure 1.4: GW signals confirmed by the LIGO-VIRGO collaboration from 2016 until now. The left image shows all the signals: it can be noticed that NS-NS merger GW170817 signal is longer than BH-BH ones, over which the image on the right focuses. Images from [38].

Future detectors

In the years to come, GW Astronomy will become more and more relevant thanks to the improvement of instruments.

LIGO and VIRGO are currently being upgraded and they will be turned on again at the beginning of 2019. If also other interferometers will be built (e.g. LIGO India [39] or KAGRA [32]) there will be the possibility of detecting GWs between 10 and 1000 Hz [65] coming from all directions in the sky, analyzing them with a better signal-to-noise ratio (see Chapter 3).

In about 10 years, the so called 3rd generation interferometers will be realized: to extend the detectable amplitude range and increase the sensitivity at high f while decreasing the low f noise ([36] and [23]), they will be placed in underground observatories to lower the seismic impact and they will have cryogenically cooled mirrors to avoid thermal vibrations. Einstein Telescope (ET) is one of these. As described in [23] it will be made of three 10 km long arms arranged in a triangular pattern in order to be equally sensitive to both polarizations. Each of them will comprise two interferometers, one specialized for low frequency GWs and the other for high frequency ones; it will measure f up to 1 Hz [65].

Furthermore, space interferometers are planned for the 2030s. Isolated from every ambient noise and from the terrestrial gravity gradient, thanks to longer arms they will measure GWs with lower frequency ($f \simeq 10^{-4} - 10^{-1}$ Hz) [65], as the one produced during the merging of massive BH or the inspiraling of NS and BH whose merger can now be seen from Earth ([36] and [40]). Even the Cosmological GW background will become detectable thanks to in-orbit observatories. LISA (Laser Interferometer Space Antenna) will be the first one: it will be made of three spacecrafts in near-equilateral triangular formation (see [40] for details), with 2.5 million km long arms. The laser interferometry will compare the distance between free falling masses contained in each spacecraft; the plane in which the spacecrafts will lay will be inclined $\simeq 60°$ with respect to the ecliptic[10]. In this way, orbiting around the Sun the triangular formation will be maintained throughout the year, while the triangle will rotate about its centre [40] (see Figure 1.5). LISA will measure on frequencies different from the ones from the ground; in particular, it will allow to measure GWs from the Cosmological background (see Sec. 1.2.2 and e.g. [9] and [10]). Other possible future detectors will be BBO (Big Bang Observer) and DECIGO (DECI-herz Interferometer Gravitational wave Observatory). In the preconceptual design (see [19]) they constitute of 4 clusters, each of which is made by 3 spacecrafts exchanging laser beams one with the others (i.e. each of them is made as LISA). Two of these clusters will be located at the same position, in order to enhance the sensitivity; the other will be widely separated to increase the angular resolution. DECIGO and BBO will be the most sensitive to GWs in the $0.1 - 1$Hz band [19].

Figure 1.5 shows some characteristics that ET, LISA and BBO will have. All these projects will require the work of hundreds of people to be developed; this will push both the scientific and the technological development, involving a significant gain not only for the academic world, but for all the society.

1.3.2   GW signal

The GW detected signal is a waveform that can be modeled depending on its source. In the case of binary mergers, it depends on many parameters: the inspiralling bodies' masses and spins, the distance to the binary, its position in the sky and the orientation of its orbital plane. When comparing templates and observed waveforms, also the detector noise and its relative position and inclination related to the binary ones have to be taken into account [18].

The waveforms can be described with a Newtonian approximation or it can include also post-Newtonian corrections. In fact, to the lowest order, inspiralling compact binaries can be described as two orbiting Newtonian point particles, whose motion evolves secularly due to GW emissions. When they impact the detector, they produce (see [18] for details) the measured strain

$$h(t) = \frac{(384/5)^{1/2}\pi^{2/3}Q(\theta,\phi,\psi,\iota)\mu M}{Dr(t)} \cos\left(\int 2\pi f dt\right) , \qquad (1.59)$$

where D is the distance to the source, while the angles describe the sky position and the orientation of the binary: (θ,ϕ) is the spherical coordinate system centered at the Earth, so that $\theta = 0$ is the Earth's rotation axis and $\pi/2 - \theta$ is the North latitude, while ϕ is the longitude; the unit vector $\mathbf{n} = (\sin\theta\cos\phi, \sin\theta\sin\phi, \cos\theta)$ is defined.

---

[10]The ecliptic is the apparent path over which the Sun moves when seen from the Earth reference system. It is given by the intersection between the terrestrial orbital plane and the celestial sphere.
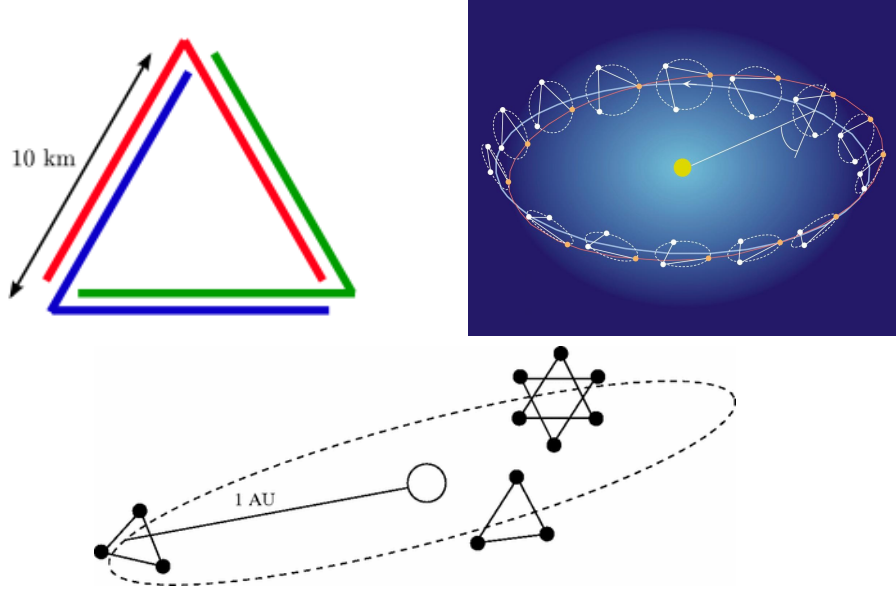
Figure 1.5: Above images: to the left ET laser arrangement; to the right LISA configuration and orbit. Below image: BBO configuration. Images respectevely from [23], [40], [19].

ψ is the polarization angle and ι is the inclination of the orbit to the Line Of Sight (LOS), such that $\cos\iota = \hat{\mathbf{L}} \cdot \mathbf{n}$ being $\hat{\mathbf{L}}$ the unit vector in the direction of the binary's orbital angular momentum. The function $r(t)$ is obtained integrating the final rates for circula orbits: as [18] shows,

$$\frac{dr}{dt} = \frac{dr}{dE}\frac{dE}{dt} = -\frac{r}{E}\frac{dE}{dt} = -\frac{64}{5}\frac{\mu M^2}{r^3} \ , \tag{1.60}$$

where dr/dE is the decreasing of the orbit size due to the energy loss when GWs are emitted. Integrating eq. (1.60), one obtains $r(t) = (256/5 \cdot \mu M^2)^{1/4}(t_c - t)^{1/4}$.

Finally, the functions the quantity Q depends from are discussed. Consider a network of detectors, each of which having output $h_a(t) = \mathbf{d}_a : \mathbf{h}(\mathbf{x}_a, t)$. $\mathbf{d}_a$ is the polarization tensor of the ath detector, which double contracts[11] with the TT strain tensor $\mathbf{h}(\mathbf{x}, t)$. As described in Sec. 1.1.2, $\mathbf{x}_a$ can be omitted while studying the wave at the detector location. Let $\mathbf{e}_n^A$ with $A = +, \times$ be a basis for the TT tensor perpendicular to $\mathbf{n}$; the detector beam pattern functions can therefore be defined as

$$F_a^A(\mathbf{n}) = \mathbf{e}_n^A : \mathbf{d}_a \ . \tag{1.61}$$

The basis $(\mathbf{e}_n^+, \mathbf{e}_n^\times)$ can be transformed into any other polarization basis $(\mathbf{e}'^+, \mathbf{e}'^\times)$ thanks to the rotation $\mathbf{e}'^A = R_B^A(2\psi)\mathbf{e}_n^B$ where the rotation matrix is defined as

$$R_B^A(2\psi) \ = \ \begin{pmatrix} \cos 2\psi & \sin 2\psi \\ -\sin 2\psi & \cos 2\psi \end{pmatrix} \ . \tag{1.62}$$

The strain tensor $\mathbf{h}(t)$ of the wave can be separated in $h_+(t)\mathbf{e}'_x + h_\times(t)\mathbf{e}'_y$ calculated

---

[11]For tensors A_{ij} and B_{lm} the ":" product is defined as $A : B = \text{tr}(AB^T) = A_{ij}B_{ij}$.

in the preferred polarization basis $(\mathbf{e}'_x, \mathbf{e}'_y)$, where

$$
\begin{aligned}
\mathbf{e}'_x &= \frac{\mathbf{n} \times \hat{\mathbf{L}}}{||\mathbf{n} \times \hat{\mathbf{L}}||} \\
\mathbf{e}'_y &= \frac{-\mathbf{n} \times \mathbf{e}'_x}{||\mathbf{n} \times \mathbf{e}'_\mathbf{x}||} \ .
\end{aligned}
\tag{1.63}
$$

The Fourier transform of the two polarization components is

$$
\tilde{h}_A(f) = \chi_A(\cos\iota)\tilde{h}_0(f)
\tag{1.64}
$$

where $\chi_+ = (1 + \cos 2\iota)/2$, $\chi_\times = -i\cos\iota$ and

$$
\tilde{h}_0(f) = \sqrt{\frac{5}{24}}\pi^{-2/3}D^{-1}M_{\text{chirp}}^{5/6}f^{-7/6}\exp[i\Psi(f)] \quad \text{for } f \geqslant 0 \ ,
\tag{1.65}
$$

where $\Psi(f)$ is a function of M_{chirp}, μ, the spin parameter β, the time and waveform phase at the coalescence t_C and ϕ_C (see [18] for details); the signal amplitude and frequency both increases as $t \to t_C$. Finally, $Q \propto R_B^A(2\psi)\chi_A(\cos\iota)F_a^B(\mathbf{n})$ and the signal defined in eq. (1.59), when it is read by a single detector, becomes (see [18] for details)

$$
\tilde{h}(f) = R_B^A(2\psi)\chi_A(\cos\iota)F_a^B(\mathbf{n})e^{-2\pi i(\mathbf{n}\cdot\mathbf{x})f}\ \tilde{h}_0(f) \ .
\tag{1.66}
$$

In [18] the Fourier transform of the Newtonian waveform is explicitly computed; its final expression is

$$
\tilde{h}(f) = \frac{Q}{D}\ M_{\text{chirp}}^{5/6}\ f^{-7/6}\ \exp[i\Psi(f)] \ ,
\tag{1.67}
$$

valid up to high frequencies, where the model transits to the ring down phase (see Sec. 1.2.2).

If the detector and the binary are in relative motion, the detected signal $\mathbf{h}(t)$ is Doppler-shifted and it is not possible to reconstruct the no-shifted signal from it, because of the $\mathbf{h}(t)$ invariance under the transformation $(f, M_{\text{chirp}}, \mu, R, D, t) \to (f/\lambda, M_{\text{chirp}}\lambda, \mu\lambda, R\lambda, D\lambda, t\lambda)$ being λ the shift amplitude. For binary systems at Cosmological distances, GWs parameters depend on the Cosmological redshift z (see Chapter 2); in particular, the waveform is function of

$$
M_z = (1 + z)M_{\text{chirp}} \quad \mu_z = (1 + z)\mu \ ,
\tag{1.68}
$$

and of the luminosity distance D_L (see Chapter 2) instead of D.

It is possible to extend this model including post-Newtonian effects, indicated as $P^x N$, where x is the order of the correction. The binary can still be considered as formed by two point-like masses since tidal intetractions are negligible [18]; nevertheless they can have spin angular momenta. Corrections of the $P^x N$ order implies that the GW waveform includes higher order multipoles of the energy-momentum tensor and corrections for the lowest-order expression for the amplitude of each multipole component. This implies corrections in the energy and gravitational luminosity with a consequent modification in the inspiral rate and in the orbital phase (see [18] for details).

In [51] the following expression for the post-Newtonian waveform for a NS-NS system is reported:

$$
\tilde{h}(f) = \frac{A}{D_L(z)}M_z^{5/6}f^{-7/6}e^{i\Phi(f)} \ ,
\tag{1.69}
$$

where

$$A = (\sqrt{6}\pi^{2/3})^{-1} \quad \text{is a geometrical factor due to the binary inclinations average}$$

$$\Phi = 2\pi f t_c - \phi_c - \frac{\pi}{4} + \frac{3}{128}(\pi M_z f)^{-5/3}\left[1 + \frac{20}{9}\left(\frac{743}{336} + \frac{11}{4}\eta\right)\eta^{-2/5}(\pi M_z f)^{2/3} - \right.$$
$$\left. - 16\pi\eta^{-3/5}(\pi M_z f) - \frac{25}{768}X(z)M_z(\pi M_z f)^{-8/3}\right] .$$
(1.70)

In the previous expression

- $\eta = \frac{m_1 m_2}{(m_1+m_2)^2}$ is the symmetric mass ratio;

- $D_L(z) = (1+z)\int_0^z \frac{1}{H(z')}\,dz'$ is the luminosity distance (see Chapter 2);

- $X(z) = \frac{1}{2}\left(H_0 - \frac{H(z)}{1+z}\right)$ is the Universe expansion parameter, being $X(z) > 0$ when the expansion is accelerated, $X(z) < 0$ when it is decelerated. $H(z)$ is the Hubble parameter at the binary distance and H_0 is its current value.

Φ is function of $\pi M_z f$, so it is redshift dependent. It is made of different contributions:

- $2\pi f t_c - \phi_c - \frac{\pi}{4}$ is the intrinsic part, due to the GW formation;

- $\frac{3}{128}(\pi M_z f)^{-5/3}$ is due to the Newtonian dynamics;

- $\frac{3}{128}(\pi M_z f)^{-5/3}\left[\frac{20}{9}\left(\frac{743}{336} + \frac{11}{4}\eta\right)\eta^{-2/5}(\pi M_z f)^{2/3}\left(-16\pi\eta^{-3/5}(\pi M_z f)\right)\right]$ is the PN correction;

- $\frac{3}{128}(\pi M_z f)^{-5/3}\left[-\frac{25}{768}X(z)M_z(\pi M_z f)^{-8/3}\right]$ is the P^4N phase correction due to the Universe expansion and it is relevant at low frequencies.

This is the waveform expression that will be used from now on in this work.

Chapter 2

Can Cosmology exploit Gravitational Waves?

This Chapter describes how Gravitational Waves can be used to infer informations on the structure and the evolution of the Universe. To do so, some elements of the Cosmological Standard Model (Sec. 2.1) of the teory of distribution and evolution of Universe Large Scale Structures (LSS) (Sec. 2.2) are given. These will be useful to understand what can be done with GWs (Sec. 2.3).

2.1 Cosmological Standard Model overview

2.1.1 Living in an expanding Universe

Today's Cosmology is based on the so called Cosmological Principle: on sufficiently large scales (over 100 Mpc [11] and [37]), the Universe can be considered homogeneous and isotropic [17]. Homogeneity means that the fluctuations due to the presence of cosmic structures "looks the same", on average, in different positions in space (e.g. the smoothed matter density field takes the same value everywhere). Isotropy on the other hand is the property of looking the same on average in every direction; this is quite evident looking at the Cosmic Microwave Background radiation (CMB)[1].

To describe this background configuration (over which a perturbative theory will describe the existence of structures, see Sec. 2.2), GR can be used. The Universe on the largest scales can be treated (see [17] for details) as a perfect fluid, the geometrical properties of which at the 0th order are described by a metric (see Sec. 1.1) underlying the Cosmological Principle. This is the Robertson Walker (RW) metric, described by

$$ds^2 = -dt^2 + a^2(t)\left[\frac{dr^2}{1 - kr^2} + r^2(d\theta^2 + \sin^2\theta d\phi^2)\right] , \tag{2.1}$$

where (r, θ, ϕ) are the comoving spherical coordinates and k is the spatial curvature parameter, being $k = 0$ in flat spaces, $k > 0$ (always re-scalable to $k = +1$ via a

---

[1]The CMB is the radiation emitted on the last scattering surface, when for the first time photons decoupled from matter. Before that moment, the high density prevents the photons free streaming because of the high cross section and the small free path they had; the Universe expansion (see Sec. 2.1.1) changed that quantities until the Universe became transparent to radiation. Today the CMB can be measured in the microwave band ($\simeq$ GHz): it has a quasi-perfect Black Body (BB) spectrum, whose temperature is 2.725 K [35] with very little fluctuations one direction from another.

rescaling of a(t)) in closed spaces or $k < 0$ (always re-scalable to $k = -1$) in open ones. $a(t)$ is the scale factor: it describes how the Universe size evolves in time, expanding if $a(t) > 0$, contracting if $a(t) < 0$ or mantaining the same size it has today if $a(t) = a(t_0) = 1$.

$a(t)$ is linked to the physical distance: in fact, while the comoving coordinates (r, θ, ϕ) and the comoving distances χ remain constant through time, the space expansion implies that proper distances between points change ([11] and [37]) as

$$d(t) = a(t)\chi$$

$$\text{where } \chi = \begin{cases} |k|^{-1/2} \sinh^{-1} \sqrt{|k|}r & \text{if } k < 0 \\ r & \text{if } k = 0 \\ |k|^{-1/2} \sin^{-1} \sqrt{|k|}r & \text{if } k > 0 . \end{cases} \tag{2.2}$$

The scale factor evolution can be inferred from the Einstein equations (see Chapter 1): for a homogeneous and isotropic perfect fluid described by rest-mass energy density $\rho = \rho c^2$ and pressure p, the solutions are (see [17]) the Friedmann Cosmological equations

$$\begin{cases} \dot{a}^2 + k = \frac{8}{3}\pi G \rho a^2 \\ \ddot{a} = -\frac{4}{3}\pi G(\rho + 3p)a . \end{cases} \tag{2.3}$$

From eq. (2.3) $a(t)$ can be obtained when the EoS is known: set $\omega = p/\rho$ and chosen $k = 0$ (flat Universe or sub-dominant curvature ([11] and [37])), the scale factor is

$$a(t) = t^{2/3(1+\omega)} \Rightarrow \rho \propto a^{-3(1+\omega)} , \tag{2.4}$$

The value of ω depends on what the Universe is dominated by: if the main component is radiation it is $\omega = 1/3$, if the Universe is matter-dominated $\omega = 0$, if Dark Energy (DE) dominates then $\omega = -1$. The relative aboundance of these components can be determined comparing their density $\rho_\gamma, \rho_m, \rho_\Lambda$ or their density parameters $\Omega_{\gamma,m,\Lambda} = \rho_{\gamma,m,\Lambda}/\rho_c$; ρ_c is the critical density, whose value correspond to the one required to have a flat Universe. Solving eq. (2.3), it can be demonstrated [17] that

$$\rho_c = \frac{3}{8\pi}\left(\frac{\dot{a}}{a}\right)^2 . \tag{2.5}$$

The total matter-energy density is $\Omega_{TOT} = \Omega_\gamma + \Omega_m + \Omega_\Lambda$; today $\Omega_{TOT} \simeq \Omega_m + \Omega_\Lambda$ because Ω_γ is negligible.

Observations today give good evidence that the Universe is flat and expanding in an accelerated manner (see [35] and [56]); some of its characterizing parameters are reported in Tab. 2.1. This is consistent with a Universe dominated by a Cosmological constant, or a dynamical DE component, as eq. (2.4) can show if it is calculated for each one of the Universe components in order to get the evolution trend of the density parameters. Alternatively, this accelerated expansion can be explained with a modification of Einstein equations on the largest Cosmological scales.

Whatever observer is chosen, it can picture the same Universe thanks to the Cosmological Principle; in particular, it sees the other points in space moving away as time goes by, because of the expansion. The farther a point is, the faster it would recede from the observer; this can be expressed by means of the Hubble law (see [17])

$$v = \frac{\dot{a}(t)}{a(t)}\chi = H(t)\chi \Rightarrow H(t) = \frac{\dot{a}(t)}{a(t)} . \tag{2.6}$$

	WMAP	PLANCK
$\Omega_b h^2$	0.02225 ± 0.054	0.02242 ± 0.00014
$\Omega_{DM} h^2$	0.1126 ± 0.0036	0.11933 ± 0.00091
Ω_Λ	0.725 ± 0.016	0.6889 ± 0.0056
n_s	0.968 ± 0.012	0.9665 ± 0.0038
H_0	70.2 ± 1.4 km s^{-1} Mpc^{-1}	67.66 ± 0.42 km s^{-1} Mpc^{-1}

Table 2.1: Universe parameters derived from the WMAP survey [35] and the PLANCK satellite [56]. Ω_b is the baryon density parameter and Ω_{DM} the Dark Matter one. They can be combined to get $\Omega_m = \Omega_b + \Omega_{DM}$. Ω_Λ, H_0 and h^2 are defined in Sec. 2.1.1, while n_s in Sec. 2.2.2.

The quantity $H(t)$ is called the Hubble parameter; its current value H_0 is commonly called Hubble constant and is reported in Tab. 2.1. Other parameters are frequently used: $h = H_0/(100$ km s^{-1}Mpc$^{-1})$ and $h_{70} = H_0/(70$ km s^{-1}Mpc$^{-1})$ reduce the Hubble constant to an adimensional quantity while H_0/c expresses it in Mpc^{-1}.

Redshift and distance measurements

When a luminous source is considered (e.g. a galaxy), it is possible to define [17] its redshift z as

$$z = \frac{\lambda_0 - \lambda_e}{\lambda_e} , \qquad (2.7)$$

where λ_0 is the wavelength observed for its radiation at $t = t_0$, while λ_e is the one the source emitted at $t = t_e$; the difference between the two is due to the Doppler effect caused by the relative motion between the source and the observer and can be measured from the emission/absorption lines on the EM spectrum. As [17] demonstrates, it is linked with the scale factor by the relation

$$1 + z = \frac{1}{a} \quad \text{with} \quad a = a(t_e) \text{ and } 1 = a(t_0) . \qquad (2.8)$$

Visible objects extend out to $z \lesssim 6$ [22].

It is possible to demonstrate that, when the Universe is flat[2],

$$H(z) = H_0 \sqrt{\Omega_m(1+z)^3 + \Omega_{gamma}(1+z)^4 + \Omega_\Lambda} . \qquad (2.9)$$

When spacetime is expanding, the distance between the source and the observer is not uniquely defined. Considering that the observer is located where the scale factor is $a(t_0) = 1$, the source comoving distance can be calculated [22] as

$$\begin{aligned} \chi = D_c &= \int_{t(a)}^{t_0} \frac{dt'}{a(t')} \\ &= \int_a^1 \frac{da'}{a'\dot{a}'} \quad \text{changing the integration variable from } t' \text{ to } a' \\ &= \int_a^1 \frac{da'}{a'^2 H(a')} \quad \text{using eq. (2.6)} \\ &= \int_0^z \frac{dz'}{\sqrt{\Omega_m(1+z')^3 + \Omega_\Lambda}} dz' \quad \text{using eq. (2.8) and (2.9)} , \end{aligned} \qquad (2.10)$$

---

[2]From now on, we will assume a flat Universe, consistently with current observational evidence from CMB data.

and consequently

$$\chi = \frac{1}{H_0} \int_0^z \frac{H_0}{H(z')} \, dz' \ .$$
(2.11)

Another way is to define the luminosity distance D_L: this is linked with the preservation of the Euclidean inverse-square law for the diminution of light

$$F = \frac{L}{4\pi D_L^2} \ ,$$
(2.12)

where L denotes the power emitted at time t by one source and F its flux, i.e. the power received per unit area. If it is located at comoving distance D_c and $L(D_c)$ is the power passing through a spherical shell $4\pi D_c^2$, the flux at time t_0 is

$$F = \frac{L(D_c)}{4\pi D_c^2} \ .$$
(2.13)

The value of $L(D_c)$ depends on the number and the energy of the photons detected in a fixed time. The photon number is smaller by a factor a at the observer location than it was at emission because of the expansion of the Universe; similarly, the energy decreases by a factor a between the two points (see [22] for details). Therefore, the observed luminosity is smaller by a factor a^2 than L and eq. (2.13) can be rewritten as

$$F = \frac{La^2}{4\pi D_c^2} \ .$$
(2.14)

Eq. (2.12) and (2.14) express the same relation: this implies that the luminosity distance is

$$D_L = \frac{D_c}{a} = (1+z) \int_0^z \frac{1}{H(z')} \, dz' \ .$$
(2.15)

The third distance definition is linked with the apparent angular size θ of an extended source. If its physical size is d, the comoving one is d/a (see eq. (2.2)) and the subtended angle appears to be $\theta = (d/a)/D_c$ (see [22] for details); consequently it is possible to define the angular diameter distance as

$$\begin{aligned}
D_A &= d/\theta = aD_c \\
&= \frac{D_c}{1+z} = \frac{D_L}{(1+z)^2} \ .
\end{aligned}$$
(2.16)

Standard candles

The luminosity distance to a source, when measurable, can be compared to the redshift to infer the expansion rate of the Universe. To do so, sources of known intrinsic luminosity have to be taken into account: the most representative are type Ia SN. These are different from the SN described in Sec. 1.2. In fact, they are not due to massive stars evolution but to the thermonuclear explosion of a Carbon Oxygen White Dwarf (WD), the remnant of a small star core (see [46] and [59] for details). This happens in binary systems: the mass accretion from the companion to the WD brings it to reach the Chandrasekhar limit[3], triggering the Carbon ignition. In WD conditions, this process is unstable and leads to a strong increase in temperature: in

---

[3]The Chandrasekhar mass $M_{Ch} = 1.46M_\odot$ is defined for a system held by degenerate electron pressure, e.g. a WD: when this mass value is overcome, electrons can no longer support the hydrostatic equilibrium condition that prevents the system from collapsing under its own gravity.

this way, all the WD material is burned thanks to an explosive flame that propagates outwards (see [46] and [59] for details).

Type Ia SN have no remnants and their light curve is very well modeled. In particular, their peaks are very bright and have a very small spread in intrinsic luminosity, probably due to the fact that WD explosions all happen more or less at the same mass value, set by the Chandrasekhar limit (see [34]). These properties bring two important consequences: first of all, the apparent brightness can be used to infer SN luminosity distance D_L as described in eq. (2.12); furthermore, these objects can be seen even if they are very far in space, where the Cosmological effects are large enough to be measured [34]. Particularly, the D_L can be compared to the redshift z thanks to the Hubble diagram reported in Figure 2.1: from eq. (2.15) and (2.6) it can be seen how the relation between them depends on the value (and the sign) of $\dot{a}$, thus from the fact that the Universe is expanding accelerating, decelerating or with costant rate. Similarly it can be done using GWs, as Sec. 2.3.2 describes.
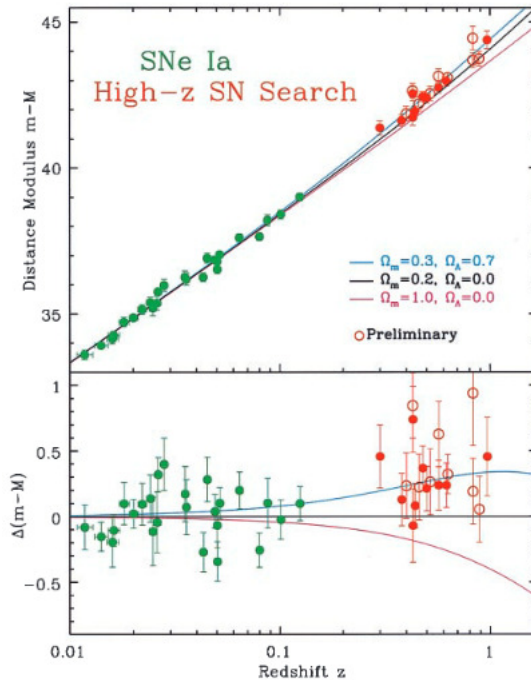
Figure 2.1: The Hubble diagram for SN Ia. The lines show the predictions for various Cosmologies, the points are observations: they show that a model with $\Lambda > 0$ (i.e. an accelerated expanding Universe) is favoured. Image from [34].

2.2   Cosmological Perturbation

2.2.1   RW perturbation

The RW metric describes the Universe on large scales (see Sec. 2.1); to study how structures (i.e. DM halos, galaxies, stars...) were born and evolve it is instead necessary to to study small fluctuations with respect to the RW background, representing small matter inhomogeneities. This leads to developing a perturbative theory.

Primordial quantum fluctuactions from Inflation can generate such small amplitude initial density inhomogeneities that evolve in time, generating the LSS that can be seen today. This is based on the effect of gravitational instability [22] that brings matter to accumulate in the initially overdense regions, against which pressure exerted by the particle thermal motions acts, trying to preserve the pre-existing hydrostatic equilibrium. To model this situation, two regimes have to be taken into account ([11] and [37]):

- the linear regime, on scales over $\lambda \simeq 10$ Mpc where the perturbations are $\delta = \delta\rho/\bar{\rho} \simeq 10^{-5}$, $\bar{\rho}$ being the RW background mean density;

- the non linear regime, on scales $\lambda < 10$ Mpc, i.e. where the galaxies formation takes place.

In both cases, it is possible to perturb both the metric and the energy-momentum tensor. The background metric can be expressed as $ds^2 = g_{\mu\nu}dx^\mu dx^\nu = a^2(\eta)(-d\eta^2 + dx^2 + dy^2 + dz^2)$, $d\eta = dt/a$ being the conformal time; each component can be perturbed as follows (see [11] and [37] for details)

$$
\begin{aligned}
g_{00} &= -a^2(\eta)\left(1 + 2\sum_{r=1}^{\infty}\frac{1}{r!}\psi^{(r)}\right) \\
g_{0i} &= g_{i0} = -a^2(\eta)\sum_{r=1}^{\infty}\frac{1}{r!}\omega_i^{(r)} \\
g_{ij} &= a^2(\eta)\left[\left(1 - 2\sum_{r=1}^{\infty}\frac{1}{r!}\phi^{(r)}\right)\delta_{Dij} + \sum_{r=1}^{\infty}\chi_{ij}^{(r)}\right].
\end{aligned}
\tag{2.17}
$$

where $r = 1, 2...$ is the perturbative order; $\psi^{(r)}(\mathbf{x}, \eta)$, $\omega_i^{(r)}(\mathbf{x}, \eta)$, $\phi^{(r)}$ and $\chi_{ij}^{(r)}$ can be parted into scalar, vectorial and tensorial components that are independent[4] one from another at the 1$^{\text{st}}$ order. In particular

- $\psi^{(r)}$ and $\phi^{(r)}$ are scalar quantities;

- $\omega_i^{(r)} = \partial_i\omega_\parallel^{(r)} + \omega_{i\perp}^{(r)}$ where $\partial_i\omega_\parallel^{(r)}$ is the gradient of the scalar potential and $\omega_{i\perp}^{(r)}$ is the vectorial part, with null divergence $\partial^i\omega_{i\perp}^{(r)} = 0$;

- $\chi_{ij} = D_{ij}\chi_\parallel^{(r)} + \partial_i\chi_{j\perp}^{(r)} + \partial_j\chi_{i\perp}^{(r)} + \chi_{ijT}^{(r)}$ is a traceless tensor with null divergence, where $D_{ij}\chi_\parallel^{(r)} = (\partial_i\partial_j - 1/3\nabla^2\delta_{ij})\chi_\parallel^{(r)}$, $\partial_i\chi_{i\perp}^{(r)} = 0$ and $\chi_{iT}^i = 0$, $\partial^i\chi_{iT} = 0$.

The scalar component is linked with density fluctuations, the tensor one gives rise to stochastic GWs (different from the Astrophysical GWs described in Sec. 1.2, see e.g. [14]), while the vector component can be neglected because its amplitude decreases rapidly in time. In this work only scalar perturbations are considered: they are linked with $\psi^{(r)}$, $\phi^{(r)}$, $\omega_\parallel^{(r)}$ and $\chi_\parallel^{(r)}$.

It is possible also to perturb the energy-tensor momentum (see Sec. 1.1) $T_{\mu\nu} = \rho u_\mu u_\nu + p(g_{\mu\nu} + u_\mu u_\nu) + \Pi_{\mu\nu}$ (where $\Pi_{\mu\nu}$ is due to the anisotropic stress) modifying

---

[4]This means that a scalar perturbation can not give rise to vector or tensor ones, as well as a vectorial or a tensorial perturbation can't give rise to the others.

the density or the 4-velocity as

$$\rho = \rho_0 + \sum_{r=1}^{\infty} \frac{1}{r!} \delta^{(r)}\rho$$

$$u^\mu = \frac{1}{a}\left(\delta_0^\mu + \sum_{r=1}^{\infty} \frac{1}{r!} v^{(r)\mu}\right) \tag{2.18}$$

where $\dfrac{1}{a}\delta_0^\mu = \dfrac{\delta_0^\mu}{\sqrt{-g_{00}}} = u^\mu$ is the velocity comoving with the expansion.

Using the EoS, the pressure perturbation can be defined as

$$\delta p = \left.\frac{\partial p}{\partial \rho}\right|_S + \left.\frac{\partial p}{\partial S}\right|_\rho = c_s^2 \delta\rho + \delta p_{na} \tag{2.19}$$

where $c_s^2 = \left.\dfrac{\partial p}{\partial \rho}\right|_S$ is the adiabatic speed of sound.

It is possible to demonstrate that the value of the perturbations has 2 degrees of freedom due to the gauge choice (see Sec. 1.1.2). Some gauge invariants can therefore be defined (see [11] and [37] for details): in the scalar case 2 independent quantities can be defined, both acting on the geometry (i.e. using the metric fluctuations) or on the matter perturbations (i.e. acting on $T_{\mu\nu}$). In the first case, the two Bardeen gauge invariant gravitational potentials can be defined ([11] and [37]) as

$$2\Psi_A = 2\psi + 2\omega_\parallel' + \frac{2a'}{a}\omega_\parallel - \left(\chi_\parallel'' + \frac{a'}{a}\chi_\parallel'\right)$$

$$2\Phi_H = -2\phi - \frac{1}{3}\nabla^2\chi_\parallel + \frac{2a'}{a}\omega_\parallel - \frac{a'}{a}\chi_\parallel' \ . \tag{2.20}$$

When the Poisson gauge[5] is chosen $\Psi_A = \psi$ and $\Phi_H = -\phi$

These perturbation are due to the primordial quantum fluctuactions (see [11] and [37] for details) that were imprinted as classical perturbations on Cosmological scales, at the end of Inflation. Their evolution is obtained inserting eq. (2.17), (2.18) and (2.19) into eq. (1.9) (for a complete derivation, see [22]). When the perturbations have scale larger than the horizon[6], they are frozen; large perturbations that can be seen today entered the horizon recently and their evolution is still linear. The smaller ones entered the horizon before and their evolution is linked with the epoch at which they did it: δ grows logarithmically in the radiation dominated era, while it is described by a time power law in the matter dominated one [22]. Despite this, at late times the evolution of different size perturbations becomes identical; the matter distribution at this stage can be observed and linked with the primordial one.

---

[5]The Poisson gauge is defined by $\omega_\parallel = 0$, $\chi_\parallel = 0$ and $\chi_\perp^i = 0$. It is the one in which the Einstein equations (see Sec. 1.1) are directly reducible to the Newtonian form.

[6]The Cosmological horizon is defined as $R_c = c/H(t)$. It contains the regions that are in causal contact with the observer, i.e. the regions from which an emitted light ray can reach the observer in a time $t < \tau_H = 1/H(t)$ ([11] and [37]).

Perturbation evolution

Cosmological perturbations can be seen as a superposition of plane waves evolving independently while the fluctuations are still linear [17]. They are described by the wave vector $\mathbf{k}$ and they are linked via a Poisson equation to the gravitational potential $\Phi(\mathbf{k})$. It set its value during Inflation and in turns it generates matter fluctuations δ.

The distribution of the Cosmological perturbations can be therefore represented not in real space, but in Fourier space, in terms of the wavevectors of each component $\mathbf{k}$. The Universe can be considered as a volume V, for example a cube of side $L >> l_s$ where l_s is the maximum scale for the perturbations; let $\bar{\rho}$ be the main density inside V and $\rho(\mathbf{x})$ the density at a point specified by the position vector $\mathbf{x}$: the fluctuation here is $\delta(\mathbf{x}) = [\rho(\mathbf{x}) - \bar{\rho}]/\bar{\rho}$. This can be expressed as a Fourier series

$$\delta(\mathbf{x}) = \sum_k \delta_k \exp(i\mathbf{k} \cdot \mathbf{x}) = \sum_k \delta_k^* \exp(-i\mathbf{k} \cdot \mathbf{x}) \ , \tag{2.21}$$

where the wavevector $\mathbf{k}$ has components

$$k_x = n_x \frac{2\pi}{L} \quad k_y = n_y \frac{2\pi}{L} \quad k_z = n_z \frac{2\pi}{L} \qquad \text{with } n_x, \ n_y, \ n_z \text{ scalars,} \tag{2.22}$$

and the Fourier coefficients are [17]

$$\delta_{\mathbf{k}} = \frac{1}{V} \int_V \delta(\mathbf{x}) \exp(-i\mathbf{k} \cdot \mathbf{x}) \, d\mathbf{x} \quad \text{and } \delta_{\mathbf{k}}^* = \delta_{-\mathbf{k}} \text{ because } \delta(\mathbf{k}) \in \mathbb{R}. \tag{2.23}$$

In [22], the full derivation of both the Power Spectrum (PS, see Sec. 2.2.2) of $\Phi(\mathbf{k})$ and of the perturbations $\delta_{\mathbf{k}}$ is shown. The primordial fluctuations distribution can be related to the matter distribution observable today Φ_0 (see [22]) thanks to the relation (see Sec. 2.2.2 for the $\mathbf{k}$ and k dependence)

$$\Phi_0(\mathbf{k}, a) = \Phi(\mathbf{k})T(k)G(a) \ . \tag{2.24}$$

The function $T(k)$ is the Transfer function, describing the evolution of perturbations through the epoch of horizon crossing and the transition between the radiation and the matter dominated era; it is conventionally defined in order to get $T(k) = 1$ on Large Scales [22] as

$$T(k) = \frac{\Phi(k, a_{\text{Late}})}{\Phi_{\text{Large Scales}}(k, a_{\text{Late}})} \ , \tag{2.25}$$

where a_{Late} is the scale factor at a time well after the perturbation entered the horizon and the transition between radiation and matter dominated era happened. $G(a)$ is the Growth function that describes the wavelenght independent growth at late times; conventionally

$$\frac{G(a)}{a} = \frac{\Phi(a)}{\Phi(a_{\text{Late}})} \ . \tag{2.26}$$

To explicitly link the fluctuations in the gravitational potential to the perturbations in the matter distribution, the Poisson equation can be used [22]

$$\begin{aligned} \Phi_0(\mathbf{k}, a) &= \frac{4\pi \rho_m a^2 \delta}{k^2} \quad \text{if } a > a_{\text{late}} \\ \Rightarrow \delta(\mathbf{k}, a) &= \frac{k^2 a \ \Phi_0(\mathbf{k}, a)}{(3/2) \ \Omega_m H_0^2} = \frac{3}{5} \frac{k^2}{\Omega_m H_0^2} \ \Phi(\mathbf{k})T(k)G(a) \ , \end{aligned} \tag{2.27}$$

where the second equation is obtained substituting $\rho_m = \Omega_m \rho_c / a^3$ and using the Friedmann equation (2.3) to get $4\pi\rho_c = (3/2)H_0^2$ while the third uses eq. (2.24), (2.25) and (2.26) with the convention previously described (see [22] for details). The PS derived for the density distribution is reported in Sec. 2.2.2. The author of [22] presents the complete description of the evolution of its modes k; we show here only the final result, which will be useful later on.

Particularly, at late times ($z \lesssim 10$) all the k modes have entered the horizon and experience the same growth function. This uniform evolution is due to the fact that Cold[7] DM has zero pressure and has no way to smooth out inhomogenities. It can be shown that in this case the growth function can be computed analitically; its trend is reported in Figure 2.2 and it is derived from

$$G(a) = \frac{5\Omega_m}{2} \frac{H(a)}{H_0} \int_0^a \frac{da'}{\left[a' \frac{H(a')}{H_0} \right]^3} \ . \tag{2.28}$$

Considering $a = 1/(1+z)$ eq. (2.28) can be also expressed by

$$G(z) = \frac{5\Omega_m}{2} \frac{H(z)}{H_0} \int_z^\infty \frac{(1+z')H_0^3}{H(z')^3} \, dx' \ . \tag{2.29}$$
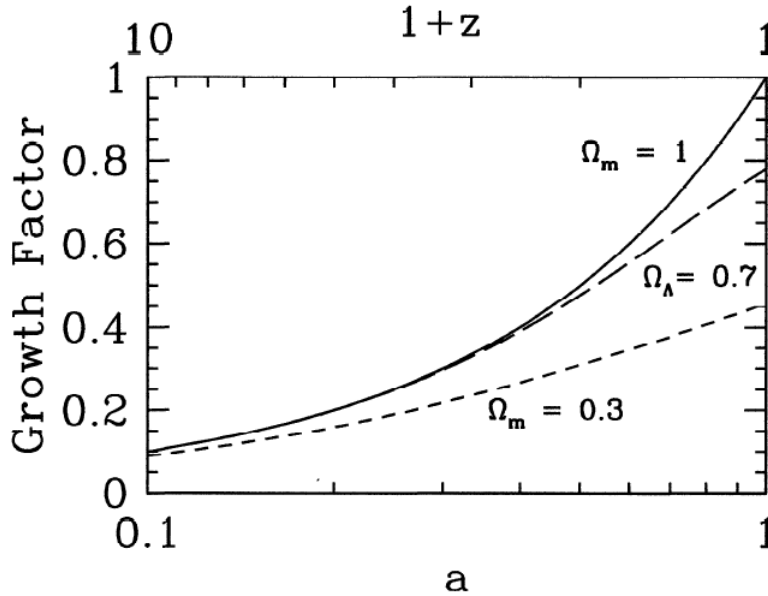
Figure 2.2: Growth function depending on the Cosmology choice. The two upper curves are for flat Universes respectively with and without Λ contribution; the bottom curve is for an open Universe. Image from [22].

---

[7]In the composition of the Universe, Ω_m main contribution is given by DM. This can be divided into Hot (HDM), Warm (WDM) and Cold (CDM) depending on the velocity its particles had at the moment they decoupled from radiation. Observations show that CDM is the most aboundant and the one forming the halos from which structures generated.

2.2.2   Power Spectrum

Considering the Fourier representation of the Cosmological perturbations described in Sec. 2.2.1, it is possible to consider a large number N of 'realisations' of the Universe, in which $\delta_{\mathbf{k}}$ values vary in both amplitude and phase [17]. If the phases are random, the density field has Gaussian statistics and the mean value of the perturbation $\delta(\mathbf{x})$ across the statistical ensemble is identically zero by definition, while its variance is

$$\sigma^2 = \sum_{\mathbf{k}} \left\langle |\delta_{\mathbf{k}}| \right\rangle = \frac{1}{V} \sum_{\mathbf{k}} \delta_{\mathbf{k}}^2 \ , \tag{2.30}$$

where the average is taken over an ensemble of realisations and $\left\langle |\delta_{\mathbf{k}}| \right\rangle$ is the contribution to the variance due to waves of wavenumber $\mathbf{k}$. Taking the limit $V \to \infty$ and assuming that the density field is statistically homogeneous and isotropic (i.e. there is no dependence on the direction of $\mathbf{k}$ but only on this modulus k), eq. (2.30) becomes

$$\sigma^2 = \frac{1}{2\pi^2} \int_0^\infty P(k) k^2 \, dk \quad \Leftrightarrow \quad \left\langle \delta_{\mathbf{k}} \delta_{\mathbf{k}_1} \right\rangle = (2\pi)^3 P(k) \delta_D^{(3)}(\mathbf{k} + \mathbf{k}_1) \ , \tag{2.31}$$

where $P(k)$ is the Power Spectral density function (PS), i.e. the Fourier transform of the 2 points correlation function[8] $\xi(r) = \left\langle \delta(x + r)\delta(x) \right\rangle$. It is possible to derive the dimensionless PS

$$\Delta(k) = \frac{1}{2\pi^2} P(k) k^3 \ , \tag{2.32}$$

useful to determin the power spectral index

$$
\begin{aligned}
n_s(k) - 1 &= \frac{d \ln \Delta(k)}{d \ln k} & \text{for scalar perturbations} \\
n_t(k) &= \frac{d \ln \Delta_t(k)}{d \ln k} & \text{for tensor perturbations.}
\end{aligned}
\tag{2.33}
$$

The author of [22] demonstrates that the matter PS observable today is

$$P(k, a) = 2\pi^2 \delta^2 \frac{k^{n_s}}{H_0^{n_s + 3}} T^2(k) \left(\frac{G(a)}{G(a = 1)} \right)^2 \ \text{for } a > a_{\text{Late}} \ , \tag{2.34}$$

in the case of CDM perturbations. If other energy-matter contributions are present (baryons, neutrinos, HDM, WDM, DE...), they can modify eq. (2.34).

Angular PS

Instead of considering the linear Fourier expansion, the perturbation field can be expressed in spherical coordinates as

$$\Theta(\mathbf{x}, \mathbf{p}, \eta) = \sum_{l=1}^\infty \sum_{m=-l}^l a_{lm}(\mathbf{x}, \eta) Y_l^m(\mathbf{p}) \ , \tag{2.35}$$

---

[8]The 2 points correlation function is defined thanks to the relation $\delta^2 P_2 = n^2[1 + \xi_{12}]dV_1 dV_2$ where n is the mean number density of sources and $\delta^2 P_2$ is the joint probability to find one of them in dV_1 and a second one in dV_2 at distance r_{12}. $\xi(r)$ measures the clustering properties of a distribution: in the random case $\xi(r_{12}) = 0$, while if $\xi(r_{12}) > 0$ the sources have the tendence to cluster (see [25] and [42] and for details).

where $\mathbf{p}$ are the field momenta and Y_l^m are the spherical harmonics (see Figure 2.3), a complete set of eigenfunctions[9] on the sphere; they are defined as

$$Y_l^m(\theta,\phi) \;=\; Ne^{im\phi}P_l^{|m|}(\cos\theta) \;, \tag{2.36}$$

being N a normalization constant and P_l^m the associated Legendre polynomials ([27] and [58])

$$
\begin{aligned}
P_l^m(s) &= (-1)^m(1-s^2)^{m/2}\frac{d^m}{ds^m}P_l^0(s) \\
&= (-1)^m(1-s^2)^{m/2}\frac{d^m}{ds^m}\left[\frac{1}{2^l l!}\frac{d^{l+m}}{ds^{l+m}}(s^2-1)^l\right]
\end{aligned}
\tag{2.37}
$$

where $l \;=\; 0,1... \propto \dfrac{1}{\theta}$ and $m \;=\; -l,...0...+l$.

The coefficients a_{lm} are the amplitudes varing in space and time, that can be calculated as

$$a_{lm}(\mathbf{x},\eta) = \int \frac{d^3k}{2\pi^3}e^{i\mathbf{k}\cdot\mathbf{x}}\int Y_{lm}^*(\mathbf{p})\,\Theta(\mathbf{k},\mathbf{p},\eta)\,d\Omega \;. \tag{2.38}$$

$m=0,\,n=1$ $m=1,\,n=1$ $m=2,\,n=2$ $m=4,\,n=5$

$m=0,\,n=2$ $m=1,\,n=2$ $m=2,\,n=3$ $m=5,\,n=7$

$m=0,\,n=3$ $m=1,\,n=3$ $m=3,\,n=6$ $m=6,\,n=10$
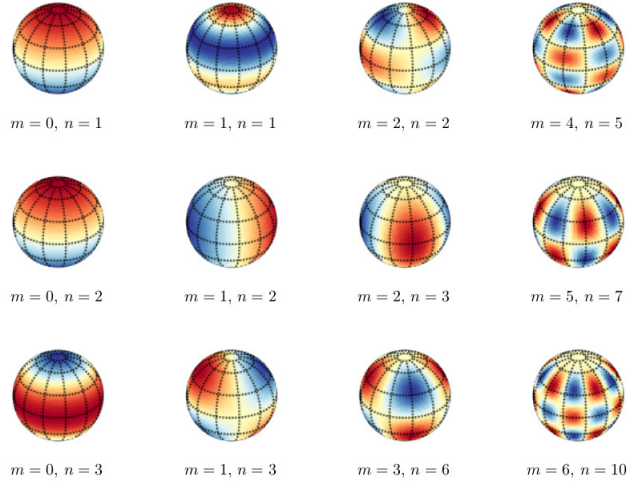
Figure 2.3: How $Y_l^m(\theta,\phi)$ looks like depending on l and m value. Image from [63].

The amplitudes are distributed with average $\langle a_{lm}\rangle = 0$ and variance $\langle a_{lm}a_{l'm'}^*\rangle = C_l\delta_{ll'}\delta_{mm'}$: for a given l, the variance is the same [22]. This means that the number of the possible C_l samplings is $\sum_{m=-l}^{l}|m|$ and depends on l (e.g. when $l=2$ there are 5 possible samplings, when $l=100$ they are 201); C_l have for this reason an intrinsic uncertainty due to the number of possible samplings. It is called cosmic variance and it is defined [22] as

$$\frac{\Delta C_l}{C_l} = \sqrt{\frac{2}{2l+1}} \;. \tag{2.39}$$

Lower l, i.e. larger angular scales θ, have an higher uncertainty.

---

[9]Taken a linear operator F defined over a funcion space, its eigenfunctions g satisfy the relation $Fg = \lambda g$ where λ is a scalar called the eigenvalue.

$\Theta(\mathbf{x}, \mathbf{p}, \eta)$ can be Fourier transformed to $\Theta(\mathbf{k}, \mathbf{p})$; this one depends on the amplitude, the initial phase $\delta_{\mathbf{k}}$ and the evolution $\Theta(\mathbf{k}, \mathbf{p})/\delta_{\mathbf{k}}$. As [22] explains, it is possible to get

$$< \Theta(\mathbf{k}, \mathbf{p}), \Theta^*(\mathbf{k}', \mathbf{p}') > = (2\pi)^3 \, \delta_D^{(3)}(\mathbf{k} - \mathbf{k}') \, P(k) \, \frac{\Theta(\mathbf{k}, \mathbf{p})}{\delta_{\mathbf{k}}} \frac{\Theta^*(\mathbf{k}', \mathbf{p}')}{\delta_{\mathbf{k}'}} \; . \qquad (2.40)$$

Squaring and integrating eq. (2.40) (see [22]), the Angular PS (APS) obtained is

$$\begin{aligned} C_l &= \int \frac{d^3k}{(2\pi)^3} \, P(k) \, \int d\Omega \, Y_{lm}^*(\mathbf{p}) \, \frac{\Theta(\mathbf{k}, \mathbf{k} \cdot \mathbf{p})}{\delta_{\mathbf{k}}} \int d\Omega' \, Y_{lm}(\mathbf{p}') \, \frac{\Theta^*(\mathbf{k}, \mathbf{k} \cdot \mathbf{p}')}{\delta_{\mathbf{k}}^*} \\ &= \frac{2}{\pi} \int_0^\infty k^2 P(k) \left| \frac{\Theta_l(k)}{\delta_k} \right|^2 dk \; . \end{aligned} \qquad (2.41)$$

The evolution of the PS (i.e. $T(k)$ and $G(a)$) from the primordial one is encapsulated in $|\Theta_l(k)/\delta_k|$.

It is possible to calculate C_l for some particular kinds of observations; for example, in [31] it is calculated for the galaxies number counts. In this work it is used the same derivation despite the observable is the number counts of NS-NS merger events.

The matter PS $P(k)$ obtained in linear perturbation theory has to be converted to the galaxy number count PS: to do it a bias has to be defined in order to distinguish the tracer (i.e. the NS-NS merger rate, see Sec. 2.3.1) from the underlying CDM distribution. In this work, a linear bias is assumed; [47] (see Chapter 4) defines it as

$$b(z) = b_0 + \frac{b_z}{G(z)} \; , \qquad (2.42)$$

where $b_0 = b_z = 1$ and $G(z)$ from eq. (2.29); the NS-NS PS is therefore defined as $P_{NS\text{-}NS}(k) = b^2 P(k)$ and it has to be projected to C_l. In order to derive the C_l expression, the number of detectable sources per solid angle $\mathcal{S}$ has to be defined: it depends on the selection function of the survey (see Sec. 2.3.1) and it differs from the unbiased quantity $\bar{\mathcal{S}}$ by $\mathcal{S} = \bar{\mathcal{S}}(1 + b\delta(\mathbf{x}))$ in the simplest case. [31] shows how to explicitly obtain $\Delta(\mathbf{x}, \hat{\gamma}) = (\mathcal{S} - \bar{\mathcal{S}})/\bar{\mathcal{S}}$, which depends on the location $\mathbf{x}$ and the direction $\hat{\gamma}$ of the observation. Calculating $\langle \Delta(\mathbf{x}, \hat{\gamma_1}), \Delta(\mathbf{x}, \hat{\gamma_2}) \rangle$ (see [31]) and taking its Legendre transform it is possible to get

$$\begin{aligned} C_l &= \frac{2}{\pi} \int k^2 P(k) f_l(k)^2 \, dk \\ \text{where } f_l(k) &= \frac{1}{\bar{\mathcal{S}}} \int dz \frac{1}{F(x)} \frac{d\chi}{dz} j_l(kx) r^2 G(x) b(x) \bar{s}(r) T_{NL}(k, z) \; . \end{aligned} \qquad (2.43)$$

The quantity χ is the comoving distance of the point $\mathbf{x}$; $\bar{s}(\chi)$ is the comoving density of detectable sources, related to $\bar{\mathcal{S}}$ by $\chi^2 \bar{s}(z) d\chi/dz = d\bar{\mathcal{S}}/dz$; $F(x) = 1$ for Universe with zero mean curvature and $T_{NL}(k, z)$ is the correction factor for non linear evolution.

The spherical Bessel functions $j_l(kx)$ are the canonical solutions of the equation

$$x^2 \frac{d^2y}{dx^2} + x \frac{dy}{dx} + (x^2 - l^2)y = 0 \; . \qquad (2.44)$$

The Bessel functions can be distinguished in first and second type. The former in the origin of the coordinate system have finite value if $l \geq 0$ while if $l < 0$ they diverge;

the latter, instead have a singularity in the origin. The first type Bessel functions can be written as

$$J_l(x) = \sum_{m=0}^{\infty} \frac{(-1)^m}{m! \, \Gamma(m+l+1)} \left(\frac{x}{2}\right)^{2m+l} , \qquad (2.45)$$

where $\Gamma(s) = \int_0^{+\infty} t^{s-1} e^{-t} dt$ and $\Gamma(n+1) = n!$ if $n \in \mathbb{N}$. If $l \in \mathbb{Z}$, $J_{-l}(x) = (-1)^l J_l(x)$.

The spherical Bessel are the solutions of

$$x^2 \frac{d^2 y}{dx^2} + 2x \frac{dy}{dx} + (x^2 - l(l+1))y = 0 , \qquad (2.46)$$

which is the radial part of the Helmholtz equation $\nabla^2 A + k^2 A = 0$. They can be calculated as

$$j_l(x) = \sqrt{\frac{\pi}{2x}} J_{l+\frac{1}{2}}(x) . \qquad (2.47)$$

Eq. (2.43) is valid for all angular scales but for smaller ones ($l > 30$) it is possible to use the Limber approximation in order to avoid the Bessel function calculation (which is computationally very expensive), assuming in this way a flat sky. In this case, the expression for the C_l is [31]

$$C_l = \frac{1}{\bar{\mathcal{S}}^2} \int dz \frac{d\chi}{dz} P\left(k = \frac{l}{\chi}, z\right) \left[\bar{s}(z) G(z) \; b \; T_{NL}\left(k = \frac{l}{\chi}, z\right)\right] . \qquad (2.48)$$

The APS can be used to calculate the auto and cross correlation function, as Chapter 3 describes.

2.2.3   Gravitational Lensing

On small angular scales, inhomogeneities are very widespread: as described in Sec. 2.2.1, they originate deformations in the RW metric, changing the spacetime curvature because of their mass. This implies that a light ray passing near one of them is deflected, as the equation $ds^2 = 0$ shows when perturbing the RW metric (see eq.(2.1), (2.17), [25] and [42] for more details): this behaviour can be compared to the optical effect of lenses, which deviate the light paths because of having a refractive index[10] different from the surrounding.

To model the gravitational lensing effect (see [25] and [42] for details), it is possible to consider a thin, plane lens, due to a weak gravitational field Φ: in this way the metric can be assumed locally Minkowskian, with small Newtonian perturbations, and the light ray is deflected by a small angle which value is given by

$$\alpha \; = \; 2 \int \nabla_\perp \Phi \, dl = \frac{4M}{B} \; << \; 1 \; \text{rad} , \qquad (2.49)$$

where $\nabla_\perp$ is the gradient calculated in the orthogonal direction to the light propagation path and B is the impact parameter of the light ray with respect to the lens barycenter.

This deviation leads to a change in the observed position and luminosity of the source, depending on the lens mass distribution and the relative position between the source, the lens and the observer. It is possible to distinguish between

---

[10]The refractive index describes how light propagates inside a medium and it can be expressed as $n_R = c/v$ where c is the speed of light in the vacuum and v is its phase velocity in the medium. When a light ray passes from one medium to another, it can be bent; the deviation amplitude is given by the Snell law of refraction $n_{R1} \sin \theta_1 = n_{R2} \sin \theta_2$ being θ_1, θ_2 the angles the ray forms with the perpendicular to the division surface between the two mediums.

- strong lensing, which produces multiple images and rings (see Figure 2.4a);

- micro lensing, due to compact objects in the Milky Way halo that modify the light curve of background stars(see Figure 2.4b);

- weak lensing, that affects the ellipticity and the orientation of observed galaxies when a DM halo is interposed between them and the observer (see Figure 2.4c).

Since only weak lensing will play a role in our analysis, we will focus just on it in the following.

(a)

(b)

(c)

(d)
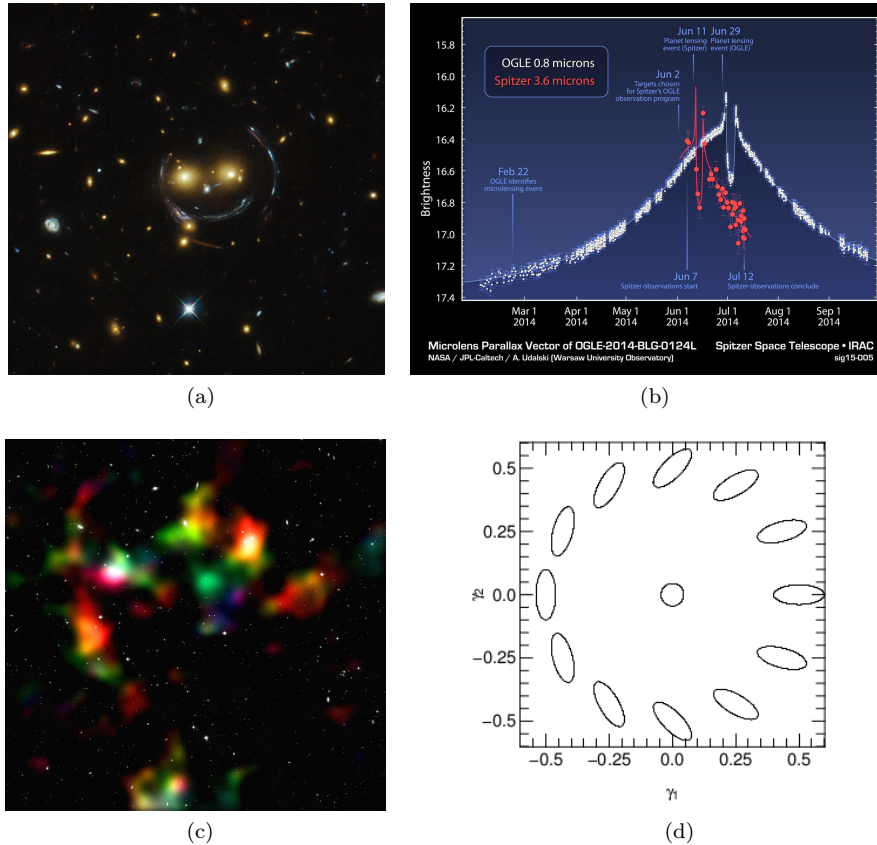
Figure 2.4: Figure 2.4a shows the galaxy cluster SDSS J1038+4849 bending the light coming from background sources; the Einstein ring that appears indicates the alignment between the source and the lens along the LOS. Figure 2.4b shows the increase in brightness on the light of a background star during a microlensing event (i.e. when a foreground star or planet passes in front of it); data are taken from NASA's Spitzer Space Telescope and from the Optical Gravitational Lensing Experiment (OGLE) telescope located in Chile: the great distance between them causes the time delay between the magnification in the two curves. Figure 2.4c is a reconstruction of the matter distribution in the COSMOS field, inferred from the weak gravitational lensing distortions that appears on the shapes of background galaxies. Finally, Figure 2.4d represents how a circular distribution is rotated and modified into an elliptical one, depending on the weak lensing shear (γ_1, γ_2) values. The first image is taken from [49], the second and the third from [50], the last one from [33].

Weak Lensing PS

Weak gravitational lensing distorces the images of distant galaxies, coherently deforming them by the matter inhomogeneities along the LOS. This is called cosmic shear and is due to the LSS of the Universe; thus, by measuring galaxies shape correlations it is possible to study their properties and evolution as well as the geometry of the Universe [33].

To describe this approach, in a comoving system eq. (2.49) can be generalized to more than one thick and non-planar lens. In linear approximation, it is possible to define (see [33] for details) the amplification matrix $\mathcal{A} = \partial\beta/\partial\theta$, where β are the unlensed source coordinates and θ are the lensed image coordinates; in this way, $\mathcal{A}^{-1}$ describes the local mapping of the source light distribution to image coordinates [33]. Under these condition, it is possible to define a 2D lensing potential ψ such that

$$\mathcal{A}_{ij} = \delta_{Dij} - \partial_i\partial_j\psi \;\Leftrightarrow\; \mathcal{A} = \begin{pmatrix} 1 - \mathsf{k} - \gamma_1 & -\gamma_2 \\ -\gamma_2 & 1 - \mathsf{k} + \gamma_1 \end{pmatrix}$$

$$\mathsf{k}(\theta) = \frac{1}{2}(\partial_1\partial_1 + \partial_2\partial_2)\psi = \frac{1}{2}\nabla^2\psi \quad \text{is the scalar convergence}$$

$$\gamma_1(\theta) = \frac{1}{2}(\partial_1\partial_1 - \partial_2\partial_2)\psi \qquad \gamma_2(\theta) = \partial_1\partial_2\psi$$

$$\Rightarrow \; \gamma(\theta) = \gamma_1 + i\gamma_2 \quad \text{is the shear.}$$

(2.50)

The convergence is an isotropic change of the observed size of the source image and can be represented as a projection on the LOS of the density contrast $\delta(\mathbf{x})$; the shear instead quantifies an anisotropic stretching, e.g. it turns a circular distribution into an elliptical one, as Figure 2.4d shows.

When considering the Cosmological lensing due to LSS, k and γ values are about a few percent: each source is weakly lensed and there are not multiple images. Since this effect arises from variations in the gravitational potential along the light path, weak lensing contains information about the clustering of DM mass along the LOS, which causes both a correlated distortion of source images, which depends on the shear, and a magnification μ (i.e. an increase in brightness) of high redshift sources [8]. This is linked with the convergence and it is given by

$$\mu = (\det|\mathcal{A}|)^{-1} = \frac{1}{|(1-\mathsf{k})^2 - \gamma^2|} = 1 + \delta\mu \simeq 1 + 2\mathsf{k} , \qquad (2.51)$$

where $\delta\mu$ are the magnification fluctuations and the last approximation holds in the weak lensing regime.

The convergence field in flat sky approximation can be expanded (see [8] for details) in Fourier modes as $\mathsf{k}(l) = \int d^2\theta \mathsf{k}(\theta)e^{il\cdot\theta}$; the 2 points correlation function of these modes defines [8] the APS

$$\langle \mathsf{k}(l)\mathsf{k}^*(l')\rangle = (2\pi)^2 C_l^{\mathsf{kk}}\delta_D(l - l')$$

$$\Rightarrow C_l^{\mathsf{kk}} = \frac{9H_0^4\Omega_m^2}{4}\int_0^{\chi_H}\left(\frac{\bar{W}(\chi)}{a(\chi)}\right)^2 P_\delta\left(\frac{l}{\chi}, \chi\right)d\chi .$$

(2.52)

The integral is evaluated over the comoving distance χ from 0 to the horizon, defined as $\chi_H = \int dz/H(z)$; the weighting function is $\bar{W}(\chi) = \int_\chi^{\chi_H} d\chi' P(\chi')(\chi' - \chi)/(\chi')$, where it has been defined $P(\chi')d\chi' = p(z)dz$ and $p(z)$ is the matter distribution function. On angular scales smaller than about $10'$, C_l^{kk} is dominated by galaxy clusters [8]; in

the case of weak lensing the shear APS $C_l^{\gamma\gamma}$ is equal to C_l^{kk}, while the magnification fluctuations PS is

$$C_l^{\delta\mu\delta\mu} = 4C_l^{\mathsf{kk}} = 4C_l^{\gamma\gamma} \; . \tag{2.53}$$

2.3 How GWs can help Cosmology

In this section we will discuss several uses of GWs to extract Cosmological information (Sec. 2.3.2). Before dwelling into these topics, it is however important to provide a preliminary introduction to the observation of merging events, considered as Cosmological sources (Sec. 2.3.1).

2.3.1 Number of NS-NS merging events

To estimate the NS-NS merging events APS (see Chapter 4) and consequently obtain a powerful instrument to study Cosmology via GW emission of such events, it is necessary to know the merger rate history $\dot{n}(z)$. In this thesis, we will express this as a function of the redshift z, following [19]: here, $\dot{n}(z)$ it is defined as

$$\dot{n}(z) = \dot{n}_0 r \quad \text{with} \quad r = \begin{cases} 1 + 2z & z \leq 1 \\ \frac{3(5-z)}{4} & 1 < z \leq 5 \\ 0 & z > 5 \; , \end{cases} \tag{2.54}$$

where $\dot{n}_0 = 10^{-6}\mathrm{Mpc}^{-3}\mathrm{yr}^{-1}$ is the value [47] gives for the merger rate today. It is given by the product of the current merger rate in the Milky Way ($\simeq 10^{-4} - 10^{-6}\mathrm{yr}^{-1}$), and a factor that extrapolates the average rate in the Universe ($1.1 - 1.6 \cdot 10^{-2} h_{70}^{-1}\mathrm{Mpc}^{-3}$).

Observational sources selection

Not all sources in the sky can of course be detected by a given survey, due to its flux limitation and observational selection function.

Flux limitation implies that some sources can not be identified if their apparent brightness is lower than a threshold value, which is linked with the sensibility and the Signal-to-Noise ratio (SNR, see Chapter 3) of the instrument used. Sources can thus be excluded either because they are intrinsically faint or because they appear this way since they are very far. When observing GWs, the same problem can occur considering the wave amplitude instead of the brightness. A calculation of how many NS-NS events ΔN_m can be detected in an observation time $\Delta\tau_0$ can be found in [19]. Summing $\dot{n}(z)$ over all the redshift values, it is possible to get

$$\dot{N} = \frac{\Delta N_m}{\Delta \tau_0} = \int_0^\infty 4\pi \left[a_0 r_1(z)\right]^2 \dot{n}(z) \frac{d\tau_1}{dz} dz$$

$$\text{where} \quad a_0 r_1(z) = \frac{1}{H_0} \int_0^z \frac{dz'}{\sqrt{(1 - \Omega_\Lambda(1+z)^3 + \Omega_\Lambda}} \tag{2.55}$$

$$\frac{d\tau_1}{dz} = \frac{1}{H_0} \frac{1}{1+z} \sqrt{(1 - \Omega_\Lambda(1+z)^3 + \Omega_\Lambda} \; ,$$

and, integrating in time, N_m is found.

It is important to note that a flux limited survey is also limited in redshift. However, the lensing effect has to be taken into account (see Sec. 2.2.3): if a source is magnified by some matter distribution settled along the LOS, it can be included in

the survey even if it is farther than others that have been excluded. The observed source number counts N_m is therefore affected by the magnification bias s (see [21] for details). Considering that the source number counts is related to the threshold flux by $\bar{N} \simeq F_t^{-\alpha}$, and it is affected by the lensing magnification as $N_m(> F_t, z)/\bar{N}(> F_t, z) = \mu^{\alpha-1}$, it is possible to define

$$s = \frac{\partial \log_{10} \bar{N}}{\partial m_t} = -\frac{1}{2.5}\frac{\partial \ln \bar{N}}{\ln F_t} = \frac{1}{2.5}\alpha \ , \qquad (2.56)$$

(where $m_t = m_0 - 2.5\log_{10}(F_t/F_0)$ is the apparent magnitude associated to F_t and it is defined thanks to the reference values m_0, F_0), in order to get

$$\frac{N_m - \bar{N}}{\bar{N}} \simeq 2(\alpha - 1)\mathsf{k} = (5s - 2)\mathsf{k} \ . \qquad (2.57)$$

In the GWs case the same argument can be applied. Nevertheless, in this work the magnification bias is not considered: it is set to $s = 2/5$ in order to get $N_m = \bar{N}$.

As for the observational selection function, it is due to the fact that the survey is realized dividing into bins the redshift interval in which the sources are observable. The method is the same as the one used to study the galaxies number counts (see for example [7], [15] and [30]) where the angular correlations are measured in samples selected in different shell, defined by the redshift bins. To approximate the redshift binning, it is possible to consider (see [30] for details) that photometric redshift estimates are distributed as Gaussians. The ith bin can therefore be described as [43]

$$W(z, z_i) = \frac{1}{2}\frac{dN_m(z)}{dz}\left[\text{erfc}\left(\frac{(i-1)\Delta - z}{\sigma(z)\sqrt{2}}\right) - \text{erfc}\left(\frac{i\Delta - z}{\sigma(z)\sqrt{2}}\right)\right] \ , \qquad (2.58)$$

erfc being $\text{erfc}(x) = 2/\pi \int_x^\infty e^{-t^2} dt$ the complementary error function[11] dN_m/dz is obtained deriving in dz and integrating in dt the eq. (2.55), Δ is a scalar quantity, z_i is the mean redshift in the bin and $\sigma(z) = 0.02(1+z)$. The fact that in each redshift bin sources are selected by a Gaussian implies that not all of them are observed; moreover, two different Gaussians can overlap and one source can be included in both of them. This kind of selection is applied in Chapter 4 to infer Cosmological informations from the NS-NS mergers APS.

2.3.2   GW application in Cosomology

One of the most promising ways GWs can be used to infer Cosmological parameters is to use them as standard sirens. This idea is similar to the standard candles one described in Sec. 2.1.1 and it is achieved comparing the D_L measurements derived from GWs (see Sec. 1.3.2) to the redshift z of their sources. The latter can be obtained from the spectrum of the host galaxy in which the GW event was originated or from the one of its EM counterpart, when this is present (see Sec. 1.2).

The redshift z can give an estimate of the Universe size when the GWs were emitted, while D_L is linked with the expansion undergone by the Universe in the time between that moment and the observation [20]. In particular, from eq. (2.15) it can

---

[11]The complementary error function is related with the error function, which describes the probability distribution of the errors of a normal distribution.

be seen that a D_L measurement would give information about the Cosmological parameters[12] (e.g. Ω_m, Ω_Λ); however, this will be possible only with the third generation GW observatories and with the space ones (see Sec. 1.3.1), which will measure GW events at high redshifts. Future ground-based GW observatories will measure events only up to $z \simeq 0.3$: in this case, eq. (2.15) can be approximated as $D_L \simeq z/H_0$ and constraints on H_0 can be derived. These measurements will hopefully help understanding the current discrepancy between the value obtained from PLANCK data ($H = 70.2 \pm 1.4$ km s^{-1}Mpc^{-1}) and from cosmic distance ladder[13] ($H = 73.8 \pm 2.4$ km s^{-1}Mpc^{-1}) (see [53] for details). Figure 2.5 shows the results of a simulation for a 3 detector network: the Probability Density Function (PDF) obtained for a high number of events well determines the value of H_0. This can be combined with the the redshift of the last scattering surface, obtained from the CMB (see Sec. 2.1) in order to gain information on the curvature of the Universe and the DE EoS.
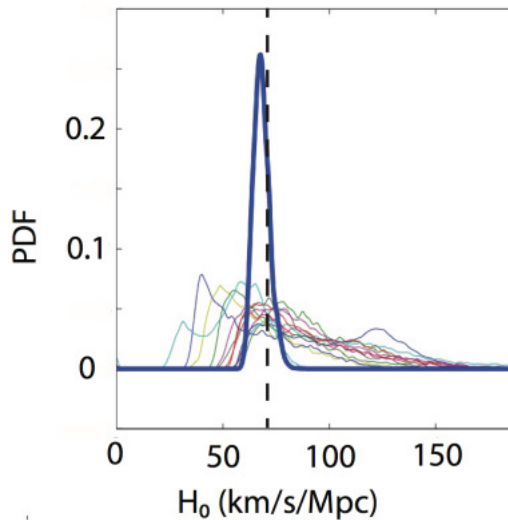

Figure 2.5: A simulated sample of 15 NS-NS merger events observed by LIGO Livingston, LIGO Hanford, Virgo (see Sec. 1.3.1). The light coloured lines represent the H_0 PDF for each event, while the thicker blue one is the joint PDF of all the events: it is narrower and nearer to the vertical dashed line that denotes the value $H_0 = 70.5$ km s^{-1}Mpc^{-1} used to generate the simulations. Image from [53].

GW set of data are independent from the ones from those coming from other kind of observations (e.g. CMB, galaxies counts...) and their errors are uncorrelated. Moreover, when used to study the $D_L - z$ relation, GWs provide a small error. In fact, they depend on the number of detectors used and on their noise curves. These can be well characterized and they provide small errors (see [20] for details), mainly because the merger are well modeled thanks to the PN approximation (see Sec. 1.3.2); for space

---

[12]Eq. (2.15) has been derived in the case of flat Universe. It is possible to generalize it [53] as

$$D_L(z) = \frac{1+z}{H_0\sqrt{\Omega_k}} \sinh\left[\sqrt{\Omega_k} \int_0^z \frac{H_0}{H(z')}\, dz'\right] \quad \text{where} \quad \Omega_k = 1 - \Omega_m - \Omega_\gamma - \Omega_\Lambda \ ,$$

[13]The cosmic distance ladder is the succesion of methods used to determine distances of astronomical sources.

interferometers this will be even better because using free masses the instruments will be self-calibrating. Also the lensing magnification effect (see Sec. 2.2.3) has to be taken into account. It introduces a dispersion in the $D_L - z$ diagram (see Figure 2.6), from which the convergence PS can be obtained. From this one, also the shear PS can be derived (see Sec. 2.2.3) and compared with the one reconstructed from the background galaxies ellipticity distribution, which depends on the relative distance between the observer, the lens and the source and on the lenses distribution [20].
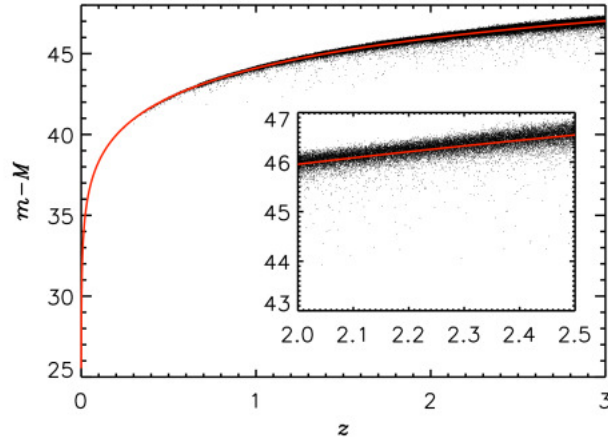

Figure 2.6: $D_L - z$ diagram for simulated data from BBO (see Sec. 1.3.1), where D_L is expressed as distance modulus $m - M$ being m the apparent magnitude and M the absolute one (i.e. the magnitude the source would have if it was located at distance $= 10$ pc from the observer). The red line represents the "true" relation; the points deviate from it because of lensing magnification. Image from [20].

The bigger problem in the use of standard sirens derives from redshift measurements, that can be obtained only if an EM source is present. The first way to obtain it is to identify the host galaxy where the GW emission occurred, but to do it GW interferometers with a good angular resolution are required and, as explained in Sec. 1.3.1, this will be achieved only with future observatories. Even if the host galaxy was localized, it is not so easy to identify it: it could be found in a crowded enviroment, or it could be too faint to be observed by the EM survey (see Sec. 2.3.1).

The second way to get an EM signal linked with a GW observation is to identify its EM counterpart. This can happen only for binary systems containing at least one NS (see Sec. 1.2) and can be related to an isotropic (e.g. kilonovae) or beamed (e.g. Gamma Ray Bursts (GRB)) emission. In the latter case, problems can occur if the beam is oriented in a way that prevents its observation.

To avoid the EM problem, several solutions have been proposed. The redshift z can not be obtained from the GWs alone, because it is degenerate with the mass (see Sec. 1.3.2). The degeneracy could be broken if the NS EoS was known: in fact, it can add a tidal deformation in the GW phase that, if measerued, would give additional information (see [53] for details). Alternatively, galaxy catalogues can be used (there is a correlation between the galaxy mass and luminosity and the probability that a GW event occurs, see [51]) or a chirp mass distribution can be assumed using the stellar populations synthesis models. In Chapter 4 another method is presented: it has been proposed in [47] and carefully analized in this work.

Other applications

Besides their use as standard sirens, GWs have other applications in Cosmology. They can be used to test GR under different perspectives; for example, the ratio between the GW velocity and the speed of light has already been measured from the NS-NS merger event GW170817 (see Figure 1.4) and its value has be constrained to $|v_{GW}/c| \lesssim 4.5 \cdot 10^{-16}$ [24]. This one permits to test modified gravity and DE evolution models: some of them, in fact, use particular metrics to explain the accelerated expansion of the Universe and at the same time they provide for GWs $v_{GW} \neq c$. However, as long as the limit on $|v_{GW}/c|$ is set, some of these models can be excluded (see [24] for details).

Moreover, the GR lensing description can be tested comparing the magnification obtained from GWs and the shear observed thanks to the ellipticity of background galaxies.

Finally, a deep knowledge of the Astrophysical GWs allows removing their wavefronts from the data, in order to detect the primordial GW signal (see [51]). This one, combined with the CMB polarization data will provide a test for the Inflation models.

Chapter 3

How future experiments can be forecasted?

This Chapter describes some of the statistical techniques that can be used to forecast future experiments. In particular, as well as theoretical models can be constraint when data have been collected (Sec. 3.1), it is possible to estimate how well their parameters will be obtained before the observations start (Sec. 3.2). This can be done also to forecast how well an APS will be measured by future surveys (Sec. 3.3).

3.1 From data to parameter constraints

3.1.1 Likelihood function

Data taken from observations can be used to study the validity of theoretical models and to constrain their parameters ϑ. As a matter of fact, the data set $\mathcal{D}$ can be used to obtain the expectation value and the errors of the distribution characterized by conditional probability[1] $P(\vartheta|\mathcal{D})$, called the posterior. The probability distribution is linked to the physical properties thanks to some quantities, called the estimators ϵ (e.g. the mean value), that can be derived both from theory and from data. The estimators are unbiased if their expectation value $\langle\epsilon\rangle = \epsilon_0$, ϵ_0 being the "true" value [29]; in this case, the distribution that they descibe is unbiased too.

$P(\vartheta|\mathcal{D})$ describes the probability of deriving a particular set ϑ when $P(\mathcal{D})$ is given; however, even if $P(\mathcal{D})$ is not known, $P(\vartheta|\mathcal{D})$ can be linked to the probability of the data distribution conditioned by the knowledge of the parameters, that the Bayes theorem (see [68] for details) shows to be

$$P(\vartheta|\mathcal{D}) = \frac{P(\mathcal{D}|\vartheta)P(\vartheta)}{P(\mathcal{D})}$$
$$\simeq L(\mathcal{D};\vartheta) \,, \tag{3.1}$$

where $P(\vartheta)$, $P(\mathcal{D})$ and $P(\mathcal{D}|\vartheta) = L(\mathcal{D};\vartheta)$ are respectevely called prior, evidence and likelihood function. The equivalence between $P(\vartheta|\mathcal{D})$ and $L(\mathcal{D};\vartheta)$ is valid when $P(\mathcal{D}) = 1$, i.e. when data has already been gotten. It also assumes the indifference

---

[1]The conditional probability is a measure of the probability of an event A given by assumption that another event B has occurred. It is usually defined as $P(A|B) = P(A \cap B)/P(B)$(Kolmogorov definition).

principle, under which all the ϑ values are equiprobable and the prior $P(\vartheta) \simeq$ cost is flat.

ϑ values can be obtained in this way if the data have sufficiently high "statistical power": if the results change a lot when the prior is varied, $\mathcal{D}$ can not be used to constraint the parameters (see [29] for more details).

$L(\mathcal{D}; \vartheta)$ describes the probability that, when a model is assumed, a certain experiment can obtain a particular set of data [22]. Its maximum value and width can be used to derive the parameters best estimate and the error associated with it: particularly, when the prior is constant the $L(\mathcal{D}; \vartheta)$ maximum value corresponds to the $P(\vartheta|\mathcal{D})$ peak. The maximum likelihood can always be found by differentiating $L(\mathcal{D}; \vartheta)$ with respect to each ϑ_α.

If the N data are Gaussianly distributed, the likelihood in the parameter space can be approximated [68] by a multivariate Gaussian distribution

$$L(\mathcal{D}; \vartheta) = \frac{1}{(2\pi)^{N/2} |\det C|^{1/2}} \exp\left[-\frac{1}{2} \sum_{ij} (\mathcal{D}_i - \mu_i) C_{ij}^{-1} (\mathcal{D}_j - \mu_j)\right] , \qquad (3.2)$$

where $C = \left\langle (\mathcal{D}_i - \mu_i)(\mathcal{D}_j - \mu_j) \right\rangle$ is the Covariance matrix as defined in Sec. 3.2. This kind of distribution is commonly assumed: the likelihood is a multivariate Gaussian if the errors are Gaussianly distributed, but the approximation holds even if they are not, as the central limit theorem[2] assures (see [68] for details).

As for the errors, they can be defined in different ways. It is called conditional error σ_α^{cond} the uncertainty obtained for ϑ_α when all the other parameters have been set to fixed values. This can be done thanks to the marginalization process, which consists in removing the parameters dependence by integrating their acceptable values, e.g. the ϑ_1 marginalized distribution is $P(\vartheta_1) = \int d\vartheta_2...d\vartheta_N$.

σ_α^{cond} is the minimum error that can be obtained on the parameter ϑ_α; it can be calculated [68] as

$$\sigma_\alpha^{cond} = \frac{1}{\sqrt{H_{\alpha\alpha}}} , \qquad (3.3)$$

where H is the Hessian matrix as defined in Sec. 3.1.2. It is not frequently used; instead the marginal error is very common: it can be defined when the likelihood is a multivariate Gaussian distribution, as

$$\sigma_\alpha = \sqrt{(H^{-1})_{\alpha\alpha}} . \qquad (3.4)$$

When more than one consistent data set $\mathcal{D}_1, \mathcal{D}_2$ is available, these can be combined to get better constraints on the model parameters. If the sets are independent, the combination is done by multiplying their likelihood: the Bayes theorem assures that it is possible both to consider the data set $(\mathcal{D}_1, \mathcal{D}_2)$ with prior $P(\theta)$ and to think of the data set $\mathcal{D}_2$ with prior $(\mathcal{D}, P(\vartheta))$ (see [29] for details). If some of the data sets are dependent one on another, Covariance has to be considered instead (see Sec. 3.2.2).

---

[2]The central limit theorem in statistics assures that, when independent random variables are added, their sum tends towards a Gaussian distribution. In the case presented in the text, the variables are independent measurements of the data.

3.1.2   Covariance matrix

Two different parameters ϑ_α and ϑ_β can have similar effects on the observables; in this case, when they are estimated from data, they can correlate, even if physically they don't relate. Their correlation is enclosed [68] in the Hessian matrix

$$H_{\alpha\beta} = -\frac{\partial^2 \ln L(\mathcal{D}; \vartheta)}{\partial\vartheta_\alpha\partial\vartheta_\beta} \ . \tag{3.5}$$

If this matrix is diagonal, the parameters are uncorrelated.

When the errors are distributed Gaussianly, H is linked to the Covariance matrix $C = \langle D \rangle$, where $D = (\mathcal{D} - \mu)(\mathcal{D} - \mu)^T$ is the data matrix and $\mu = \langle \mathcal{D} \rangle$ is the average vector. Defining $\mathcal{L} = -\ln L$, from eq. (3.2), it is possible to get (see [29] for details)

$$
\begin{aligned}
2\mathcal{L} &= \ln(\det C) + (\mathcal{D} - \mu)C^{-1}(\mathcal{D} - \mu)^T \\
&= \mathrm{tr}[\ln C + C^{-1}D] \\
\Rightarrow 2\frac{\partial\mathcal{L}}{\partial\vartheta_\alpha} &= \mathrm{tr}\left[C^{-1}\frac{\partial C}{\partial\vartheta_\alpha} + C^{-1}\frac{\partial D}{\partial\vartheta_\alpha} - C^{-1}\frac{\partial C}{\partial\vartheta_\alpha}C^{-1}D\right] \ .
\end{aligned}
\tag{3.6}
$$

It is possible to demonstrate [29] that $\langle \mathcal{D}\mathcal{D}^T \rangle = C + \mu\mu^T$, $\langle \partial D/\partial\vartheta_\alpha \rangle = 0$ and

$$\left\langle \frac{\partial^2 D}{\partial\vartheta_\alpha\partial\vartheta_\beta} \right\rangle = \frac{\partial\mu}{\partial\vartheta_\alpha}\left(\frac{\partial\mu}{\partial\vartheta_\beta}\right)^T + \frac{\partial\mu}{\partial\vartheta_\beta}\left(\frac{\partial\mu}{\partial\vartheta_\alpha}\right)^T \ . \tag{3.7}$$

This properties can be used to rewrite eq. (3.6) as

$$
\begin{aligned}
\left\langle \frac{\partial\mathcal{L}}{\partial\vartheta_\alpha} \right\rangle &= \mathrm{tr}\left[\left\langle C^{-1}\frac{\partial C}{\partial\vartheta_\alpha}\right\rangle + \left\langle C^{-1}\frac{\partial D}{\partial\vartheta_\alpha}\right\rangle - \left\langle C^{-1}\frac{\partial C}{\partial\vartheta_\alpha}C^{-1}D\right\rangle\right] \\
&= \mathrm{tr}\left[\left\langle C^{-1}\frac{\partial C}{\partial\vartheta_\alpha}\right\rangle - \left\langle C^{-1}\frac{\partial C}{\partial\vartheta_\alpha}\right\rangle\right] = 0
\end{aligned}
\tag{3.8}
$$

$$\text{and} \quad \left\langle \frac{\partial^2\mathcal{L}}{\partial\vartheta_\alpha\partial\vartheta_\beta} \right\rangle = \frac{1}{2}\mathrm{tr}\left[\left\langle -C^{-1}\frac{\partial C}{\partial\vartheta_\alpha}C^{-1}\frac{\partial C}{\partial\vartheta_\beta}\right\rangle + \left\langle C^{-1}\frac{\partial D}{\partial\vartheta_\alpha\partial\vartheta_\beta}\right\rangle\right] = \langle H \rangle \ .$$

Eq. (3.13) and (3.16) in Sec. 3.2 and 3.2.2 show that H and C are also stricly linked to the Fisher matrix.

It is possible to show (details in [22]) that $C = N_l + C_s$, being N_l the Covariance matrix for the instrumental noise, while C_s is the one for the signal. The first one can be obtained from the data, the latter thanks to the convolution between the model and the window function of the experiment: this is due to the pixelization of the detector and the beam size of the observations (see [22] for details).

The χ^2 function

The Covariance matrix can be used to describe how much a model agrees with a given set of data, being therefore suitable to analyze it. C is in fact involved in the calculation of the merit function χ^2, which maximum value gives the best fit parameters for the data interpolation. The author of [68] defines it as

$$\chi^2 = \sum_i w_i[\mathcal{D}_i - \mathcal{Y}(x_i|\vartheta)]^2 \ , \tag{3.9}$$

where $\mathcal{D}_i$ are the data, $\mathcal{Y}(x_i|\vartheta)$ the model used to describe them thanks to the coordinates x_i and the parameters ϑ and w_i are some weights. The minumum value for them is $w_i = 1/\sigma_i$ (σ_i being the error on the ith data point); when this value is used and the data correlate, eq. (3.9) can be transformed into

$$\chi^2 = \sum_{ij} (\mathcal{D}_i - \mu_i) C_{ij}^{-1} (\mathcal{D}_j - \mu_j) \ . \tag{3.10}$$

To understand if a model is adequate for the data interpolation, the χ^2 function has to be minimized in order to get the best fit. When the data can be approximated by a multivariate Gaussian distribution (see Sec. 3.1.1), $L(\mathcal{D}; \vartheta) \propto \exp(-1/2\chi^2)$ and the best fit is the one that maximizes the likelihood function.

3.1.3 Signal-to-Noise Ratio

The Signal-to-Noise Ratio (SNR) is a measure that compares the average signal power to the average power of the background noise. The noise can have different origins: it can be generated from the instrumental apparatus, from the detector or it can be linked with background sources or atmospherical effects. If the signal and the noise are both zero mean and their variances $\sigma_{S,N}^2$ are known, the SNR can be calculated as

$$\text{SNR} = \frac{P_S}{P_N} = \frac{\sigma_S^2}{\sigma_N^2} \ . \tag{3.11}$$

SNR sets the accuracy a measure can be done with. To be detected and confirmed, the data has to have a SNR above a certain threshold level. Low values of SNR mean that a signal has not been detected, while very high values imply a nearly certain detection. Figure 3.1 shows an example of SNR values for the detection of GWs.
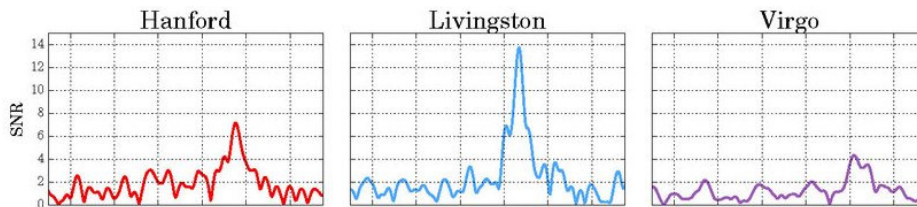
Figure 3.1: SNR of the interferometers LIGO Hanford, LIGO Livingston and VIRGO when the event GW170817 (see Sec. 1.2) was detected. Figure from [38].

3.2 Forecast techniques

In the scientific research, looking for new kinds of data and trying to have a better measurement of those already existing are fundamental tasks: new instruments (e.g. experiments, telescopes, satellites...) are steadily studied to involve their collection.

To plan the realization of one of them, its targets have to be defined: these include not only the kinds of observations it will do, but also the models it will test through the data it will get. It is important to understand before its realization what will be its capability in constraint models parameters: to do so, the Fisher matrix (Sec. 3.2.1) or the Monte Carlo methods (Sec. 3.2.3) can be used.

3.2.1   Fisher matrix

The Fisher matrix of a given future experiment predicts the minimum error it will commit in estimate a particular parameters set. It can be calculated only through the values of the measure uncertainties and the model that links parameters with data, even if they are still not gathered [70].

In fact, considering a parameter set $(\vartheta_1...\vartheta_N)$, the observables $(\mathcal{O}_1...\mathcal{O}_M)$ can be expressed as $\mathcal{O}_m(\vartheta_1, ..., \vartheta_N)$ with gaussian errors σ_m^2. The Fisher matrix can consequently be expressed as

$$F_{\alpha\beta} = \sum_{m=1}^{M} \frac{1}{\sigma_m^2} \frac{\partial \mathcal{O}_m}{\partial \vartheta_\alpha} \frac{\partial \mathcal{O}_m}{\partial \vartheta_\beta} \ . \tag{3.12}$$

In eq. (3.12), when the result of the derivation is still a function of the parameters, it is necessary to define a fiducial model to have their values a priori. The Fisher matrix obtained in this way is strictly dependent on them and it is valid only for models which parameter values are similar to the fiducial ones.

$F_{\alpha\beta}$ is linked to the Hessian $H_{\alpha\beta}$ defined in eq. (3.5) thanks to the ensemble average on the data [29], which gives

$$F_{\alpha\beta} = \langle H_{\alpha\beta} \rangle = \left\langle -\frac{\partial^2 \ln L}{\partial \theta_\alpha \partial \theta_\beta} \right\rangle = \left\langle \frac{\partial^2 \mathcal{L}}{\partial \theta_\alpha \partial \theta_\beta} \right\rangle \ . \tag{3.13}$$

When independent data sets are considered, the total likelihood is given by the product of the likelihoods of each set; for this reason, F_{TOT} for them is obtained summing the single Fisher matrices [68]. This can be useful for example when the values of some parameters $\vartheta_{\alpha,\beta}$ are already known (e.g. from previous observations) with a certain error $\sigma_{\text{prior } \alpha,\beta}^2$. In this case, to insert this information in the Fisher matrix, the matrix having $\sigma_{\text{prior } \alpha,\beta}^2$ on the diagonal has to be inverted and summed to F in order to get F_{TOT} (see [70] for details). In the same way, when data from different experiments can be combined to improve the parameter estimation, their Fisher matrices can be summed and the minimum uncertainty can be obtained from F_{TOT} (see [70] for examples).

Sometimes it is necessary to remove some parameters from the Fisher matrix, e.g. beacuse they are not of interest for the analysis (in this case they are called nuisance parameters). The marginalization process described in 3.1.1 has therfore to be performed: the probability of the parameter that has to be removed is integrated and the parameters becomes free to assume every value compatible with the others [70].

When the parameters are unbiased (see Sec. 3.1.1), the Cramér-Rao inequality can be derived. It assures [29] that

$$\Delta\vartheta_\alpha \geqslant \frac{1}{\sqrt{F_{\alpha\alpha}}} \ . \tag{3.14}$$

If the likelihood is Gaussianly distributed, the equality in eq. (3.14) is satisfied; on the other hand, when systematic errors or real effects are present, the uncertainty $\Delta\vartheta$ increases. The Cramér-Rao inequality places a lower limit on the errors that one can attain for the parameters estimation, regardless of the method used [29]. Usually, the error is higher than this: in the common case, the other parameters are estimated from the data as well and the minimum standard deviation is given by the marginal error defined in eq. (3.4) and linked to the Fisher matrix by $\Delta\vartheta_\alpha \geqslant \sqrt{(F^{-1})_{\alpha\alpha}}$ [3].

---

[3]$\Delta\vartheta_\alpha$ is the standard deviation of the errors σ_α as can be shown considering that $F = \langle H \rangle$.

3.2.2 Link between Fisher and Covariance

The Fisher matrix can be linked to the Covariance defined in eq. (3.5): in the case of future experiment forecasting, its diagonal elements are the minimum errors the parameters estimation will have, while the elements out of the diagonal give the correlation between different estimates. The correlation can be due not only to a physical link between the parameters but also to how they affect data: independent parameters can have similar effects and their estimates can therefore correlate [29].

Considering for example the case of a two parameters model, having Fisher matrix

$$F = \begin{pmatrix} a_{11} & a_{12} \\ a_{21} & a_{22} \end{pmatrix} \ , \tag{3.15}$$

where a_{11}, a_{22} are the estimation of the ϑ_1, ϑ_2 parameters, the Covariance matrix can be obtained as

$$F^{-1} = \frac{1}{\det F} \begin{pmatrix} c \circ f(a_{11}) & c \circ f(a_{12}) \\ c \circ f(a_{21}) & c \circ f(a_{22}) \end{pmatrix} = \begin{pmatrix} \sigma_1^2 & \sigma_{12}^2 \\ \sigma_{21}^2 & \sigma_2^2 \end{pmatrix} = C \ , \tag{3.16}$$

where $c \circ f(a_{\alpha\beta}) = (-1)^{\alpha+\beta} \det(F^{\alpha\beta})$ and $F^{\alpha\beta}$ is the submatrix obtained from F removing the α row and the β column. σ_1^2 and σ_2^2 are the minimum error obtainable for a_{11} and a_{12}, while $\sigma_{12} = \sigma_{21} = \rho\sigma_1\sigma_2$ is the correlation between them (ρ is called correlation parameter). Therefore, when the parameter ϑ_α has a high value $a_{\alpha\alpha}$ in the Fisher matrix, its error σ_α is small in the Covariance.

If F is obtained by summing other contributions, the Covariance matrix is obtained inverting the total one; if some parameters have to be marginalized, this can be done on the final Covariance matrix only if they are uncorrelated, otherwise the marginalization process has to be applied separately on the matrices of the single experiments.

Thanks to eq. (3.8), the Fisher matrix can be expressed as

$$\begin{aligned}
F_{\alpha\beta} &= \frac{1}{2}\mathrm{tr}\left[C^{-1}\frac{\partial C}{\partial\vartheta_\alpha}C^{-1}\frac{\partial C}{\partial\vartheta_\beta} + C^{-1}\left\langle\frac{\partial D}{\partial\vartheta_\alpha\partial\vartheta_\beta}\right\rangle \right] \\
&= \frac{1}{2}\mathrm{tr}\left[C^{-1}\frac{\partial C}{\partial\vartheta_\alpha}C^{-1}\frac{\partial C}{\partial\vartheta_\beta} + C^{-1}\left(\frac{\partial\mu}{\partial\vartheta_\alpha}\left(\frac{\partial\mu}{\partial\vartheta_\beta}\right)^T + \frac{\partial\mu}{\partial\vartheta_\beta}\left(\frac{\partial\mu}{\partial\vartheta_\alpha}\right)^T\right) \right] \ .
\end{aligned} \tag{3.17}$$

Confidence ellipses

The Covariance matrix of Gaussian distributions can be used to create the confidence regions: they are used to represent in the parameter space the compact intervals around the best fit values that contain a given percentage of the probability distribution [68]. This can be done when two parameters are studied; if there are more than two, all the others have to be marginalized [16].

As already mentioned in Sec. 3.2.1, the confidence regions are ellipses defined by $\chi^2 = \text{cost}$. They are defined by the $\sigma_{1,2}^2$ values obtained in eq. (3.16): their semi-axes a, b and inclination ι are

$$a^2 = \frac{\sigma_1^2 + \sigma_2^2}{2} + \sqrt{\frac{(\sigma_1^2 + \sigma_2^2)^2}{4} + \sigma_{12}^2} \tag{3.18}$$

$$b^2 = \frac{\sigma_1^2 + \sigma_2^2}{2} - \sqrt{\frac{(\sigma_1^2 + \sigma_2^2)^2}{4} + \sigma_{12}^2} \tag{3.19}$$

$$\mathrm{tg}(2\iota) = \frac{2\sigma_{12}}{\sigma_1^2 - \sigma_2^2} \tag{3.20}$$

As Figure 3.2 shows, the confidence ellipse is tilted when the parameter estimations correlate. Inside the ellipse, some confidence levels can be defined by multiplying its axes by the parameter $\alpha = \sqrt{\Delta\chi^2}$ [16]. The values commonly used are described in Tab. 3.1.

Confidence level		α
$1 - \sigma$	68.3%	1.52
$2 - \sigma$	95.4%	2.48
$3 - \sigma$	99.3%	3.44
	...	

Table 3.1: Definition of the confidence levels, data from [16].

The ellipse area is related with the merit function: it can be demonstrated (see [16] for details) that it is given by

$$
\begin{aligned}
A &= \pi(\alpha a)(\alpha b) \\
&= \pi\Delta\chi^2\left[\left(\frac{\sigma_1^2 + \sigma_2^2}{2}\right)^2 - \frac{(\sigma_1^2 + \sigma_2^2)^2}{4} + \sigma_{12}^2\right]^{1/2} \\
&= \pi\Delta\chi^2\left[\frac{1}{4}\sigma_1^4 + \frac{1}{4}\sigma_2^4 + \frac{1}{2}\sigma_1^2\sigma_2^2 - \frac{1}{4}\sigma_1^4 - \frac{1}{4}\sigma_2^4 + \frac{1}{2}\sigma_1^2\sigma_2^2 - \sigma_{12}^2\right]^{1/2} \\
&= \pi\Delta\chi^2(\sigma_1^2\sigma_2^2 - \sigma_{12}^2)^{1/2} \\
&= \pi\Delta\chi^2\sigma_1\sigma_2\sqrt{1 - \rho^2} \ .
\end{aligned}
\tag{3.21}
$$

3.2.3   Monte Carlo methods

To improve the statistical analysis and the forecasting of future experiments, simulations can be done. Several methods exist; however, among the most commonly used there are the Monte Carlo ones. They can be divided into Markov Chain Monte Carlo (MCMC) and Monte Carlo error estimations.

While MCMC simulate a series of point distributed as the likelihood function in order to map the posterior (see [29] for more detalis), Monte Carlo error estimations are used to simulate the different results that one observation can give. In fact (see [68] for more details), considering that the parameter ϑ has true value ϑ_0, from more than one observation different values of ϑ_i can be inferred. Each of them represents a different "Universe configuration" and their ensemble average would be $\langle\vartheta_i\rangle = \vartheta_0$; therefore, the distribution $\vartheta_i - \vartheta_0$ gives the estimation errors. However this distribution is not known: Monte Carlo error estimations consist in choosing a value $\bar{\vartheta}_0$ and simulate $\vartheta_i - \bar{\vartheta}_0$ instead. If this distribution is similar enough to the underlying one and the observational effects are mimicked quite well, this technique is extremely powerful and can map $\vartheta_i - \vartheta_0$, giving information about the value of ϑ_0 [68].

3.3   Angular Power Spectrum Fisher matrix

The Fisher matrix derived in Sec. 3.2.1 can be used to predict how well a future experiment will measure a certain APS: to do so, the model parameters ϑ_α are identified with the C_l values (see Sec. 2.2.2) and Gaussian fluctuations with average $\mu = 0$
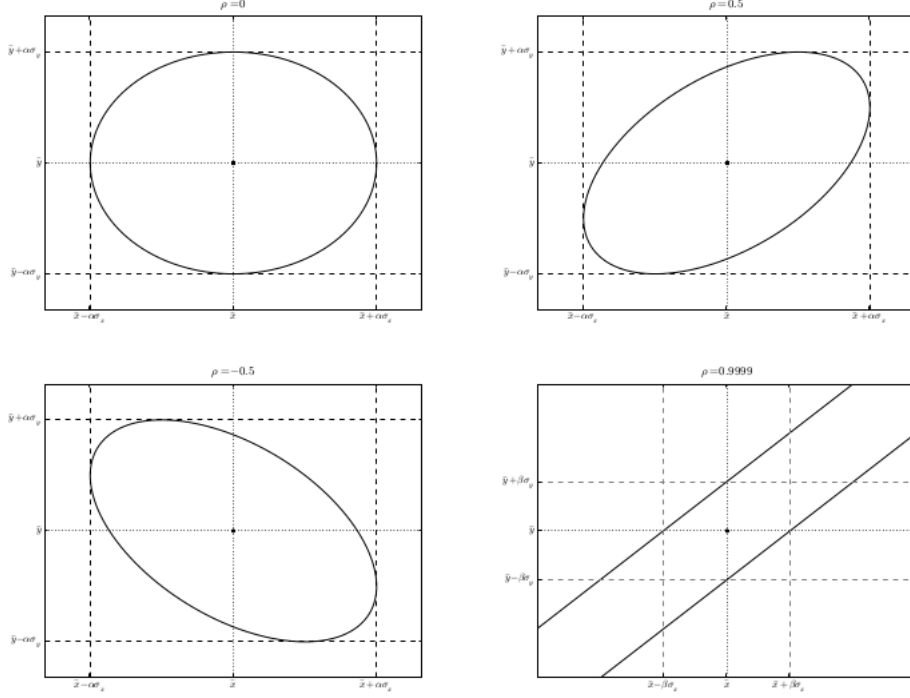
Figure 3.2: $1 - \sigma$ confidence ellipses for parameters x, y having uncertainties σ_x, σ_y and correlation coefficient ρ. The dash lines represent the marginalized uncertainty for each value, expressed by $\alpha\sigma_x$ and $\alpha\sigma_y$. Figure from [16].

are considered. Eq. (3.17) in this case can be reduced to

$$F_{\alpha\beta} = \frac{1}{2}\text{tr}\left[C^{-1}\frac{\partial C}{\partial\vartheta_\alpha}C^{-1}\frac{\partial C}{\partial\vartheta_\beta}\right] . \tag{3.22}$$

If the observations are done with beam size σ, the signal Covariance matrix can be calculated as $C_s = C_l\delta_{Dll'}\delta_{Dmm'}W = C_l\delta_{Dll'}\delta_{Dmm'}e^{-l^2\sigma^2}$ where $W = e^{-l^2\sigma^2}$ is the window function of the instrument used. On the other hand, the noise Covariance matrix is $N_l = \delta_{Dll'}\delta_{Dmm'}w^{-1}$ where $w = (\Delta\Omega\sigma_n^2)^{-1}$, $\Delta\Omega$ being the angular size of each pixel on the detector and σ_n its noise[4]. The total Covariance matrix results therefore (see [22] for details) made up by

$$C_{ll'mm'} = \delta_{Dll'}\delta_{Dmm'}\left[C_l e^{-l^2\sigma^2} + w^{-1}\right] . \tag{3.23}$$

Eq. (3.23) can be used to get

$$\begin{aligned}C_{ll'mm'}^{-1} &= \delta_{Dll'}\delta_{Dmm'}\left[C_l e^{-l^2\sigma^2} + w^{-1}\right]^{-1} \\ \frac{\partial C_{ll'mm'}}{\partial\vartheta_\alpha} &= \frac{\partial C_{ll'mm'}}{\partial C_\alpha} = \delta_{Dll'}\delta_{Dmm'}\delta_{Dl\alpha}e^{-l^2\sigma^2} ,\end{aligned} \tag{3.24}$$

---

[4]Particular attention has to be put in this Section on the notation. C_l indicates the APS coefficients, as defined in Sec. 2.2.2 and l is the multipole, linked to the angular scale of the fluctuations analyzed. $C_{ll'mm'}$ is otherwise the Covariance matrix as defined in Sec. 3.1.2 and its subscripts l, l', m, m' identify the pixel from which the signal and the noise are measured.

and this result can be inserted in (3.22) to get an explicit expression for the Fisher matrix. If the observations are realized all over the sky, C_l don't correlate one with the other and F is diagonal; it can be expressed as

$$
\begin{aligned}
F_{\alpha\beta} &= \frac{1}{2} \, C^{-1}_{ll'mm'} \frac{\partial C_{l'l''m'm''}}{\partial \vartheta_\alpha} C^{-1}_{l''l'''m''m'''} \frac{\partial C_{l'''lm'''m}}{\partial \vartheta_\beta} \\
&= \frac{1}{2} \frac{\delta_{Dll'}\delta_{Dmm'}}{C_l e^{-l^2\sigma^2} + w^{-1}} \left(\delta_{Dl'l''}\delta_{Dm'm''}\delta_{Dl'\alpha}e^{-l'^2\sigma^2}\right) \cdot \\
&\quad \cdot \frac{\delta_{Dl''l'''}\delta_{Dm''m'''}}{C_{l''} e^{-l''^2\sigma^2} + w^{-1}} \left(\delta_{Dl'''l}\delta_{Dm'''m}\delta_{Dl'''\beta}e^{-l'''^2\sigma^2}\right) \\
&= \frac{2\alpha+1}{2} \, \delta_{D\alpha\beta}e^{-2\alpha^2\sigma^2}\left[C_l e^{-\alpha^2\sigma^2} + w^{-1}\right]^{-2} ,
\end{aligned}
\tag{3.25}
$$

where the last two equalities are obtained applying the δ_D in order to transform (l, l') to (α, β) (see [22]) and to obtain

$$
\sum_m \sum_{m'm''m'''} \delta_{Dmm'}\delta_{Dm'm''}\delta_{Dm''m'''}\delta_{Dm'''m} = \sum_m \delta_{Dmm} = \frac{2l+1}{2} = \frac{2\alpha+1}{2} . \tag{3.26}
$$

For reasons of consistency with the previous and subsequent text, eq. (3.25) will be expressed as $F_{\alpha\beta} = (2l+1)/2\delta_{D\alpha\beta}e^{-2l^2\sigma^2}[C_l e^{-l^2\sigma^2} + w^{-1}]^{-2}$. The errors on C_l can therefore be calculated as

$$
\begin{aligned}
\delta C_l &= \sqrt{F^{-1}} = \sqrt{\frac{2}{2l+1}}e^{l^2\sigma^2}\left(C_l e^{-l^2\sigma^2} + w^{-1}\right) \\
&= \sqrt{\frac{2}{2l+1}}\left(C_l + w^{-1}e^{l^2\sigma^2}\right) ,
\end{aligned}
\tag{3.27}
$$

where $(2l+1)$ is the number of independent samplings used to measure each C_l, $w^{-1}e^{l^2\sigma^2}$ expresses the atmosferic and instrumental noise. The error due to the cosmic variance (see Sec. 2.2.2) is instead implicit in the C_l value. If the survey is sky limited and it covers only a fraction f_{sky}, eq. (3.27) includes this information and it is possible to show that (see [22])

$$
\delta C_l = \sqrt{\frac{2}{(2l+1)f_{sky}}}\left(C_l + w^{-1}e^{l^2\sigma^2}\right) . \tag{3.28}
$$

These values can be used to calculate the χ^2 function (see Sec. 3.1.2). It desrcibes the link between the model and the observation and it can therefore be expressed [22] also as

$$
\chi^2(\vartheta_\alpha) = \sum_l \frac{\left(C_l^{mod} - C_l^{obs}\right)^2}{\left(\delta C_l\right)^2} . \tag{3.29}
$$

Galaxy counts Fisher matrix

It is possible to study the case of a noiseless survey that covers all the sky. The APS signal is in this case given by the spherical harmonics (see Sec. 2.2.2), while the coefficients are $s_l = (a_l^1, a_l^2...)$, where $1, 2...$ identifies the observables.

For a survey as the one described in Chapter 4, whose aim is to study the projected 2D APS of the fluctuations in the matter (in particular in NS-NS binaries) distribution,

the coefficient expresses respectively the number counts C and the lensing fluctuations L for each redshift bin that is observed (see Chapter 4). If x, y are the combinations between them (e.g $x, y =$ CC, CL, LC, LL), the Fisher matrix can be obtained similarly to what [22] and [68] do in the CMB APS analysis, and it results

$$F_{\alpha\beta} = \sum_{xy} \sum_l \frac{\partial C_l^x}{\partial \vartheta_\alpha} \left(\mathcal{C}_l^{xy}\right)^{-1} \frac{\partial C_l^y}{\partial \vartheta_\beta} \quad \text{where } (\mathcal{C}_l^{xy})^{-1} = (C_l^x)^{-1}(C_l^y)^{-1} . \quad (3.30)$$

The Covariance matrix can be explicitly written as

$$C = \begin{pmatrix} C_l^{CC} & C_l^{CL} \\ C_l^{CL} & C_l^{LL} \end{pmatrix}$$
$$\mathcal{C}_l = \frac{2}{2l+1} \begin{pmatrix} (C_l^{CC})^2 & (C_l^{CL})^2 & C_l^{CC} C_l^{CL} \\ (C_l^{CL})^2 & (C_l^{LL})^2 & C_l^{LL} C_l^{CL} \\ C_l^{CC} C_l^{CL} & C_l^{LL} C_l^{CL} & \frac{1}{2}[(C_l^{CL})^2 + C_l^{CC} C_l^{LL}] \end{pmatrix} , \quad (3.31)$$

where it is clear that the two parameter estimations correlate.

These results (for the Fisher matrix in general and for the APS one) will be necessary in Chapter 4 to compute the Fisher matrix in the particular case studied. The target is to forecast the errors that future GW observatories, such as ET, will committ in estimating Cosmological parameters from GW measurements.

Chapter 4

Can standard sirens be used without redshift?

This Chapter describes one possible application of GWs in Cosmological studies. It is based on the work of Namikawa, Nishizawa and Taruya [47] and it focuses on the use of GWs as standard sirens without redshift information. The problem presented (Sec. 4.1) has been faced both with a theoretical (Sec. 4.2) and a numerical (Sec. 4.4) approach. It represents the first step of a wider study that will be developed in the future (Sec. 4.5).

4.1   Standard sirens without redshift information

The authors of [47] propose a statistic method to use GWs as standard sirens even if there is no redshift information, without assuming too binding conditions a priori. The study is carried out with the forecasting of future interferometers, in particular ET (see Sec. 1.3.1).

The GW events considered here are due to the merging of NS-NS binaries. The main task is to compare their observed luminosity distance distribution with the theoretical one. If no redshift is available, the latter can be obtained studying the anisotropies due both to the weak lensing and to the NS clustering caused by the gravitational potential fluctuations (see Chapter 2).

If other kinds of binary systems were studied (e.g. NS-BH or BH-BH), the approch to the problem would be the same. Some quantities, such as the merging rate and the bias, would change. As described in Sec. 1.2, the distance up to which measurements can be done depends on the bodies componing the binary: the more massive they are, the higher the amplitude of the GWs is and the farther they can be observed.

4.2   Theoretical approach

In this Section, the analysis performed in [47] is reported and deepened. Firstly, an estimator to measure the anisotropies in the NS-NS merging distribution is defined (Sec. 4.2.1). It is then linked to the other observables (Sec. 4.2.2), in particular to the matter and lensing APS. These can be used to construct the auto and cross APS of the estimator in different luminosity distance bins (Sec. 4.2.3).

4.2.1 The anisotropy estimator

The NS-NS binary systems distribution[1] can be defined as $N(D_L, \Omega) = N(x)$, depending on the luminosity distance D_L and the observation direction Ω. This is an all sky Poissonian distribution, over which fluctuations due to clustering and lensing effects overlap. The distribution function can be normalized dividing $N(x)$ for the total number of binaries visible in each direction, i.e. integrated by D_L. The normalized distribution therefore is

$$p(x) = \frac{N(x)}{\int N(x)\, dD_L} \ . \tag{4.1}$$

An anisotropy estimator has to be built in order to study the fluctuations and their physical properties. The first step to take is to divide the NS-NS binaries in i luminosity distance intervals, each of them defined by $D_{Li} \in [D_{Li}^{min}, D_{Li}^{max}]$. Each of the observed D_L belongs to one interval and it differs from the its average $\overline{D}_L$ for two main reasons:

- in each direction Ω, the NS-NS binaries are clustered and this creates fluctuations in $N(x)$;

- the observed D_L is affected by the gravitational lensing. In particular, the convergence $\mathsf{k}(\overline{x}) = \mathsf{k}(\overline{D}_L, \Omega)$ (see Sec. 2.2.3) induces a magnification effect on the observable $D_L(x) = \overline{D}_L\big(1 + \mathsf{k}(\overline{x})\big)$. Second order effects, such as the shift of the source positions due to the GW trajectory deviation, are not considered.

The average $\overline{D}_L$ can be calculated for each bin and each Ω direction as

$$\hat{d}_i(\Omega) = \int_{D_{Li}^{min}}^{D_{Li}^{max}} D_L p(x)\, dD_L \ , \tag{4.2}$$

and, averaging all over the sky

$$\hat{d}_i = \int_{4\pi} \hat{d}_i(\Omega)\, d\Omega \ . \tag{4.3}$$

To study the anisotropies in each luminosity distance bin, the estimator can be defined as

$$\hat{s}_i(\Omega) = \frac{\hat{d}_i(\Omega) - \hat{d}_i}{\hat{d}_i} \ . \tag{4.4}$$

Physically, this means that in each direction Ω and in each bin $[D_{Li}^{min}, D_{Li}^{max}]$ NS-NS binaries can be found and their positions fluctuate with respect to the typical luminosity distance of the bin $\hat{d}_i$. The estimator $\hat{s}_i$ represents the normalized distance between this one and the observed average position $\hat{d}_i(\Omega)$.

$\hat{s}_i(\Omega)$ is proportional both to the intrinsic number density of the NS-NS systems $\delta(\overline{x})$ and to the fluctuations due to the lensing convergence k.

4.2.2 Link between different observables

The main observable is the distribution $p(D_L, \Omega)d\Omega dD_L$, whose fluctuations are due both to the clustering $\delta(\overline{x})$ and the lensing. Their effect can be described as

$$p(D_L, \Omega)d\Omega dD_L = \overline{p}(\overline{D}_L)\big[1 + \delta(\overline{x})\big]d\Omega d\overline{D}_L \ , \tag{4.5}$$

---

[1]When talking about the NS-NS binaries distribution, it is always subtexted that these systems merged and emmitted GWs.

where $p(D_L, \Omega)$ is the lensed distribution and $\bar{p}(\overline{D}_L, \Omega)$ the non lensed one. In particular, $D_L = \overline{D}_L(1 + k(\bar{x}))$. Possible fluctuations from the average direction $\overline{\Omega}$ are not considered here; for this reason, the Ω dependence in $\bar{p}(\overline{D}_L, \Omega) = \bar{p}(\overline{D}_L)$ can be omitted.

The dimensionless quantity $n(x) = D_L p(x)$ can be defined. It can be calculated as

$$
\begin{aligned}
n(x) &= D_L \ p(x) \\
&= D_L \ \bar{p}(\overline{D}_L) \big[1 + \delta(\bar{x})\big] d\Omega \ d\overline{D}_L \frac{1}{d\Omega} \frac{1}{dD_L} \\
&= D_L \ \frac{\overline{n}(\overline{D}_L)}{\overline{D}_L} \big[1 + \delta(\bar{x})\big] \frac{d\overline{D}_L}{dD_L} \\
&= \overline{n}(\overline{D}_L) \big[1 + \delta(\bar{x})\big] \big(1 + k(\bar{x})\big) \frac{d\overline{D}_L}{dD_L} \ ,
\end{aligned}
\tag{4.6}
$$

where the relation between lensed D_L and non lensed $\overline{D}_L$ has been used. Calculating $\overline{D}_L / dD_L$ as

$$
\frac{d\overline{D}_L}{dD_L} = \frac{d}{dD_L} \left(\frac{D_L}{1 + k(x)} \right) = \frac{1 + k - D_L k'}{[1 + k]^2} \ .
\tag{4.7}
$$

and neglecting the second order perturbations by removing the "above bars", it is possible to get

$$
n(x) \simeq \overline{n} \left(\frac{D_L}{1 + k(x)} \right) \big[1 + \delta(x)\big] \big(1 + k(x)\big) \frac{1 + k(x) - D_L k'(x)}{\big(1 + k(x)\big)^2} \ ,
$$

where $k' = dk/dD_L$. Using the Taylor expansion

$$
\frac{1 + k - D_L k'}{1 + k} = 1 - \frac{D_L k'}{1 + k} \simeq 1 - D_L k'(1 - k) \ ,
\tag{4.8}
$$

and neglecting the second order fluctuations, eq. (4.6) becomes

$$
\begin{aligned}
n(x) &\simeq \overline{n} \left(\frac{D_L}{1 + k(x)} \right) \big[1 + \delta(x)\big] \big[1 - D_L k'(x) \big(1 - k(x)\big)\big] \\
&\simeq \overline{n} \left(\frac{D_L}{1 + k(x)} \right) \big[1 + \delta(x)\big] \big[1 - D_L k'(x)\big] \ .
\end{aligned}
\tag{4.9}
$$

Therefore the observed average position at linear order can be defined as

$$
\begin{aligned}
\hat{d}_i(\Omega) &= \int_{D_{Li}^{min}}^{D_{Li}^{max}} D_L p(x) \, dD_L = \int_{D_{Li}^{min}}^{D_{Li}^{max}} n(x) \, dD_L \\
&\simeq \int_{D_{Li}^{min}}^{D_{Li}^{max}} \overline{n} \left(\frac{D_L}{1 + k(x)} \right) \big[1 + \delta(x)\big] \big[1 - D_L k'(x)\big] \, dD_L \\
&\simeq \int_{D_{Li}^{min}}^{D_{Li}^{max}} \overline{n} \left(\frac{D_L}{1 + k(x)} \right) \big[1 + \delta(x) - D_L k'(x)\big] \, dD_L \ ,
\end{aligned}
\tag{4.10}
$$

Thanks to the Ω average, in each luminosity distance bin it is possible to define

$$
\begin{aligned}
\hat{d}_i = &\int_{D_{Li}^{min}}^{D_{Li}^{max}} \int_{4\pi} \overline{n} \left(\frac{D_L}{1 + k(x)} \right) d\Omega \, dD_L + \int_{D_{Li}^{min}}^{D_{Li}^{max}} \int_{4\pi} \delta(x) \overline{n} \left(\frac{D_L}{1 + k(x)} \right) d\Omega \, dD_L + \\
&- \int_{D_{Li}^{min}}^{D_{Li}^{max}} \int_{4\pi} D_L k'(x) \overline{n} \left(\frac{D_L}{1 + k(x)} \right) d\Omega \, dD_L = \overline{d}_i.
\end{aligned}
\tag{4.11}
$$

Integrating in $d\Omega$ at the linear order it is possible to have that

- $\overline{n}\left(\frac{D_L}{1+\mathsf{k}(x)}\right)$ loses the k dependence thanks to the average of the Taylor expansion;

- $\int_{4\pi} \delta(x)\, d\Omega = 0$ thanks to the fluctuations average;

- $\int_{4\pi} \mathsf{k}(x)\, d\Omega = \int_{4\pi} \mathsf{k}'(x)\, d\Omega = 0$ thanks to the fluctuations average.

Therefore, eq. (4.11) becomes $\overline{d}_i = \int_{D_{Li}^{min}}^{D_{Li}^{max}} \overline{n}(D_L)\, dD_L$ and $\overline{d}_i$ can be used to express $\hat{d}_i(\Omega)$. To do so, it is necessary to define

$$\gamma(D_L) = 1 + D_L\left[\delta_D(D_L - D_{Li}^{min}) - \delta_D(D_L - D_{Li}^{max})\right] . \tag{4.12}$$

This factor applicates the convergence effect only on D_{Li}^{min} and D_{Li}^{max}: this is due to the assumption of neglecting lensing second order effects, such as the deviation of the GW trajectories. In eq. (4.10) $\mathsf{k}(x)$ can be averaged over all the sky; assuming $\overline{D}_L \simeq D_L$, the value of $\hat{d}_i(\Omega)$ can be calculated as

$$
\begin{aligned}
\hat{d}_i(\Omega) &\simeq \int_{D_{Li}^{min}}^{D_{Li}^{max}} \overline{n}\left(\frac{D_L}{1+\mathsf{k}(x)}\right)\left[\delta(x) - D_L\mathsf{k}'(x)\right] dD_L + \int_{D_{Li}^{min}}^{D_{Li}^{max}} \overline{n}\left(\frac{D_L}{1+\mathsf{k}(x)}\right) dD_L \\
&\simeq \int_{D_{Li}^{min}}^{D_{Li}^{max}} \overline{n}(D_L)\left[1 + \delta(x) + \mathsf{k}(x)\big(1 + D_L(D_{Li}^{min} - D_{Li}^{max})\big)\right] dD_L ,
\end{aligned}
\tag{4.13}
$$

where at the linear order $D_L\mathsf{k}' \simeq D_L\Delta\mathsf{k}/\Delta D_L \simeq \mathsf{k}(1 - D_L\Delta D_L)$.

Therefore $\hat{d}_i(\Omega) \simeq \overline{d}_i + \int_{D_{Li}^{min}}^{D_{Li}^{max}} \overline{n}(D_L)\left[\delta(x) + \gamma(D_L)\mathsf{k}(x)\right] dD_L$ and, thanks to these definitions, the anisotropy estimator can be derived as

$$
\begin{aligned}
\hat{s}_i(\Omega) &= \frac{\hat{d}_i(\Omega) - \overline{d}_i}{\overline{d}_i} \\
&= \frac{\overline{d}_i + \int_{D_{Li}^{min}}^{D_{Li}^{max}} \overline{n}(D_L)\left[\delta(x) + \gamma(D_L)\mathsf{k}(x)\right] dD_L - \overline{d}_i}{\overline{d}_i} \\
&= \frac{1}{\overline{d}_i} \int_{D_{Li}^{min}}^{D_{Li}^{max}} \overline{n}(D_L)\left[\delta(x) + \gamma(D_L)\mathsf{k}(x)\right] dD_L .
\end{aligned}
\tag{4.14}
$$

4.2.3 Anisotropies APS

The estimator defined in eq. (4.14) can be used to infer Cosmological information. To do so, as [47] explains, it is necessary to define the auto and cross APS for all the distance luminosity bins. In each of them, $\hat{s}_i(\Omega)$ can be decomposed in the harmonic space using the coefficients $\hat{s}_{i,lm}$: they represent the spherical harmonics (see Sec. 2.2.2) linked to the angle values ($\Omega = (\theta, \phi)$). For each couple of bins (i, j) it is indeed possible to define operatively

$$\hat{C}_l^{s_i s_j} = \frac{1}{2(2l+1)} \sum_{m=-l}^{l} \left(\hat{s}_{i,lm}\hat{s}_{j,lm}^* + \mathsf{c.c.}\right) . \tag{4.15}$$

If the angular part of δ and k are decomposed into harmonic coefficents δ_{lm}, k_{lm}, eq. (4.14) can be expressed as

$$\hat{s}_i = \sum_l \sum_m \frac{1}{\bar{d}_i} \int dD_L \ \bar{n}(D_L) \big[\delta_{lm}(x) + \gamma(D_L) k_{lm}(x) \big] \ . \tag{4.16}$$

It is therefore possible to define $C_l^{s_i s_j}$ using the ensemble average over (i,j) in order to get

$$
\begin{aligned}
C_l^{s_i s_j} &= \int \frac{dD_{L1}}{\bar{d}_i} \int \frac{dD_{L2}}{\bar{d}_j} \ \bar{n}(D_{L1}) \ \bar{n}(D_{L2}) \cdot \\
&\quad \cdot \big[\delta_{1,lm}^* + \gamma(D_{L1}) k_{1,lm}^* \big] \big[\delta_{2,lm} + \gamma(D_{L2}) k_{2,lm}^* \big] + \text{c.c.} \\
&= \int \frac{dD_{L1}}{\bar{d}_i} \int \frac{dD_{L2}}{\bar{d}_j} \ \bar{n}(D_{L1}) \ \bar{n}(D_{L2}) \cdot \\
&\quad \cdot \big\{ C_l^{\delta_1 \delta_2} + \gamma(D_{L1}) \gamma(D_{L2}) C_l^{k_1 k_2} + \gamma(D_{L1}) C_l^{\delta_2 k_1} + \gamma(D_{L2}) C_l^{\delta_1 k_2} \big\} \ ,
\end{aligned}
\tag{4.17}
$$

where $D_{Li,j}$ is the luminosity distance in the two bins $[D_{Li,j}^{min}, D_{Li,j}^{max}]$, $\bar{d}_{i,j}$ is the average luminosity distance, $\bar{n}(D_{L1,2})$ and $\gamma(D_{L1,2})$ have been defined in Sec. 4.2.2. $C_l^{\delta_1, \delta_2}$ and $C_l^{k_1, k_2}$ are the auto APS respectively of the matter fluctuations δ and of the lensing convergence k; $C_l^{\delta_1, k_2}$ and $C_l^{k_1, \delta_2}$ are the cross angular power spectrum. They satisfy the properties

$$
\begin{aligned}
< \delta_{lm}(D_{L1}) k_{lm}^*(D_{L2}) > &= \delta_{ll'} \delta_{mm'} C_l^{\delta_1, k_2} \ , \\
< \delta_{lm}(D_{L1}) \delta_{lm}^*(D_{L2}) > &= \delta_{ll'} \delta_{mm'} C_l^{\delta_1, \delta_2} \ , \\
< k_{lm}(D_{L1}) k_{lm}^*(D_{L2}) > &= \delta_{ll'} \delta_{mm'} C_l^{k_1, k_2} \ .
\end{aligned}
\tag{4.18}
$$

The authors of [47] analyze the matter and lensing auto APS in the luminosity distance intervals $[0, 6.6]$ Gpc, $[10, 14]$ Gpc and $[21, 45]$ Gpc (i.e. redshift intervals $[0, 1]$, $[1.4, 1.9]$ and $[2.6, 4.9]$): they have been chosen considering that a three years observation survey with ET would observe inside each of them an equal number of binary sources. Figure 4.1 shows their results.

The correlation in the auto APS is dominated by the clustering; on the other hand, in the cross PS between distant bins it would be the lensing that dominates.

The matter cross APS $C_l^{\delta_1 \delta_2}$ can be obtained by the product between the C_l calculated in eq. (2.43) for two bins; when it is expressed as a function of the redshift z, it results to be (see [31] and [48])

$$
\begin{aligned}
C_l^{\delta_1 \delta_2} &= \frac{2}{\pi} \int dk k^2 P(k) \frac{1}{N^2} \int_{z_{min}^{(1)}}^{z_{max}^{(1)}} dz \frac{dN}{dz}(z) b^{(1)}(z) j_l \big(k D_c^{(1)} \big) \cdot \\
&\quad \cdot \int_{z_{min}^{(2)}}^{z_{max}^{(2)}} dz \frac{dN}{dz}(z) b^{(2)}(z) j_l \big(k D_c^{(2)} \big) \ ,
\end{aligned}
\tag{4.19}
$$

where $P(k)$ is obtained combining the primordial PS with the Transfer and Growth function (see Sec. 2.2.1), N is the sources distribution, $b^{(1)}$ and $b^{(2)}$ are the bias in the two bins $[z_{min}^{(1)}, z_{max}^{(1)}]$, $[z_{min}^{(2)}, z_{max}^{(2)}]$ and dN/dz is the selection function.
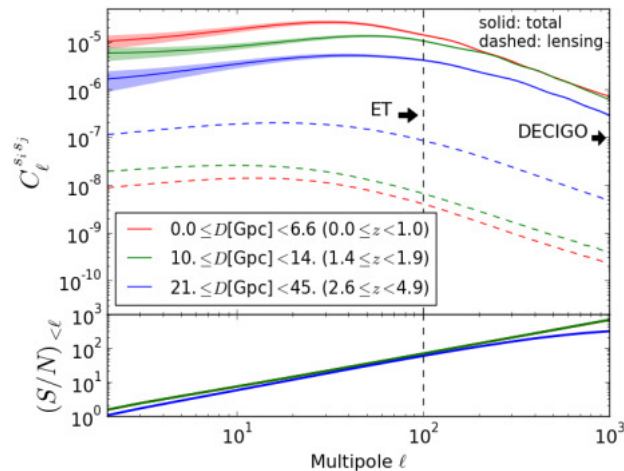
Figure 4.1: The upper image represents the auto APS for $C_l^{s_i s_j}$ described in eq. (4.17) (solid lines) and for the lensing C_l^{kk} (dashed lines), with expected $1 - \sigma$ statistical errors. A three years observation survey with ET is assumed; in this way, the luminosity distance bins contain an equal number of NS-NS sources. The lower image represents the cumulative SNR of the LSS induced anisotropies. Image from [47].

4.3 Fisher matrix

The anisotropy estimator defined in Sec. 4.2.2 and 4.2.3 have to be provided with the error bars; these are defined thanks to the propagation of the errors of the observables. First of all, the luminosity distance error can be defined as

$$\epsilon = \frac{\delta D_L}{D_L} \ , \tag{4.20}$$

in order to get $D_L = \overline{D}_L(1+\epsilon)$. The value of ϵ depends both on the detector sensibility and on the distance of the source itself. It is instead independent from the angular position of the source and from LSS: this means that it does not depend on the clustering and lensing effects. The ϵ error is assumed to be Gaussian distributed with zero mean.

As Chapter 3 described, the Fisher matrix can be used to predict the ϵ for future experiments. To derive it, in this work it is assumed that

- the GW sources are uncorrelated;

- the GW is described by a restricted 1.5 post-Newtonian wavefront (see Sec. 1.3.2);

- the merging objects that emit the GWs have zero spin.

The Fisher matrix is strictly connected with the telescope that is assumed to be used; in [47] the ET telescope (see Sec. 1.3.1) is considered. In this work the matrix is calculated only theoretically and for this reason the telescope has not been specified.

The Fisher matrix has been derived using the same approach as the one described in [51]. The GW emitting system is a NS-NS binary in the merging phase. It is

assumed to be located at z redshift, where the Hubble parameter value (see Sec. 2.1) is $H(z)$; the Universe is assumed to be spatially flat.

The model parameters are (see Sec. 1.3.2 and 2.1) the redshift chirp mass M_z, the symmetric mass ratio η, the time and phase at the coalescence t_c and ϕ_c, the luminosity distance $D_L(z)$ and the Universe expansion parameter $X(z)$. They are used to describe the wavefront: it has been defined in eq. (1.69) as

$$\tilde{h}(f) = \frac{A}{D_L(z)} M_z^{5/6} f^{-7/6} e^{i\Phi(f)} , \qquad (4.21)$$

where f is the frequency, while

$$A = (\sqrt{6}\pi^{2/3})^{-1}$$

$$\Phi = 2\pi f t_c - \phi_c - \frac{\pi}{4} + \frac{3}{128}(\pi M_z f)^{-5/3}\left[1 + \frac{20}{9}\left(\frac{743}{336} + \frac{11}{4}\eta\right)\eta^{-2/5}(\pi M_z f)^{2/3} + \right.$$

$$\left. - 16\pi\eta^{-3/5}(\pi M_z f) - \frac{25}{768}X(z)M_z(\pi M_z f)^{-8/3}\right] .$$

$$(4.22)$$

The coefficient A is a geometrical factor, due to the average inclination of the NS-NS binaries, while Φ depends on $\pi M_z f$, therefore it is linked with the redshift (see Sec. 1.3.2).

The authors of [51] calculate the Fisher matrix for the DECIGO telescope, made by 8 interferometers; for one GW source, they obtain

$$F_{\alpha\beta} = 4\sum_{i=1}^{8} Re \int_{f_{min}}^{f_{max}} \frac{1}{S_h(f)} \frac{\partial \tilde{h}^*(f)}{\partial\alpha} \frac{\partial \tilde{h}(f)}{\partial\beta} df , \qquad (4.23)$$

where $\tilde{h}^*(f)$ is the complex conjugate of the $h(f)$ quantity defined in eq. (1.69). $S_h(f)$ is due to the measurement uncertainties. It can be decomposed into the interferometer noise curve S_h^{inst} and S_h^{WD}, the confusion noise due to the low frequencies contribution of the WD[2]. The cut off frequencies f_{min} and f_{max} depend respectively the first on the trend of the noise curve, the second on the time of the observation, on z and M_{chirp}. In the ET case, the summation in eq. (4.23) has to be performed using the index $i = 1...6$, because the telescope is made of 3 interferometer couples.

The luminosity distance error can be split into $\sigma_{D_L}^2(z) = \sigma_{inst}^2 + \sigma_{lens}^2 + \sigma_{pv}^2$. σ_{inst}^2 is the instrumental error, σ_{lens}^2 is the error due to the lensing magnification on the LoS, σ_{pv}^2 is the error caused by the Doppler effect of the sources peculiar velocities. The assumptions previously described imply that σ_{lens}^2, $\sigma_{pv}^2 = 0$ and $\sigma_{D_L}^2 = \sigma_{str}^2 = \epsilon^2$.

Except for D_L, all the parameters are marginalized (see Sec. 3.1.1): the minimum error on D_L can be therefore calculated as $\epsilon = \sqrt{(F^{-1})_{D_L D_L}} = (\sqrt{F_{D_L D_L}})^{-1}$. Using the model defined in eq. (1.69), it follows that

$$\tilde{h}(f) = \frac{A}{D_L(z)} M_z^{5/6} f^{-7/6} e^{i\Phi(f)} ; \quad \tilde{h}^*(f) = \frac{A}{D_L(z)} M_z^{5/6} f^{-7/6} e^{-i\Phi(f)}$$

$$\frac{\partial \tilde{h}(f)}{\partial D_L} = -\frac{A}{D_L^2(z)} M_z^{5/6} f^{-7/6} e^{i\Phi(f)} ; \quad \frac{\partial \tilde{h}^*(f)}{\partial D_L} = -\frac{A}{D_L^2(z)} M_z^{5/6} f^{-7/6} e^{-i\Phi(f)} .$$

---

[2]In [51] the contribution $S_h^{NS}\mathcal{R}^{NS}$ is also considered. It is the error propagation due to the subtraction of the NS-NS GW contribution to the signal, in order to obtain the stochastic background (see e.g. [14]. This process is not executed in this work, so the $S_h^{NS}\mathcal{R}^{NS}$ contribution has not to be taken into account.

Therefore, it follows that

$$F_{D_L D_L} = \int_{f_{min}}^{f_{max}} \frac{1}{S_h(f)} \frac{A^2}{D_L^4(z)} M_z^{5/3} f^{-7/3} \, df$$

$$\epsilon = \left[\frac{D_L^4(z)}{A^2} M_z^{-5/3} \left(\int_{f_{min}}^{f_{max}} \frac{1}{S_h(f)} f^{-7/3} \, df \right)^{-1} \right]^{1/2} .$$

(4.24)

Error propagation

The ϵ value propagates into the estimator error. In particular, the error associated to $\hat{d}_i(\Omega)$ (see Sec. 4.2.2) is

$$\delta\hat{d}_i(\Omega) = \int_{D_{Li}^{min}}^{D_{Li}^{max}} \delta\overline{n}(\overline{D}_L) \, dD_L = \int_{D_{Li}^{min}}^{D_{Li}^{max}} \left(\overline{n}(D_L) - \overline{n}(\overline{D}_L) \right) dD_L$$

$$= \int_{D_{Li}^{min}}^{D_{Li}^{max}} \left(\overline{n}(D_L) - \overline{n}\left(\frac{D_L}{1+\epsilon} \right) \right) dD_L$$

(4.25)

$$\simeq \int_{D_{Li}^{min}}^{D_{Li}^{max}} \left(\overline{n}'(D_L) D_L \epsilon + O(\epsilon^2) \right) dD_L$$

where the last equality is obtainted considering that $\overline{n}'(D_L) = d\overline{n}/dD_L$ and

$$\overline{n}'(D_L) \simeq \frac{\Delta\overline{n}}{\Delta D_L} = \frac{\overline{n}(D_L) - \overline{n}(\overline{D}_L)}{D_L - D_L/(1+\epsilon)} = \frac{\left[\overline{n}(D_L) - \overline{n}(\overline{D}_L)\right](1+\epsilon)}{\epsilon D_L} ,$$

(4.26)

therefore

$$\overline{n}(D_L) - \overline{n}(\overline{D}_L) = \overline{n}(D_L) - \overline{n}\left(\frac{D_L}{1+\epsilon} \right)$$

$$\simeq \overline{n}(D_L) - \overline{n}(D_L(1-\epsilon))$$

$$\simeq \overline{n}(D_L) - \left(\overline{n}(D_L) + \frac{\partial\overline{n}(\epsilon D_L)}{\partial D_L} + O(\epsilon^2) \right)$$

(4.27)

$$\simeq \frac{\overline{n}'\epsilon D_L}{1+\epsilon} \simeq \overline{n}'\epsilon D_L(1-\epsilon)$$

$$\simeq \overline{n}'\epsilon D_L + O(\epsilon^2) .$$

Consequently, in each bin the average luminosity distance $\hat{d}_i$ error is of the order of $O(\epsilon^2)$; for this reason, it can be neglected assuming that the average distance estimated from the data is at the linear order equal to the average distance of the sources, i.e. $\hat{d}_i = \overline{d}_i$. Finally, the error related to the anisotropy estimator $\hat{s}_i(\Omega)$ (see eq. (4.14)) is

$$\delta\hat{s}_i = \frac{\delta\hat{d}_i(\Omega)}{\overline{d}_i} = \frac{1}{\overline{d}_i} \int_{D_{Li}^{min}}^{D_{Li}^{max}} \overline{n}'(D_L) D_L \epsilon \, dD_L .$$

(4.28)

The $\hat{s}_i(\Omega)$ estimator is used to get the APS $\hat{C}_l^{s_i s_j}$ and its ensamble value $C_l^{s_i s_j}$ as defined in Sec. 4.2.3. The error of the first one can be obtained through the

propagation of $\delta \hat{s}_i$ and result to be

$$
\begin{aligned}
\delta \hat{C}_l^{s_i s_j} &= \frac{1}{2(2l+1)} \sum_{m=-l}^{l} (\delta \hat{s}_{lm}^i \delta \hat{s}_{lm}^{j*} + \delta \hat{s}_{lm}^j \delta \hat{s}_{lm}^{i*}) \\
&= \frac{1}{2(2l+1)} \cdot 2(2l+1)\delta_{ij} \frac{1}{\overline{d}_i^2} \int_{D_{Li}^{min}}^{D_{Li}^{max}} \overline{n}'^2(D_L) D_L^2 \epsilon^2 \, dD_L \qquad (4.29) \\
&= \delta_{ij} \frac{1}{\overline{d}_i^2} \int_{D_{Li}^{min}}^{D_{Li}^{max}} \overline{n}'^2(D_L) D_L^2 \epsilon^2 \, dD_L \ .
\end{aligned}
$$

Considering that $\overline{p}(D_L) = \overline{p}(x) = N_i(x)/\int N_i(x)\,dD_L$, in each region ϵ can be related to its root mean square $\sigma^2(D_L)$. In this way, eq. (4.29) can be ensemble averaged, in order to get

$$
\begin{aligned}
\langle \delta \hat{C}_l^{s_i s_j} \rangle &= \delta_{ij} \frac{1}{\overline{d}_i^2} \int_{D_{Li}^{min}}^{D_{Li}^{max}} \overline{n}'^2(D_L) D_L^2 \sigma^2(D_L)\,dD_L \ \frac{1}{\int N_i(x)\,dD_L} \\
&= \delta_{ij} \frac{1}{\overline{d}_i^2} \int_{D_{Li}^{min}}^{D_{Li}^{max}} \overline{n}'^2(D_L) D_L^2 \sigma^2(D_L) \frac{N_i(x)}{\overline{p}(D_L)}\,dD_L \ .
\end{aligned}
\qquad (4.30)
$$

In each bin it is possible to define

$$
\sigma_i^2 = \frac{1}{\overline{d}_i^2} \int_{D_{Li}^{min}}^{D_{Li}^{max}} \overline{p}(D_L) \left[\frac{\overline{n}'(D_L)}{\overline{p}(D_L)} \right]^2 (D_L) D_L^2 \sigma^2(D_L)\,dD_L \ . \qquad (4.31)
$$

If eq. (4.30) is rewritten as $\langle \delta \hat{C}_l^{s_i s_j} \rangle = \delta_{ij}(\sigma_i^2/N_i)$, the PS can be expressed as $\langle \hat{C}_l^{s_i s_j} \rangle' = \langle \hat{C}_l^{s_i s_j} \rangle + \langle \delta \hat{C}_l^{s_i s_j} \rangle = C_l^{s_i s_j} + \delta_{ij}(\sigma_i^2/N_i)$. The last equation shows a systematic[3] offset with respect to the original PS; the uncertainty that has been obtained is different from zero even if the average value is subtracted to the PS.

SNR

The SNR can be calculated if the signal S and the noise N powers are measured for each bin. The first one is simply $\mathsf{S} = C_l^{s_i s_i}$, while the second one combines the PS offset with the cosmic variance $\Delta C_l / C_l$ (see Sec. 2.2.2). It can be derived

$$
\mathsf{N} = \frac{\Delta C_l}{C_l} \cdot \left[C_l^{s_i s_i} + (\sigma_i^2/N_i) \right] = \sqrt{\frac{2}{2l+1}} \left[C_l^{s_i s_i} + (\sigma_i^2/N_i) \right] \ . \qquad (4.32)
$$

The SNR of the anisotropy estimator $\hat{s}_{i,lm}$ in the ith bin is calculated as $(\mathsf{S}/\mathsf{N})_i$; the cumulative SNR for $\hat{s}_i$ consequently results to be

$$
\left(\frac{\mathsf{S}}{\mathsf{N}} \right)_{<l}^2 = \sum_l \left(\frac{\mathsf{S}}{\mathsf{N}} \right)_i^2 = \sum_l \frac{2l+1}{2} \left[\frac{C_l^{s_i s_i}}{C_l^{s_i s_i} + (\sigma_i^2/N_i)} \right]^2 \ . \qquad (4.33)
$$

4.4   Numerical approach

In this Section, the implementation of the code used to re-create the results of [47] is reported. In particular, the open code CAMB sources (Sec. 4.4.1, [12]) has been

---

[3]It is called "systematic" an error whose average on different kinds of data is zero.

used to obtain the matter and lensing APS. They have been inserted in a `Python` code (Sec. 4.4.2) together with the other functions necessary to calculate eq. (4.17). The problems and the results met in this analysis have been reported (Sec. 4.4.3).

4.4.1 CAMB sources

CAMB sources [12] is an open `Fortran 90` code implemented to calculate number counts, lensing and dark age 21cm PS, plus thermal history, perturbed recombination and CMB cross correlations. It is based on CAMB (Code for Anisotropies in the Microwave Background) by A. Lewis and A. Challinor [13].

It allows to calculate the APS as it was defined by eq. (2.43) in Sec. 2.2.2. At low l the results are fully spherical and calculated by direct integration of the spherical Bessel functions (the complete derivation can be found in [15]). It uses by default a finite width Gaussian selection function in redshift. On the other hand, on small scales the results are obtained using the Limber approximation (see Sec. 2.2.2); the code tries to guess the appropriate scale at which to switch.

At low redshifts, non linear corrections to the matter evolution are considered thanks to the revised Halofit model (see [62] and [64]). It considers that all the matter in the Universe is bound into non collisional DM halos [64]; these collapse gravitationally in a hierarchical way. In this scenario, the smaller scales collapse earlier, breaking the stable clustering hypothesis[4], that in other models is usually assumed. It provides inside each halo a correlation due to the density profile (see [64] for details) and at the same time a correlation between different halos at the larger scales.

Input

CAMB sources input can be set using the file `params_counts.ini`. Many parameters have to be specified; between them, the ones used to define the redshift intervals over which the APS has to be calculated are:

- `redshift`, the central value of the redshift bin;

- `redshift_kind`, the type of APS (`counts` or `lensing`) that has to be calculated;

- `redshift_bias`, the bias (see Sec. 2.2.2);

- `redshift_sigma`, the Gaussian standard deviation;

- `redshift_dlog10Ndm`, the magnification bias (see Sec. 2.3.1).

`redshift` and `redshift_bias` are used to define the Gaussian selection function in the bin; inside it, the APS is obtained thanks to the average of the APS calculated for each point that the bin contains.

The values that have been chosen as inputs are reported in Tab. 4.1. 4.2, 4.3 and will be better explained in Sec. 4.4.2. The code dependence on the changes of these values has been studied and is reported in Sec. 4.4.3.

---

[4]The stable clustering hypothesis assures that the denser fluctuations create non linear collapsed objects that decouple from the Universe expansion: they can be considered as isolated systems where the virial equilibrium is mantained [62].

$z \in [0,1]$											
4 bins			5 bins			10 bins					
r	r_s	r_b	r	r_s	r_b	r	r_s	r_b	r	r_s	r_b
0.125	0.17	2.42	0.1	0.14	2.41	0.05	0.07	2.37	0.55	0.07	2.75
0.375	0.25	2.61	0.3	0.25	2.55	0.15	0.1	2.44	0.65	0.07	2.84
0.625	0.17	2.82	0.5	0.14	2.71	0.25	0.07	2.51	0.75	0.07	2.93
0.875	0.17	3.04	0.7	0.14	2.88	0.35	0.07	2.59	0.85	0.07	3.02
−	−	−	0.9	0.14	3.06	0.45	0.07	2.67	0.95	0.07	3.11

Table 4.1: The redshift interval $z \in [0,1]$ has been divided into 4, 5 and 10 bins (see Sec. 4.4.2). For each one of them, the APS has been calculated using CAMB sources. The input parameters `redshift` = r, `redshift_sigma` = r_s and `redshift_bias` = r_b are reported (see Sec. 4.4.1). In particular, r_s has been chosen equal to 2/3 of the bin amplitude (e.g. 4 bins: $1/4 \cdot 2/3 = 0.17$), except for the second bin of each realization. Here an error occurred in CAMB calculations, so the bin amplitude itself has been used. r_b has been calculated using eq. (2.56). `redshift_dlog10Ndm` is not reported because its value has always been set equal to 0.4, in order to nullify the magnification bias (see Sec. 2.3.1).

$z \in [1.4, 1.9]$											
4 bins			5 bins			10 bins					
r	r_s	r_b	r	r_s	r_b	r	r_s	r_b	r	r_s	r_b
1.462	0.08	3.62	1.45	0.07	3.60	1.425	0.05	3.58	1.675	0.05	3.84
1.587	0.08	3.75	1.55	0.07	3.71	1.475	0.05	3.63	1.725	0.05	3.89
1.712	0.08	3.88	1.65	0.07	3.81	1.525	0.05	3.68	1.775	0.05	3.94
1.832	0.08	4.00	1.75	0.07	3.92	1.575	0.05	3.73	1.825	0.05	4.00
−	−	−	1.85	0.07	4.02	1.625	0.05	3.78	1.875	0.06	4.05

Table 4.2: The redshift interval $z \in [1.4, 1.9]$ has been divided into 4, 5 and 10 bins (see Sec. 4.4.2). For each one of them, the APS has been calculated using CAMB sources. The input parameters `redshift` = r, `redshift_sigma` = r_s and `redshift_bias` = r_b are reported (see Sec. 4.4.1). In particular, r_s has been chosen equal to 2/3 of the bin amplitude, except for the 10 bins case: here the value $(1.9 − 1.4)/10 \cdot 2/3 = 0.03$ would be too small (CAMB returns `NAN`). The amplitude of the bin itself has therefore been chosen; the last bin, however, required a even bigger value. r_b has been calculated using eq. (2.56). `redshift_dlog10Ndm` is not reported because its value has always been set equal to 0.4, in order to nullify the magnification bias (see Sec. 2.3.1).

$z \in [2.6, 4.9]$											
4 bins			5 bins			10 bins					
r	r_s	r_b	r	r_s	r_b	r	r_s	r_b	r	r_s	r_b
2.887	0.38	5.25	2.83	0.31	5.17	2.715	0.15	5.03	3.865	0.15	6.63
3.462	0.38	6.03	3.29	0.31	5.78	2.945	0.15	5.32	4.095	0.15	7.00
4.037	0.38	6.91	3.75	0.31	6.45	3.175	0.15	5.63	4.325	0.15	7.40
4.612	0.38	7.93	4.21	0.31	7.20	3.405	0.15	5.94	4.555	0.15	7.82
−	−	−	4.67	0.31	8.04	3.635	0.15	6.28	4.785	0.15	8.27

Table 4.3: The redshift interval $z \in [2.6, 4.9]$ has been divided into 4, 5 and 10 bins (see Sec. 4.4.2). For each one of them, the APS has been calculated using CAMB sources. The input parameters `redshift` = r, `redshift_sigma` = r_s and `redshift_bias` = r_b are reported (see Sec. 4.4.1). In particular, r_s has been chosen equal to 2/3 of the bin amplitude. r_b hab been calculated using eq. (2.56). `redshift_dlog10Ndm` is not reported because its value has always been set equal to 0.4, in order to nullify the magnification bias (see Sec. 2.3.1).

Output

The `_scalCovCls.dat` file that CAMB returns when running `params_counts.ini` contains the auto and cross PS; its columns are of the form

$$l \quad C_{11} \quad C_{12} \quad ... \quad C_{1n} \quad C_{21} \quad C_{22} \quad ... \quad C_{nn} \; ,$$

where the PS are unlensed and dimensionless and they are equal to

$$C_{ij} = \frac{l(l+1)}{2\pi} C_l^{ij} \; , \qquad (4.34)$$

The fields i, j are ordered as T, E, Φ, win_1, win_2... , where T, E depends on the CMB PS, Φ is the CMB lensing potential and win_1, win_2... are the `counts` or `lensing` PS in the redshift bin (see [12] for more details). In this work, the quantities required are the auto and cross C_l^{ij} calculated for the matter δ and for the lensing k.

4.4.2 `Python` code

In [47], the method described in Sec. 4.2 is presented and some results are shown. However, the computational realization is completly missing. The main task of this work has therefore been the full numerical implementation of the statistical analysis [47] propose. This method, in fact, is used in [47] only to forecast the sensitivity with which ET will estimate primordial non gaussianity; nevertheless it could be used to obtain much more information, both on Cosmology and Astrophysics. Some of its applications are reported in Sec. 4.5.

In this perspective, the results reported in this work are the first, necessary step to develop all the other applications. To achieve them, a `Python` code has been written in order to implement eq. (4.17). It uses the `Python` libraries `os`, `math`, `numpy`, `matplotlib.pyplot`, `scipy.signal`, `scipy.integrate`. In particular, when an integration is required, it is performed using `scipy.integrate.trapz` which operates over sampled array. Initially, the following global variables are defined.

- the speed of light in km s^{-1}: `light` $= 3. \cdot 10^5$;

- the Ω_m value (see Chapter 2): `om` $= 0.2511$;

- the Ω_Λ value (see Chapter 2): `ol` $= 0.729$;

- the Hubble parameter as of today in km s^{-1} Mpc^{-1} (see Chapter 2): `H0` $= 70.3$;

- the Hubble parameter as of today in Mpc^{-1}: `H0_scaled` $=$ `H0`/`light`;

- the redshift value used as upper extremity when an integration up to infinity would be required: `Z` $= 10$. This is done to reduce the computational cost; the value is chosen because the growth function assures that there are no other sources farther than that (see Figure 2.2);

- the number of points in which the arrays are sampled: `npt` $= 101$. Other values (11 and 501) have also been used.

Before running the code, it is necessary to obtain the APS using CAMB sources: Figure 4.1 requires them in the redshift intervals $[0, 1]$, $[1.4, 1.9]$ and $[2.6, 4.9]$. Since, as already mentioned in Sec. 4.4.1, CAMB calculates the average APS inside the Gaussian defined by the input parameters, the redshift intervals have been divided

into 4, 5 and 10 bins. Over each of them, a Gaussian function has been built (see Tab. 4.1, 4.2 and 4.3); the curves partially overlap and permit to calculate different APS: these will be combined thanks to the `Python` code.

The code is organized as follows.

1. For each redshift interval ($[0, 1], [1.4, 1.9], [2.6, 4.9]$), the CAMB output files for a given bin set (4, 5 or 10) are read and the columns $C_{\delta\delta}$, $C_{\delta k}$, $C_{k\delta}$, C_{kk} (see eq. (4.34)) with the auto and cross APS are imported. Their values are then rescaled using the factor $2\pi/l(l+1)$ and for each bin four arrays containing $C_l^{\delta\delta}$, $C_l^{\delta k}$, $C_l^{k\delta}$, C_l^{kk} (see eq. (4.17)) are created.

2. The two redshift arrays are created dividing the redshift intervals into evenly spaced points (e.g. the interval $[0, 1]$ can be divided into 101 points). The array has to describe the redshift intervals that the APS has to study; in the case of auto APS, the two redshift arrays are therefore equal.

3. Some integrations are perfomed from 0 to infinity. To reduce the computational cost, they are calculated up to a fixed finite value: it is therefore created a redshift array formed by evenly spaced points between 0 and `Z`, whose value choice has been explained previously.

4. The redshift arrays are converted into luminosity distance arrays using eq. (2.15). In the case of auto APS, the two luminosity distance arrays are equal.

5. The $\gamma(D_L)$ factor defined in eq. (4.12) has to be implemented as an array containing for each value of D_L the associated γ. To do so, the δ_D function has to be discretized: it is defined as $\int_{-\infty}^{+\infty} \delta_D(x - a)f(x)\,dx = f(a)$, and its discretization into $i = 1, ..., N$ points gives $\sum_i \delta_{ij}(x_i - a)f(x_i)\Delta x_i = f(a)$. Assuming a uniform binning in the interval $[D_L^{min}, D_L^{max}]$, it follows that $\Delta x_i = \Delta$ is the amplitude $(D_L^{max} - D_L^{min})/N$ and δ_{ij} is the Kronecker delta[5]. Consequently, the discretization brings to the substitution of $\delta_D(x_i - a)$ with δ_{ij}/Δ. In the case of auto APS, the $\gamma(D_1)$ and $\gamma(D_2)$ arrays are equal. It is important to note that eq. (4.12) defines $\gamma(D_L) = 1 + D_L[\delta_D(D_L - D_{Li}^{min}) - \delta_D(D_L - D_{Li}^{max})]$: therefore, when the redshift intervals are binned, $D_{Li}^{min,max}$ are the luminosity distances corresponding to the bounds of each bin.

6. To obtain eq. (4.17) requires the factor $F = \{C_l^{\delta_1\delta_2} + \gamma(D_{L1})\gamma(D_{L2})C_l^{k_1k_2} + \gamma(D_{L1})C_l^{\delta_2k_1} + \gamma(D_{L2})C_l^{\delta_1k_2}\}$. It is created as a matrix containing for each bin of the redshift intervals the appropriate value of the arrays $C_l^{\delta_1\delta_2}$, $C_l^{k_1k_2}$, $C_l^{\delta_2k_1}$ and $C_l^{\delta_1k_2}$. This means that the factor is a block diagonal matrix, where the blocks are defined using the bin bounds. E.g. in the case of $[0, 1]$ divided into 4 bins the matrix is

$$
\begin{pmatrix}
C_l^{\delta_1\delta_1} + ... & 0 & 0 & 0 \\
0 & C_l^{\delta_2\delta_2} + ... & 0 & 0 \\
0 & 0 & C_l^{\delta_3\delta_3} + ... & 0 \\
0 & 0 & 0 & C_l^{\delta_4\delta_4} + ...
\end{pmatrix}, \tag{4.35}
$$

---

[5]The Kronecker delta is defined as

$$
\delta_{ij} = \begin{cases} 1 & \text{if} \quad i \neq j \\ 0 & \text{if} \quad i = j. \end{cases}
$$

where the first block is defined in $0 \lesssim z_1 \lesssim 0.25$ and $0 \lesssim z_2 \lesssim 0.25$, the second in $0.25 < z_1 \lesssim 0.5$ and $0.25 < z_2 \lesssim 0.5$, the third in $0.5 < z_1 \lesssim 0.75$ and $0.5 < z_2 \lesssim 0.75$ and the last one in $0.75 < z_1 \lesssim 1$ and $0.75 < z_2 \lesssim 1$. This is an approximation: the matrix elements set to 0 should also be filled. E.g. the block with $0 \lesssim z_1 \lesssim 0.25$ and $0.25 < z_2 \lesssim 0.5$ should contain $C_l^{\delta_1 \delta_2} + ...$. This is not done in this work, but it will be implemented in future ones (see Sec. 4.5).

7. The factors $\bar{n}(D_{L1,2})$ are calculated as $n(D_L) = D_L p(D_L) = D_L p(D_L(z))$, where the normalized source distribution $p(z)$ is derived from [19] and it is

$$p(z) = \frac{1}{N}\frac{dN}{dz} = \frac{1}{N}\left(4\pi t \, [a_0 r_1(z)]^2 \, \dot{n}(z)\frac{d\tau_1}{dz}\right) . \tag{4.36}$$

The expression in parenthesis in eq. (4.36) has been described in eq. (2.55). The only difference between the two is that the expression in the first one was integrated in redshift while here it is integrated in time. In the case of auto APS, $\bar{n}(D_{L1})$ and $\bar{n}(D_{L2})$ are equal.

8. The factors $\bar{d}_i$ and $\bar{d}_j$ defined in Sec. 4.2.2 are calculated integrating $\bar{n}(D_{L1})$ and $\bar{n}(D_{L2})$ in function of D_L. In the case of auto APS, they are equal.

9. In eq. (4.17) all the functions depend on the luminosity distance D_L and the integration is performed in dD_L. However, in this work both the source distribution $p(z)$ and F are functions of the redshift z. The latter, in fact, associates different combinations of the CAMB APS to different values of the redshift. In this work, it has been decided to perform the integration in dz: the conversion can therefore be made as

$$\int_{D_L^{min}(z)}^{D_L^{max}(z)} f(D_L)\,dD_L = \int_{z^{min}}^{z^{max}} f(z)\frac{dD_L}{dz}\,dz , \tag{4.37}$$

Using eq. (2.15) the conversion factor can be calculated as

$$\frac{dD_L}{dz} = \int_0^z \frac{dz'}{H(z')} + \frac{1+z}{H(z)} . \tag{4.38}$$

Eq. 4.38 is used to calculate dD_{L1}/dz and dD_{L2}/dz, which are implemented as arrays; in the case of auto APS, they are equal.

10. $C_l^{s_i s_j}$ is obtained integrating $n(D_L)(dD_{L2}/dz)\cdot F/\bar{d}_j$ in z_2 and then multiplying the result for $n(D_L)(dD_{L1}/dz)/\bar{d}_i$ and integrating in z_1.

11. The lensing APS $C_l^{k_1 k_2}$ is multiplied for $\gamma(D_{L2})n(D_L)(dD_{L2}/dz)/\bar{d}_j$, integrated in z_2 and then the result is multiplied for $\gamma(D_{L1})n(D_L)(dD_{L1}/dz)/\bar{d}_i$ and integrated in z_1.

12. The curves obtained for the redshift intervals $[0, 1]$, $[1.4, 1.9]$ and $[2.6, 4.9]$ plotting $C_l^{s_i s_j}$ and $C_l^{k_1 k_2}$ against l are reported in Figure 4.2. This has to be compared to Figure 4.1; in Sec. 4.4.3 the discussion about this is reported.
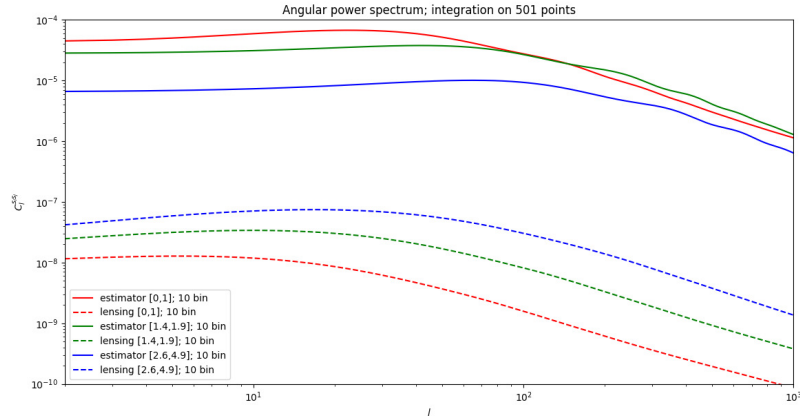
Figure 4.2: Results obtained using the `Python` code described in Sec. 4.4.2. The solid lines represent the auto APS $C_l^{s_i s_i}$ in the redshift intervals $[0, 1]$ (red), $[1.4, 1.9]$ (green) and $[2.6, 4.9]$ (blue). The dashed lines are the lensing APS $C_l^{k_1 k_1}$ for the same intervals. The discussion of these results can be found in Sec. 4.4.3.

Required functions

To realize the code described in Sec. 4.4.2 many functions have been defined. To monitor that their implementation is correct, some of them have been plotted and they are here reported.

The Cosmology is described by the $H(z)$ evolution: its trend, derived implementing eq. (2.9) in the `Python` code, is reported in Figure 4.3. It can be noticed that the two functions have the same trend in the redshift interval in which they are both defined.
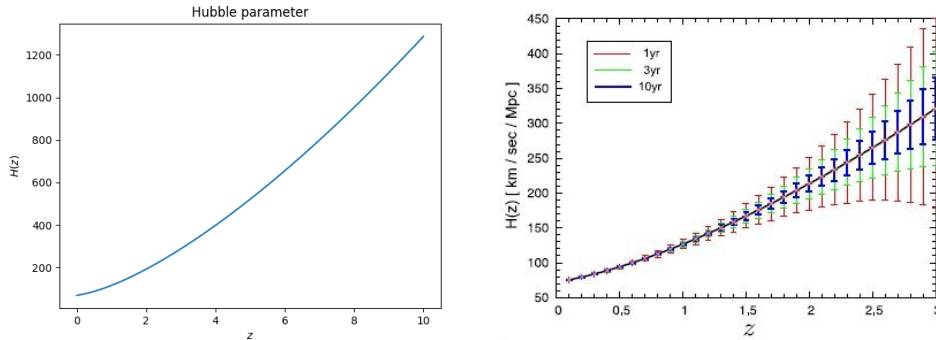

Figure 4.3: The images represent the $H(z)$ evolution: the left one is obtained through the `Python` code, while the right one is taken from [52]. It is important to note that the first one is plotted in the redshift interval $[0, 10]$, while the second in $[0, 3]$.

The growth function has been defined in eq. (2.29) and its implementation is reported in Figure 4.4. It can be compared to the one reported in Figure 2.2 taken from [22]. It can be noticed that the two functions have the same trend. Figure 4.4 shows also the bias as obtained from the implementation of eq. (2.42).
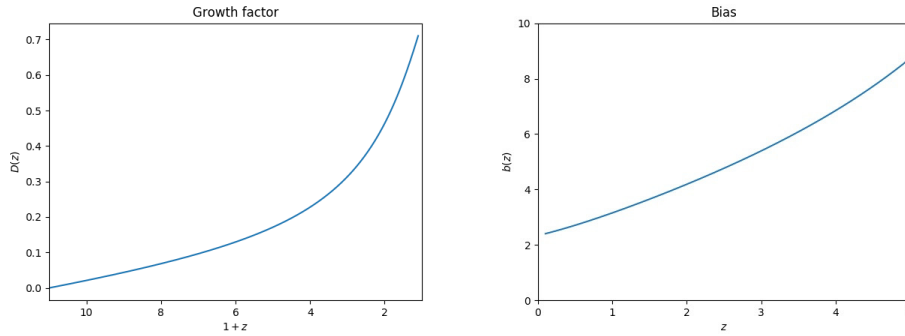
Figure 4.4: On the left hand side: growth function obtained thanks to the implementation of eq. (2.29). On the right hand side: bias obtained thanks to the implementation of eq. (2.42); it is represented only in the redshift interval $[0, 5]$ because, according to the merging rate reported in eq. (2.54), outside it there are not NS-NS systems. All the eq. are described in Chapter 2.

Finally, Figure 4.5 represents the normalized source distribution, as described in eq. (4.36), derived from [19]. From its trend, it is clear that it can be considered as a redshift selection function (see Sec. 2.3.1).
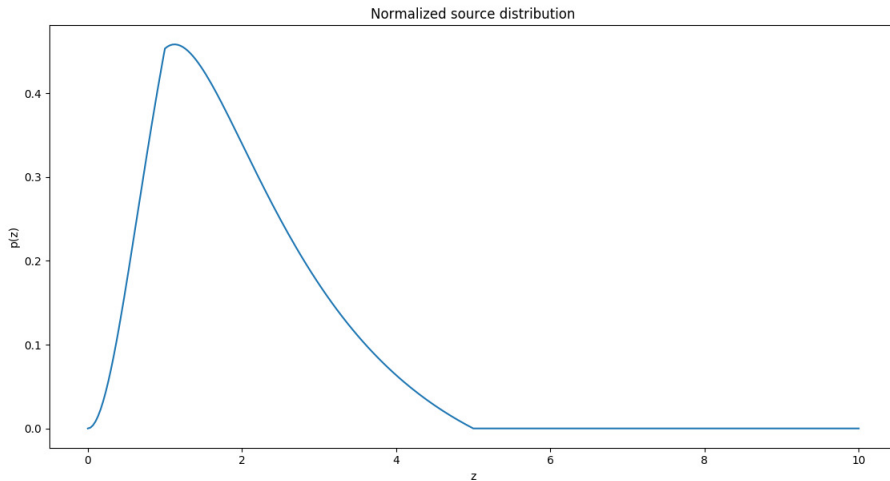

Figure 4.5: Normalized source distribution obtained implementing eq. (4.36) in the `Python` code.

4.4.3   Result discussion

As Sec. 4.4.2 described, the auto APS have been calculated in the three redshift intervals $[0, 1]$, $[1.4, 1.9]$ and $[2.6, 4.9]$. Each of them has been divided into 4, 5 and 10 bins in which the average APS has been derived thanks to CAMB sources. They have then been integrated using arrays sampled with 11, 101 and 501 points.

The curves in each of these cases have been reported in Figure 4.6, 4.7 and 4.8. It

can be noticed that the integration with 11 points more than once creates some problems. When the number of points used to sample the arrays increases, $C_l^{k_1 k_2}$ varies, while $C_l^{s_i s_j}$ seems to converge. On the other hand, $C_l^{k_1 k_2}$ seems not to having dependence on the number of bins used; $C_l^{s_i s_j}$ contrariwise changes its shape depending on its value.

Thanks to these considerations, it has been chosen to plot Figure 4.2 using 10 bins and 501 points for the integration.
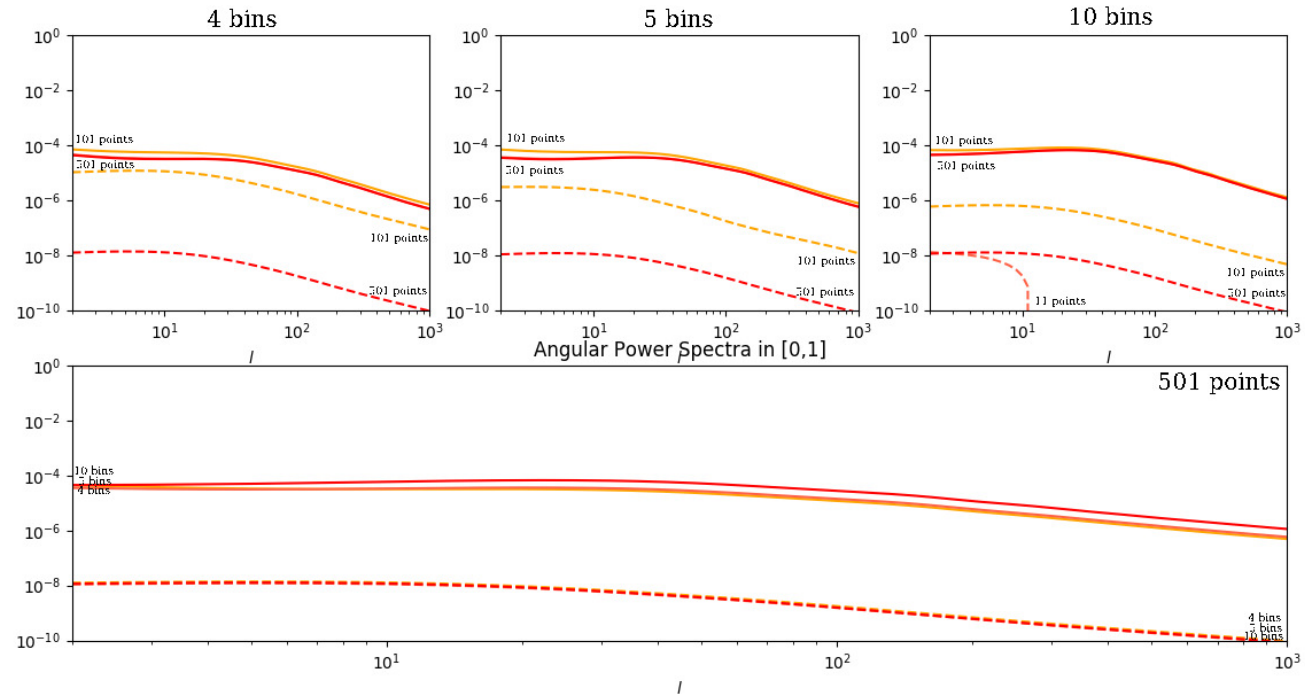
Figure 4.6: In the redshift interval [0, 1], the curves produced by the `Python` code described in Sec. 4.4.2 are represented. In the upper images, the changes due to the points used to sample the arrays are studied. Particularly, the first one is obtained with 4 bins, the second one with 5 bins and the last one with 10 bins. The lower image instead shows how, if the sampling is fixed, the number of the bins affects the curves. Considerations about these images are reported in Sec. 4.4.3.
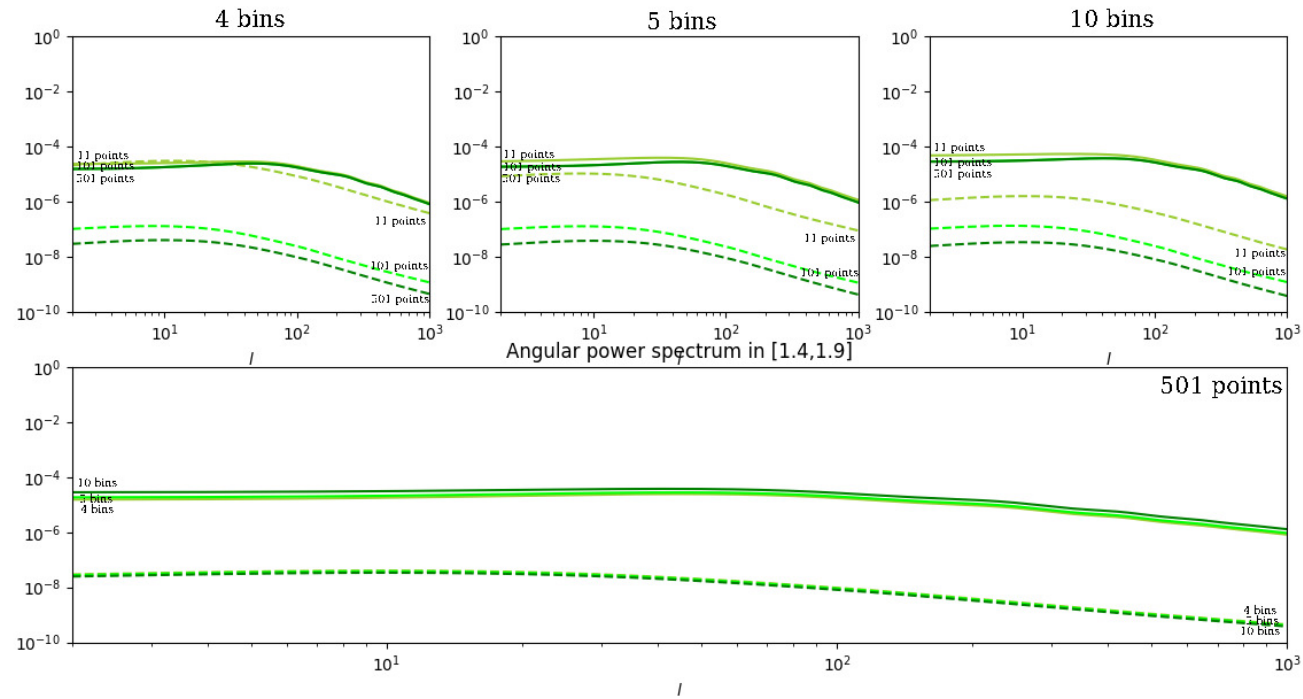
Figure 4.7: In the redshift interval $[1.4, 1.9]$, the curves produced by the `Python` code described in Sec. 4.4.2 are represented. In the upper images, the changes due to the points used to sample the arrays are studied. Particularly, the first one is obtained with 4 bins, the second one with 5 bins and the last one with 10 bins. The lower image instead shows how, if the sampling is fixed, the number of the bins affects the curves. Considerations about these images are reported in Sec. 4.4.3.
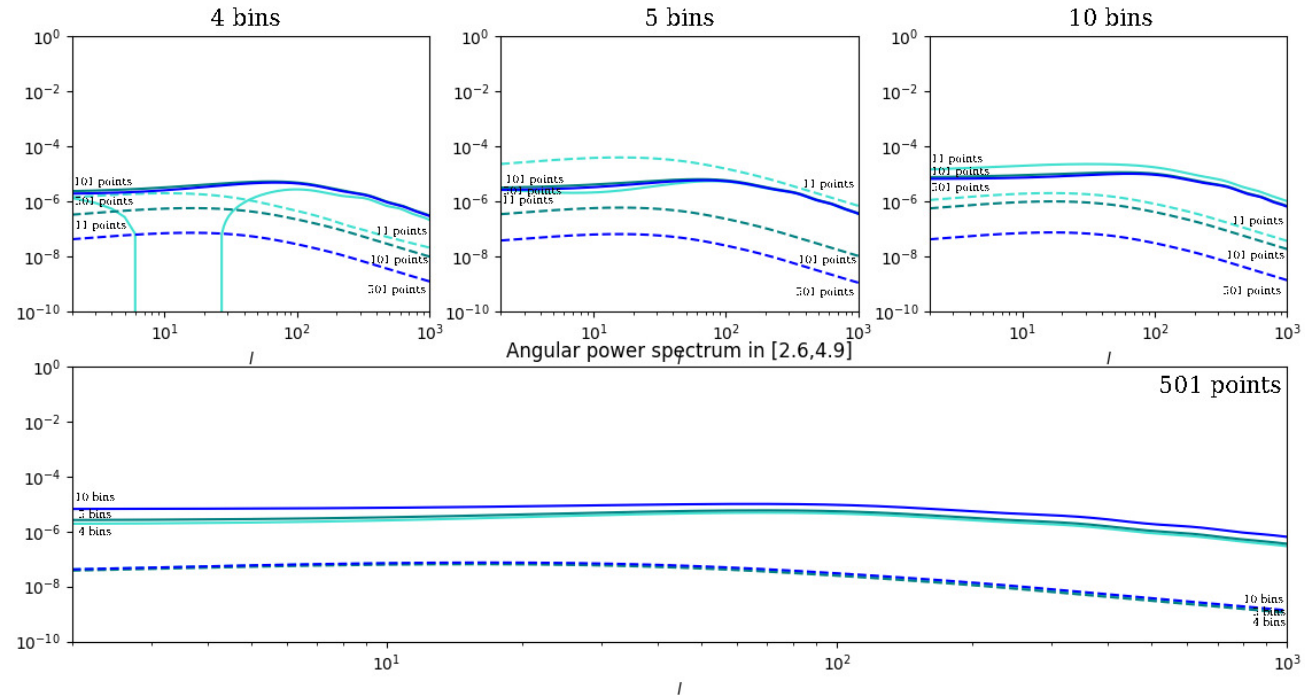
Figure 4.8: In the redshift interval [2.6, 4.9], the curves produced by the `Python` code described in Sec. 4.4.2 are represented. In the upper images, the changes due to the points used to sample the arrays are studied. Particularly, the first one is obtained with 4 bins, the second one with 5 bins and the last one with 10 bins. The lower image instead shows how, if the sampling is fixed, the number of the bins affects the curves. Considerations about these images are reported in Sec. 4.4.3.

4.5   What's next?

The analysis performed in this Chapter represents the first step to implement the study of GWs as standard sirens without redshift information. It contains some approximations, that will be improved in future works.

Particularly, the next steps that need to be realized are the following.

- Changing the gr expression in eq. (4.35) considering also the cross terms between different bins. In this way, gr will no more be diagonal and $C_l^{s_i s_j}$ will be calculated better.

- Increasing the correspondence between the curves in Figure 4.1 and 4.2 by refining the binning. In particular, the condition of equal number of sources in each redshift interval (see Sec. 4.2.3) has to be tested and implemented.

- Refining the assumed Astrophysical models for the merger rate, the bias and the GW wavefront, for example inserting a chirp mass distribution, some information on the spin of the merging objects or on the inclination of the systems with respect to the detector, in order to improve the APS calculation. On the other hand, trying to study other source distributions, such as NS-BH and BH-BH; this kind of study could be very useful in the latter case, when no EM counterpart is emitted. Degeneracies between the different parameters should also be studied.

- Calculating the cross APS between different redshift intervals. In this case, the lensing contribution will probably increase: in fact, when observing sources located at different luminosity distances the presence of the LSS along the LoS determines an increase in the lensing effects.

- Calculating numerically the Fisher matrix and the SNR (see Sec. 4.3), in order to forecast the sensibility of future experiments to the estimation of some parameters. In particular, the errors on the APS should be derived and inserted in Figure 4.2. Moreover the cumulative SNR should be plot, in order to be compared to the lower image in Figure 4.1.

- Assuming the Astrophysical models for the source distribution, the bias and the GW signal, Cosmology can be constraint from the Fisher matrix study. For example, the authors of [47] explain how the fluctuations in the luminosity distance - redshift relation between data and forecasting quantities will give information on the matter distribution in the Universe and the primordial non gaussianity in the CMB perturbation distribution.

- Assuming the Cosmological models in order to use the Fisher analysis to get information on the Astrophysical parameters. In particular, the NS-NS systems merger rate, their distribution and the bias they have with respect to DM could be better understood using the fluctuations in the luminosity distance - redshift relation between data and forecasting quantities.

- Increasing the forecasting precision thanks to simulations of the source distribution obtained with Monte Carlo methods (see Sec. 3.2.3)) and combining them to other datasets (CMB, GWs measurements...).

In conclusion, the method presented in this Chapter has to be refined, but it could be really useful to constraint both Astrophysical and Cosmological models.

Conclusions

Chapter 1 explained how Gravitational Waves generate and propagate; it described different kinds of GW sources and it presented the existing and future Gravitational Wave detectors. The Post Newtonian model used to describe their wavefront was analyzed and the use of Gravitational Waves as standard sirens was introduced. On the other hand, Chapter 2 presented the Cosmological theories that today describe what the Universe is like and how it evolves. It introduced both the background and the fluctuation structures, focusing on the evolution of the latter and the lensing that their distribution induces. Chapter 3 instead introduced some statistical techniques useful to the data analysis and the forecasting of future experiments. Particular attention was given to the Fisher matrix of the Angular Power Spectrum.

Combining all these notions, Chapter 4 analyzed a special case. It defined an anisotropy estimator by which the clustering and lensing properties of the NS-NS binary merger distribution can be studied. It derived its Angular Power Spectrum and the Angular Power Spectrum of the weak lensing effect over such distribution. The Fisher matrix necessary to study the estimator and the Power Spectrum errors was calculated. Finally, the Angular Power Spectra were computationally implemented. The results can be compared with those in [47]: some curves still do not converge perfectly. This is probably due to the approximation used to define the term in eq. (4.35), where the cross Power Spectra between different bins in each redshift interval were not considered. Future developments were finally presented. In particular, the first step is to introduce these terms and then to implement the Fisher matrix calculation. At this point, the method will be ready to be used for scientific purposes.

In conclusion, this work created the means that future works will use to infer both Cosmological and Astrophysical properties, providing new instruments to interface these two fields. In the meantime, Gravitational Wave Astronomy will develop and in the next years more and more data will be taken: this will surely lead to a better understanding of the structure and the history of the Universe, both on small and large scales.

Bibliography

[1] Abbott B.P. et al. (LIGO Scientific Collaboration and Virgo Collaboration) (2016),
Observation of Gravitational Waves from a Binary Black Hole Merger
`Phys. Rev. Lett. 116, 061102`

[2] Abbott B.P. et al. (LIGO Scientific Collaboration and Virgo Collaboration) (2016),
Binary Black Hole Mergers in the First Advanced LIGO Observing Run
`PHYS. REV. X 6, 041015`

[3] Abbott B.P. et al. (LIGO Scientific Collaboration and Virgo Collaboration) (2016),
GW151226: Observation of Gravitational Waves from a 22-Solar-Mass Binary Black Hole Coalescence
`Phys. Rev. Lett. 116, 241103`

[4] Abbott B.P. et al. (LIGO Scientific Collaboration and Virgo Collaboration) (2017),
GW170104: Observation of a 50-Solar-Mass Binary Black Hole Coalescence at Redshift 0.2
`Phys. Rev. Lett. 118, 221101`

[5] Abbott B.P. et al. (LIGO Scientific Collaboration and Virgo Collaboration) (2017),
GW170814: A Three-Detector Observation of Gravitational Waves from a Binary Black Hole Coalescence
`Phys. Rev. Lett. 119, 141101`

[6] Abbott B.P. et al. (LIGO Scientific Collaboration and Virgo Collaboration) (2017),
GW170817: Observation of Gravitational Waves from a Binary Neutron Star Inspiral
`Phys. Rev. Lett. 119, 161101`

[7] Asorey J. et al. (2016),
Galaxy clustering with photometric surveys using PDF redshift information
`Mon. Not. R. Astron. Soc. 000, 1-19`

[8] Barber A.J., Taylor A.N. (2003),
Shear and magnification angular power spectra and higher-order moments from weak gravitational lensing
`arXiv:astro-ph/0212378v2`

[9] Bartolo N. et al. (2018),
Probing non-Gaussian Stochastic Gravitational Wave Backgrounds with LISA
`arXiv:1806.02819`

[10] Bartolo N. et al. (2016),
Science with the space-based interferometer LISA. IV: Probing inflation with gravitational waves
`arXiv:1610.06481`

[11] Bartolo N. (2018),
Note di Cosmologia dell'Universo Primordiale per il Corso di Laurea Magistrale in Fisica
`Università degli studi di Padova`

[12] CAMB sources,
`https://camb.info/sources/`

[13] CAMB,
`https://camb.info/`

[14] Caprini C., Figueroa D.G. (2018),
Cosmological backgrounds of Gravitational Waves
`arXiv:1801.04268`

[15] Challinoir A., Lewis A. (2011)
The linear power spectrum of observed source number counts `arXiv:1105.5292v2`

[16] Coe D. (2009),
Fisher matrices and confidence ellipses: a quick start guide and software
`arXiv:0906.4123v1`

[17] Coles P., Lucchin F. (2002),
Cosmology - The origin and evolution of cosmic structure
`John Wiley & Sons, Ltd`

[18] Cutler C., Flanagan E.E. (1994),
Gravitational waves from merging compact binaries: How accurately can one extract the binary's parameters from the inspiral waveform?
`arXiv:gr-qc/9402014v1`

[19] Cutler C., Harms J. (2006),
BBO and the Neutron-Star-Binary subtraction problem
`arXiv:gr-qc/0511092v4`

[20] Cutler C., Holz (2009),
Ultra-high precision Cosmology from gravitational waves
`arXiv:0906.3752v1`

[21] Di Dio E. et al. (2016),
Curvature constraints from Large Scale Structure
`arXiv:1603.09073v2`

[22] Dodelson S. (2003),
Modern Cosmology
`Academic Press`

[23] ET Science Team (2011),
Einstein gravitational wave Telescope conceptual design study
`http://www.et-gw.eu ET-0106C-10`

[24] Ezquiaga J.M., Zumalacarregui (2017),
Dark Energy after GW170817
`arXiv:1710.05901v1`

[25] Franceschini A. (2017),
Lecture notes for the Theoretical Astrophysics and Cosmology course held for the master Astronomy degree course
`Università degli studi di Padova`

[26] Guzzetti M.C., Bartolo N., Liguori M., Matarrese S. (2016),
Gravitational Waves from Inflation
`arXiv:1605.01615`

[27] Guzzo M. (2017),
Lecture notes for the Mathematical Physics course held for the master Astronomy degree course
`Università degli studi di Padova`

[28] Hartle J.B. (2003),
Gravity: an introduction to Einstein's General Relativity
`Addison Wesley`

[29] Heavens A. (2010),
Statistical techniques in Cosmology
`arXiv:0906.0664v3`

79

[30] Hu W., Scranton R. (2004),
Measuring Dark Energy Clustering with CMB-Galaxy Correlations
`arXiv:astro-ph/040856v2`

[31] Huterer D. et al. (2000),
The Angular Power Spectrum of EDSGC galaxies
`Submitted to ApJ`

[32] KAGRA Observatory (2018),
`https://gwcenter.icrr.u-tokyo.ac.jp/en/`

[33] Kilbinger M. (2015),
Cosmology with cosmic shear observations: a review
`arXiv:1411.0115v2`

[34] Kirshner R.P. (1999),
Supernovae, an accelerating universe and the Cosmological constant
`Proc. Natl. Acad. Sci. USA Vol. 96`

[35] Komatsu E. et al. (2010),
Seven-year Wilkinson Microwave Anisotropy Probe (WMAP) observations: Cosmological interpretation
`arXiv:1001.4538v3`

[36] Lazzaro C. (2018),
Note sulle onde gravitazionali per il progetto Heraeus
`Università degli studi di Padova`

[37] Liddle A.R., Lyth D.H. (2009),
The Primordial Density Perturbation
`Cambridge University Press`

[38] LIGO Caltech (2018),
`https://www.ligo.caltech.edu/`

[39] LIGO India (2018),
`http://www.gw-indigo.org`

[40] LISA Consortium (2018),
`https://www.elisascience.org`

[41] Liu H. et al. (2018),
A blind search for a common signal in gravitational wave detectors
`arXiv:1802.00340v1`

[42] Longair M.S. (2008),
Galaxy formation - Second edition
`Springer`

[43] LoVerde M. et al. (2007),
Magnification–Temperature correlation: the Dark Side of ISW measurements
`arXiv:astro-ph/0611539v3`

[44] Maggiore M. (2008),
Gravitational Waves - Volume 1: theory and experiments
`Oxford University Press`

[45] Mandel I. et al. (2015),
Distinguishing types of compact-object binaries using the gravitational-wave signatures of their mergers
`arXiv:1503.03172v2`

[46] Marigo P. (2015),
Lecture notes for the Theoretical Astrophysics course held for the bachelor Astronomy degree course
`Università degli studi di Padova`

80

[47] Namikawa T., Nishizawa A., Taruya A. (2016),
Anisotropies of Gravitational-Wave Standard Sirens as a new Cosmological probe without redshift information
arXiv:1511.04638v2

[48] Namikawa T. (2011),
Magnification effect on the detection of non-Gaussianity from photometric surveys
arXiv:1103.1118v1

[49] NASA (2018),
https://www.nasa.gov/

[50] NASA (2018),
https://images.nasa.gov/

[51] Nishizawa A. et al. (2012),
Cosmology with space-based gravitational-wave detectors - dark energy and primordial gravitational waves -
arXiv:1110.2865v2

[52] Nishizawa A. et al. (2011),
Tracing the redshift evolution of the Hubble parameter with gravitational wave standard sirens
arXiv:1011.5000v2

[53] Nissanke S. et al. (2013),
Determining the Hubble constant from Gravitational Wave observations of merging compact binaries
arXiv:1307.2638v1

[54] Nobili L. (2000),
Astrofisica Relativistica
CLEUP Padova

[55] Owen B.J. (1995),
Search templates for Gravitational Wves from inspiraling binaries: Choice of template spacing
Submitted to Physical Review D

[56] Planck collaboration (2018),
Planck 2018 results. VI. Cosmological parameters
arXiv:1807.06209v1

[57] Postnov K.A., Yungelson L.R. (2014),
The evolution of compact binary star systems
Living reviews in Relativity 17:3.
https://doi.org/10.12942/lrr-2014-3

[58] Sadri H. (1999),
Mathematical Physics - A modern introduction to its foundations
Springer

[59] Salaris M. et al. (2005),
Evolution of Stars and Stellar Populations
John Wiley & Sons, Ltd.

[60] Schutz B. F. (2011),
Gravitational Waves from binary systems: probes of the Universe
Notes for Lectures at the Azores School on Observational Cosmology

[61] Sejnowski T. J. (1974),
Sources of gravity waves
Physics Today 27, 1, 40

[62] Smith R. E. et al. (2003),
Stable clustering, the halo model and nonlinear Cosmological Power Spectra
arXiv:astro-ph/0207664v2

[63] Stack Exchange (2017),
`https://tex.stackexchange.com`

[64] Takahashi R. et al. (2012),
Revising the Halofit model for the non linear matter Power Spectrum
`The Astrophysical Journal, 761:152`

[65] Tamanini N. et al. (2017),
Science with the space-based interferometer eLISA. III: Probing the expansion of the Universe using gravitational wave standard sirens
`arXiv:1601.07112v3`

[66] Tormen G. (2017),
Dispense di Relatività Generale per il Corso di Laurea Magistrale in Astronomia
`Università degli Studi di Padova`

[67] Turolla R. (2017),
Dispense di Astrofisica Relativistica per il Corso di Laurea Magistrale in Fisica
`Università degli Studi di Padova`

[68] Verde L. (2009),
Statistical methods in Cosmology
`arXiv:0911.3105v1`

[69] Virgo (2018),
`http://www.virgo-gw.eu/`

[70] Wittman D.,
Fisher matrices for beginners